University of Alberta

Simulations of Liquid Spreading and Particle Aggregation in Gas-Fluidized Beds

by

Monika Wasylkiewicz

A thesis submitted to the Faculty of Graduate Studies and Research
in partial fulfillment of the requirements for the degree of

Masters of Science

in

Chemical Engineering

Department of Chemical and Materials Engineering

© Monika Wasylkiewicz
Spring 2014
Edmonton, Alberta

Permission is hereby granted to the University of Alberta Libraries to reproduce single copies of this thesis and to lend or sell such copies for private, scholarly, or scientific research purposes only. Where the thesis is converted to, or otherwise made available in digital form, the University of Alberta will advise potential users of the thesis of these terms.

The author reserves all other publication and other rights in association with the copyright in the thesis and, except as herein before provided, neither the thesis nor any substantial portion thereof may be printed or otherwise reproduced in any material form whatsoever without the author's prior written permission.

Abstract

Introduction of a binding or reacting liquid into a gas-solid fluidized bed is common in industrial processes (e.g. fluid coking, catalytic cracking, granulation). Ability of the liquid to spread and the attractive effect on particles due to liquid bridge formation alter the fluidization behavior and process efficiency.

Direct numerical simulations are performed using the lattice-Boltzmann method, with liquid modeled as a scalar transferred during particle collisions. A liquid spreading model is introduced based on a liquid bridge growth rate, and liquid spreading is studied and analyzed in terms of diffusion coefficients. Then, a system of homogeneously wetted particles is simulated, with an attractive force applied between adjacent particles. Aggregate sizes and fluidization behavior are examined.

Liquid diffusion is slower horizontally than vertically. The relation between liquid spreading and solids volume fraction depends on liquid viscosity and surface tension. Systems simulated generally completely aggregate, with aggregation resulting in slip velocity increases.

Acknowledgements

I would like to express my gratitude to the many individuals who have made my time at the University of Alberta successful, enlightening, and enjoyable.

First and foremost, I would like to express gratitude to Dr. Jos Derksen, whose insight, supervision, and patience have been pivotal to my success. Throughout my degree, he has challenged me to broaden my knowledge, be thorough, and ensure high standards for my work. He has supported my work and provided excellent guidance. Additionally, I would like to acknowledge Dr. Petr Nikrityuk for stepping in during the concluding stages of my research, and for his role in providing feedback and support.

I am grateful to my friends and colleagues Alexandra Komrakova, Orest Shardt, and Radompon Sungkorn for the friendly, open environment they created within my research group. They were always willing to share their insight, and provided an excellent outlet for discussing challenges and problems regarding my research. Their friendship and support has been outstanding.

I would like to thank my industrial contacts, specifically Kevin Reid for his role in providing feedback and guidance, relevant data and knowledge. I acknowledge Syncrude Canada Ltd. for sponsoring my research.

Finally, I would like to acknowledge my parents, who have supported and encouraged me to pursue my academic aspirations.

Table of Contents

List of Tables

List of Figures

Nomenclature

A	Area [m^2]
$\mathbf{a}$	Angular position vector [-]
a	Separation distance between two particle surfaces [m]
Ar	Archimedes number [-]
b	Liquid bridge inner radius [m]
Bo	Bond number [-]
C	Liquid mass concentration [${}^{\mathrm{kg}}\!/\!{}_{\mathrm{m}^3}$]
$\mathbf{c}_i$	Velocity direction vector in direction i [lu]
Ca	Capillary number [-]
D	Particle diameter [m]
d	Spherical cap height covered by liquid bridge [m]
E	Residual error of fit [-]
$\mathbf{e}$	Unit vector [-]
e	Restitution coefficient [-]
$\mathbf{F}$	Body force vector [N]
F	Magnitude of force [N]
$\mathbf{f}$	External force [N/m^3]
f	Frequency [$1/\mathrm{s}$]
f_s	Friction coefficient [-]

g	Gravitational acceleration [$^{\mathrm{m}}/_{\mathrm{s}^2}$]
$g(coll)$	Relative collision velocity distribution function [-]
$g(N_{agg})$	Aggregate size distribution function [-]
$g(r)$	Radial distribution function [-]
H	Liquid bridge mean curvature [m^{-1}]
$H(r)$	Height of gap between particles as a function of liquid bridge radius [m]
h	Thickness of particle in analysis slice [m]
$\bar{\mathbf{I}}$	Identity matrix [-]
$\mathbf{I}$	Moment of inertia [$\mathrm{kg} \cdot \mathrm{m}^2$]
i, j, k	Counting variables [-]
$\mathbf{J}$	Impulse vector upon collision [$^{\mathrm{kg} \cdot \mathrm{m}}/_{\mathrm{s}}$]
L	Characteristic length scale [m]
$\mathbf{M}$	Torque [$\mathrm{N} \cdot \mathrm{m}$]
M	Number of surface control point for IBM [-]
m	Mass of particle [kg]
N	Number variable [-]
N_i	Dimensionless mass density in direction i [-]
Nx, Ny, Nz	Number of LBM nodes in x, y, z directions [-]
P	Pressure [Pa]
p	Number of fitting parameters [-]
Q	Number of data points used for curve fit [-]
r	Radial direction [m]
R_{ext}	External bridge radius of curvature [m]
Re	Reynolds number [-]
s	Arc length [m]

T_v	Viscous bridge growth number ($\frac{\mu_l U_\infty}{8\sigma}$) [-]
t	Time [s]
U	Characteristic velocity scale [m/s]
U_∞	Magnitude of single particle terminal settling velocity [m/s]
$\mathbf{u}(\mathbf{x},t)$	Fluid velocity vector at $(\mathbf{x},t)$ [m/s]
u	Magnitude of fluid velocity [m/s]
V	Volume [m^3]
$\mathbf{v}$	Solid velocity vector [m/s]
v	Magnitude of solid velocity [m/s]
w_i	Weight factor in direction i [-]
$\mathbf{x}$	Position vector [m]
x	Direction of diffusion (horizontal or vertical) [m]
x, y, z	Cartesian coordinates (z is direction of gravity) [m]

Greek Symbols

α, η	Angles [-]
β	Deviation from centre of curve fit peak [m]
Γ	Effective liquid diffusion coefficient [m^2/s]
γ	Half-filling angle [-]
Δt	Time step size [s]
Δx	Position step size [m]
Δp	Thickness of analysis slice [m]
δ	Liquid film thickness on particle [m]
θ	Contact angle [-]
μ	Dynamic viscosity [$\mathrm{Pa \cdot s}$]

ρ	Mass density [kg/m^3]
σ	Surface tension [Nm]
$\overline{\tau}$	Viscous stresss tensor [N/m^2]
τ_v	Viscous bridge growth time constant [s]
ϕ	Solids volume fraction [-]
Ω_i	Collision operator [-]
ω	Angular velocity vector [s^{-1}]

Subscripts

agg	Aggregate
b	Buoyancy
c	Capillary
co, nco	Contact, Non-contact
d	Drag
g	Gas
∞	Infinity (refers to single particle in infinite domain)
int	Internal fluid
lb	Liquid bridge
l	Liquid
m	Mixture
mf	Minimum fluidization
n	Normal direction
rel	Relative
s	Solid
sc	Spherical cap

sl	Slip
t	Tangential direction
tot	Total
v	Viscous

Abbreviations

ASD	Aggregate Size Distribution
CFD	Computational Fluid Dynamics
DEM	Discrete Element Method
FCHC	Face-Centred Hyper Cubic
IBM	Immersed Boundary Method
LBM	Lattice Boltzmann Method

Chapter 1

Introduction

1.1 Motivation

The global demand for petroleum products is ever increasing as countries industrialize and populations grow. This provides Canada with a unique opportunity due to its large reserves of unprocessed crude oil in the form of bitumen. Canada holds the third largest crude oil reserve, exceeded only by Saudi Arabia and Venezuela [1]. The social and political stability in Canada make it an attractive supplier. Currently, Canada is the 6th largest producer of crude oil, with over 3 million barrels of conventional oil and oil from oil sands produced daily [1].

The oil sands are comprised of a mixture of soil, minerals, water, and bitumen. Bitumen is the heaviest and thickest form of petroleum, requiring treatment to extract and process it into usable hydrocarbons. As compared with conventional crude oils, bitumen contains on average heavier hydrocarbon chains and can be several orders of magnitude more viscous. Additionally, it contains 50-60 % of vacuum residue (components that must first be converted into distillable fractions) [2]. Converting these heavy hydrocarbons into lighter distillable fractions is known as cracking, and is a major step in the upgrading of bitumen into useful products. The eventual goal is the production of synthetic crude oil, which has chemical and physical characteristics comparable to conventional light crude oils [3].

A technology used in Canada to crack the heavy hydrocarbons is coking, where vacuum residues are converted into carbon-rich solid coke, distillable liquids and light ends [4]. There are two main types of coking: delayed and fluid coking. Delayed coking heats the bitumen prior to introduction into a coke drum, where the liquid cracks due to low pressure and high temperature. Fluid coking heats the bitumen upon entry into the reactor, due to liquid coating heated coke particles. The higher temperatures in fluid coking (500-530 °C) compared to delayed coking (450-510 °C) and lower residence times for the vapor produced result in higher yields of light gases and distillate products in fluid coking [5].

The reactor portion of a fluid coker is a steam-fluidized bed containing solid coke particles. These particles are introduced into the top of the reactor section (see Figure 1.1), and are fluidized within the reactor through steam addition and hydrocarbon evolution. The reactor section of the fluid coker is of order 20 m high and 10 m wide, with an average particle diameter of 145 μm [6].

Liquid bitumen is injected through steam-assisted atomization nozzles, resulting in small drops that contact and coat coke particles. The high temperatures at the coke surface lead to thermal cracking of the hydrocarbon chains, resulting in the production of lighter gaseous components that are ejected upwards with the steam. The bottoms byproduct of this process is petroleum coke, which is made up mainly of residual carbon and causes the coke particles to grow in size. Between 15 and 25 % of the petroleum coke is recycled by passing through a secondary fluidized bed burner where it is reheated to process temperatures and reintroduced [7]. This is necessary since the use of thermal energy for the cleaving of hydrocarbon chains results in the cooling of the coke particles.

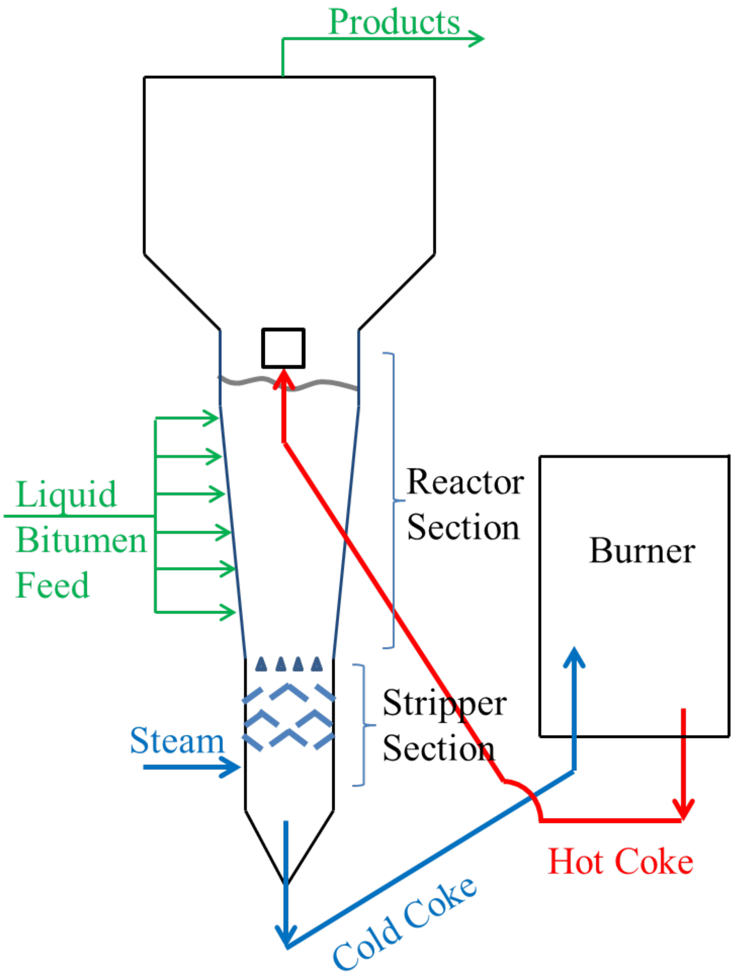

Figure 1.1: Simplified schematic of a fluid coker, reproduced based on Song et al. [6] and Darabi [3].

Typical product yields from the fluid coking process are provided in Table 1.1. Yields are dependent on the feed composition, specifically the metal, sulfur, and carbon content. Commercial units can process up to 100 KB/SD (kilobarrels per stream day) of feed [7].

Liquid bitumen is introduced through injection nozzles, with thick liquid films being deposited on particles near the injection sites. This liquid film thickness has

Table 1.1: Typical ranges of product yields [7].

Product	Yield (wt %)
Reactor Gas	11
Coker Naphtha	15-20
Light Gas Oil	12-14
Heavy Gas Oil	35-36
Net Coke	24

been shown to have a strong impact on the product yield [8]. Therefore, the efficiency of the process is highly dependent on the ability of liquid to spread from the injection nozzles throughout the reactor, resulting in thinner, more evenly distributed liquid films. Subsequent liquid-solid mixing results in the aggregation of coke particles. The liquid on the particle surfaces acts as a binder, forming liquid bridges between particles and resulting in the eventual formation of large granules made of several up to hundreds of particles [3]. The resulting aggregates settle more quickly and are more difficult to fluidize, potentially leading to partial or complete defluidization or plugging. Additionally, aggregation results in smaller overall surface areas for liquid contact, resulting in reduced heat transfer and therefore lower product yields [3].

The complex relationship between hydrodynamics, liquid injection, reaction kinetics, heat transfer, and mass transfer results in a process that, despite extensive research, is not fully understood. The various interconnecting effects are observed over a wide range of scales, from the reactor scale down to the molecular scale. At the reactor scale, the injection nozzles used, vessel size and dimensions, inlet flow rates, and type of fluidization are relevant. Focusing specifically on the fluidization, the gas-particle dynamics, motion of liquid through the bed, and resulting aggregation are the key physical phenomena affecting the fluid coking process. On the particle scale, there are effects due to shape and porosity of the particles, growth rate and profile of the liquid bridges between particles, and the wetting of the particles. The reaction process becomes relevant at smaller scales. For thinner films ($< 20\mu m$, or 0.14 of a particle diameter), the produced gases diffuse into the continuous gas phase [4]. However, at higher film thicknesses, diffusive mass transfer is limited and bubbling occurs in the films to transfer produced gas to the surface [4; 8], altering the rate at which liquid reacts (resulting in altered rates of changes in liquid properties) and the ratio of gases to coke produced. All of these scales are interdependent. For example, the change in viscosity due to the carbon reduction reaction will affect the formation of liquid bridges, altering the aggregation behavior and in turn the fluidization behavior. Conversely, effective mixing within the fluidization leads to efficient liquid spreading, resulting in thinner films, better solid-liquid heat transfer required for reaction, and therefore increased gas production.

Increasing global demand for petroleum products and more stringent environmental restrictions have encouraged research to improve the economy of operation of the fluid coking process. However, with various coupled processes occurring at different scales, industry-scale measurements and observations are limited. Simulations provide a good alternative, allowing for the separation and study of otherwise coupled effects. An understanding of the physics of these separate sub-processes and subsequent integration works to increase the understanding of the overall fluid coking process.

1.2 Thesis Objectives

Given the complexity of the interactions between different physical phenomena and the large range of scales at which these occur, direct simulation of the system is not possible. By identifying relevant phenomena occurring at a certain scale, the physics can be examined and integrated into other scales to improve the overall understanding of fluid coking. This thesis focuses on developing a fundamental understanding of liquid spreading within a fluid coker due to particle-particle collisions, and the resulting aggregation due to the formation of liquid bridges between wet particles.

The main objectives are as follows:

- Quantify liquid spreading due to particle-particle collisions as a function of the fluidization conditions (specifically solids volume fraction). The effect of the liquid spreading rules, used to calculate the per-collision liquid transfer, need to be determined. Here, the liquid presence does not affect the fluidization behavior (the liquid content is a passive scalar).
- Examine under what conditions aggregation occurs and the extent of that aggregation in the fluidized bed due to the presence of an adhesive force. This force is induced by the liquid (this parameter is now an active scalar) and mimics the formation of a liquid bridge between particles. The resulting changes in fluidization behavior can be quantified in terms of changes to gas-solid slip velocities.
- Develop a model that allows for variation in liquid properties, mimicking time dependency of liquid properties in fluid coking.

1.3 Thesis Outline

The thesis is organized as follows.

Chapter 2 provides an overview of the fundamental principles of fluidization. Previous work regarding simulations of fluidized beds is discussed, followed by an overview of the governing equations. Previous work regarding liquid spreading and the forces associated with liquid bridges are discussed, with emphasis on the methods implemented in this work. A novel liquid spreading model due to particle collisions is introduced, including a dependence of liquid viscosity, surface tension, and liquid film thickness. An overview of the numerical method is then described, including the use of the lattice-Boltzmann method (LBM), implementation of the immersed boundary method (IBM), initialization procedure, overview of physical properties, and model assumptions.

In Chapter 3, results are presented for liquid spreading rates in the form of horizontal and vertical effective diffusion coefficients due to particle-particle collisions and motion of particles. First, the liquid spreading methods are described in detail. The analysis method is then described. The analysis is begun by examining the effect of the simulation domain size on the resulting effective liquid diffusion rates. Following this, the effect of various liquid spreading models, solids volume fraction, and liquid properties on the effective liquid diffusion coefficient are examined.

Chapter 4 examines the effect of aggregation on fluidization. The problem is specified, including the aggregation model used, and liquid properties considered. Following this, examination of collision frequency, average number of liquid bridges per particle, and visualizations in order to determine the extent of aggregation are performed. Changes in fluidization behavior are then analyzed based on changes in volume-averaged particle Reynolds number, volume-averaged particle slip velocity, and aggregate size distribution (ASD).

Finally, Chapter 5 summarizes the work and discusses potential future extensions and improvements.

Chapter 2

Fundamentals

This chapter reviews and summarizes the various elements of the study, starting with an overview of the basics of fluidization and examples of industrial applications. Previous simulation work of wet gas-fluidized beds is discussed. The physical system is described in terms of mass and momentum conservation and the force relations between the gas and particle phase. Then, the mechanism for spreading of liquid due to particle-particle interactions and the resulting aggregating force is discussed. Numerical methodology is explained, with the gas system being described first, followed by the particle-particle and particle-gas interactions and liquid spreading. The boundary conditions and simulation initialization procedure are then discussed. The range of properties is discussed, along with the introduction of relevant non-dimensional parameters. Finally, required assumptions are listed.

2.1 Fluidization

Fluidization is a process in which an initially stationary bed of solid particles is suspended due to the upward motion of a fluid. A fluidized bed has various properties similar to a liquid, including the ability to be stirred. Additionally, density-based separation, with denser objects sinking and less dense objects floating, occurs within a fluidized bed [9]. The characteristics of the bed change as the fluid velocity is increased.

The bed is said to have reached incipient fluidization when the fluid velocity reaches minimum fluidization velocity u_{mf}. At this condition, the upward force of the fluid on the particles balances the downward gravitational force on the particles. Prior to this velocity, the bed is supported by the container. Beyond incipient fluidization, either homogeneous or heterogeneous fluidization occurs [10]. Particulate or homogeneous fluidization occurs when the bed expands, maintaining an approximately uniform distribution of particles. This results in minimal particle motion and mixing. Bubbling or heterogeneous fluidization occurs when fluid forms bubbles which rise through the bed. These bubbles result in considerable mixing of particles, due to solid particle entrainment in the bubble wake and large fluctuations in pressure [10].

For gas-fluidized beds, the fluidized bed behavior can be characterized based on the density difference between the particle and gas ($\rho_s - \rho_g$), and the mean particle diameter D. Geldart [11] developed a classification criteria for different fluidized systems, dividing them based on expected fluidization behaviors. Group A particles are small ($20 - 100$ μm) and have a density of less than 1.4 g/cm^3. These beds expand substantially after incipient fluidization before bubbling fluidization begins. Group B particles range in size from $40 - 500 \mu m$ and range in density from $1.4 - 4$ g/cm^3. These fluidized beds begin to bubble immediately after incipient fluidization. Particle circulation occurs due to the presence of bubbles, with bubbles bursting as discrete entities at the bed surface. Group C systems contain cohesive forces between particles. This can be due to Van der Waals forces, electrostatic forces or the presence of a wet or sticky material. These systems are difficult to fluidize, as the interparticle forces are greater than those exerted by the gas on the particle. These powders lift as a plug (in small tubes) or develop stable channels for the gas flow. These systems can be fluidized by introducing external agitation or stirring, resulting in clumped particle fluidization [12]. Finally, Group D systems contain very dense or large particles (above 500 μm). This system differs from a group B system in that the bubbles that are formed in a group D system move more slowly than the interstitial fluid. This allows gas to flow into the bottom of the bubbles and out the top.

At higher gas velocities, bed density decreases and turbulence increases for all groups, leading to the development of slugs. Group A slugs break down into a turbulent regime with a further increase in gas velocity. Eventually, increase in gas velocity results in solids being carried out of the bed [9].

Mixing of solids occurs most efficiently during bubbling fluidization. Additionally, circulation of particles results in efficient solids mixing prior to bubble formation in Group A particles [11]. The presence of aggregating particles can result in a lower static bed with a fluidized bed above, due to higher solids volume fractions below or unequal distribution of sticky feed [12].

There are several advantages that make fluidized beds beneficial to use in industrial applications. There is significant contact between the particles and the gas, allowing for good mass and heat transfer between phases [9]. Additionally, mixing occurs quickly due to a large number of particle-particle collisions, resulting in rapid temperature and product distribution throughout the bed. There are, however, a few disadvantages and challenges with fluidized beds. There is significant non-uniformity with regards to residence times due to efficient mixing, leading to low conversion rates and making the scale-up difficult to predict. Additionally, high solid particle velocities can lead to erosion of the internal elements of the system. With the addition of small volumes of liquid into a fluidized bed, the problem of aggregate formation becomes an issue.

The main focus of this work is two fold. First, the spreading of liquid through a gas-solid fluidized bed due to the motion of particles and particle-particle collisions is examined. Second, aggregation due to the formation of liquid bridges between particles in a gas-fluidized bed is studied.

Fluidized beds have been implemented in a wide range of industrial applications including heat transfer, drying, sublimation, adsorption, coating, granulation and various heterogeneous catalytic and non-catalytic gas-phase reactions [3]. The presence of liquid in a fluidized bed is essential for many of these processes. However, it can significantly alter the fluidization characteristics [13].

2.1.1 Simulations of Wet Fluidized Beds

While the majority of simulation work involving aggregation due to liquid bridges is for the application of rotating drums or granulators [14–16], there has been some work regarding gas-solid fluidized beds with wet particles for the application of fluid coking. The work of Pougatch [17] focuses on the injection of liquid into a gas-solid fluidized bed rather than on the mechanism for liquid spreading and aggregation due to particle-particle collisions.

Dosta et al. [18] performed multi-scale simulations of solid-gas fluidized beds with liquid for granulation, taking into account both heat and mass transfer processes. At the micro-scale, they applied a discrete element method (DEM) model for the particles and a computational fluid dynamics (CFD) model for the gas, with an additional capillary and viscous force as well as a decreased restitution coefficient to deal with energy loss due to the liquid. The DEM and CFD are coupled though the transfer of cell porosity and drag force/pressure information, respectively. Therefore, the gas-particle dynamics are not fully resolved. One distinct difference compared to this work is that they do not assume that particles are completely wetted. Rather, a fraction of the particle surface contains liquid. A probability variable is introduced in the meso-scale simulations for the type of collision based on the wetted surface fraction. If a wet collision takes place, the separation distance criteria used by Dosta et al. is that of twice the initial film thickness. Their meso-scale simulations combine macro-scale properties (suspension mass flow, temperature of all streams) and micro-scale particle positions and velocities (assumed to repeat cyclically due to differing time scales). They introduce a simplified nozzle model to determine the wetting of the particles, and examine mass and heat transfer amongst the three phases. The macro-scale model is a flow sheet simulation, determining particle size distribution (PSD) and temperature over time.

Mikami et al. [13] performed macro-scale simulations, and showed the effect of aggregation due to liquid presence for 0.27 wt. % water. While visually aggregation was observed, analysis of the aggregate sizes were not presented. This work additionally considered soft sphere collisions. They found that the minimum fluidization velocity for wet particles was higher than for dry particles, which is consistent for the formation of aggregates.

None of the work described above shows results dependent on the liquid surface tension and viscosity. The work of Darabi [3] focuses on particle collision induced aggregation. They develop a coalescence model based on an overall coefficient of restitution in order to determine a critical velocity for collision outcomes (rebound or stick). Liquid surface tension and viscosity effects are both taken into account.

Following this, aggregation tendency is determined by incorporating a time and temperature dependency on film thickness and liquid viscosity. This resulting restitution coefficient is used to study interactions between wet particles in a fluidized bed. The results of this work are useful due to the broad range of variables. Surface tension, liquid viscosity, film thickness, and gas velocity were all varied, allowing for a range of trends to be observed. While the scale of these simulations is significantly different from those presented in this work, this work allows for good qualitative comparison.

To date, fully resolved simulations of fluidized beds with liquid wetting have not been performed. Large-scale simulations require assumptions and simplifications to be made with regards to the small-scale gas-solid interactions. The additional presence of liquid on the particles results in a significant increase in complexity. To model this liquid properly, understanding of how quickly liquid spreads and the relative forces between particles due to the liquid need to be understood. The effects of the liquid at the small scale can lead to better understanding of aggregate size distributions at higher scales.

Fully-resolved simulations of a gas-fluidized bed are performed. The spreading of liquid is modeled, with the development of a liquid property dependent spreading rule. This allows for small-scale phenomena to be examined, while taking into account the often ignored liquid properties.

2.2 Governing Equations for Fluidization

The motion of solid and gas within a fluidized bed is governed by a set of equations, which are coupled through a gas-solid force term.

The gas phase is treated as a continuum, characterized by a local mass density

$\rho_g(\mathbf{x},t)$ and local velocity $\mathbf{u}(\mathbf{x},t)$ at position $\mathbf{x}$ and time t. Mass conservation is then specified by Equation (2.1) [19].

$$\frac{\partial \rho_g}{\partial t} + \nabla \cdot (\rho_g \mathbf{u}) = 0 \tag{2.1}$$

Similarly, momentum conservation is derived from Newton's second law of motion, which states that the rate of change of momentum is equal to the net force acting on a body. The fluidizing gas is Newtonian, with dynamic viscosity μ_g.

$$\frac{\partial\left(\rho_g \mathbf{u}\right)}{\partial t} + \nabla \cdot (\rho_g \mathbf{u}\mathbf{u}) = -\nabla \cdot (P\bar{\mathbf{I}}) + \rho_g \mathbf{g} + \nabla \cdot \overline{\tau_g} + \sum \mathbf{f} \tag{2.2}$$

P is the pressure, $\bar{\mathbf{I}}$ is the identity matrix, $\overline{\tau_g}$ is the gas viscous stress tensor (defined in Equation (2.3) [19]), and $\mathbf{f}$ represents body and surface forces acting on the gas (in this case the momentum transfer between the solid and gas phases due to drag and pressure gradients).

$$\overline{\tau_g} = \mu_g \left[\nabla \mathbf{u} + (\nabla \mathbf{u})^T\right] - \frac{2}{3}\mu_g (\nabla \cdot \mathbf{u})\bar{\mathbf{I}} \tag{2.3}$$

For an incompressible gas with a constant viscosity, Equation (2.2) simplifies to the Navier-Stokes Equation.

$$\rho_g\left(\frac{\partial}{\partial t} + \mathbf{u} \cdot \nabla\right)\mathbf{u} = -\nabla \cdot (P\bar{\mathbf{I}}) + \rho_g \mathbf{g} + \mu_g \nabla^2 \mathbf{u} + \sum \mathbf{f} \tag{2.4}$$

In this work, Equation (2.4) is solved indirectly for the gas phase through the discretized Boltzmann equation. Details of the numerical method are discussed in Section 2.4.1.

The conservation of momentum for the particulate phase is treated with a Lagrangian approach. The governing equations for translational and rotational motion of particle i are shown in Equations (2.5) and (2.7) [20].

$$m_i \frac{d\mathbf{v}_i}{dt} = \sum_j \mathbf{F}_{ij,co} + \sum_k \mathbf{F}_{ik,nco} + \mathbf{F}_{i,d} + \mathbf{F}_{i,b} \tag{2.5}$$

Here, m is the particle mass and $\mathbf{v}$ is the translational particle velocity. The first force term applies to contact forces (co) acting on particle i from particle j. This is followed by the non-contact forces (nco) acting on i due to the effect of particle k, such as those due to liquid bridges. The third and fourth terms are the gas-particle interaction force (due to drag and pressure gradients in the flow) and gravitational (or buoyant b) force, respectively. The angular momentum conservation is as follows. $\mathbf{I}_i$ is the moment of inertia, ω is the angular velocity and $\mathbf{M}_{i,j}$ is the torque acting on the particle due to other particles j and the gas, respectively.

$$\mathbf{I}_i \frac{d\omega_i}{dt} = \sum_j \mathbf{M}_{ij} + \mathbf{M}_{i,d} - \omega_i \times (\mathbf{I}_i \omega_i) \tag{2.6}$$

Due to the rotational symmetry of spherical particles, the last term in Equation (2.6) is zero and the moment of inertia becomes a scalar. This results in Equation (2.7).

$$I_i \frac{d\omega_i}{dt} = \sum_j \mathbf{M}_{ij} + \mathbf{M}_{i,d} \tag{2.7}$$

2.2.1 Particle-Particle Collisions

Discrete particle models originate from molecular dynamics methods, introduced by Alder and Wainwright [21]. These techniques can be modified and applied to granular systems.

There are two approaches for dealing with solid collisions: the hard sphere approach and the soft sphere approach. In the hard sphere approach (also known as event-driven), each particle-particle collision is assumed to occur instantaneously upon contact of the surfaces. Only binary collisions are considered. This approach was first used by Campbell and Brennen [22].

The soft sphere approach (also known as time-driven) allows for multiple collisions to occur simultaneously by extending the time in which particles collide. Particles are allowed to overlap, mimicking minor deformation and applying a related force to the particles. The net force is calculated based on the summation of forces for all binary collisions involved [23].

Hard sphere collision approaches are generally more efficient in dilute systems of particles. Additionally, this approach is more physically realistic for inelastic particles. However, hard sphere collisions are generally problematic in dense systems, where the collision frequency is high. Since only binary collisions are considered in this method, the jamming of particles breaks down the hard-sphere approach [24]. Generally, soft sphere collisions are considered in dense systems.

Even though dense systems of particles (solids volume fraction $\phi = 0.3 - 0.55$) are considered, the hard sphere collision approach is employed. This is acceptable because the simulation time and length scales are small, resulting in low particle velocities and therefore low numbers of collisions per time step. The implementation of this approach is now discussed.

The particle velocities are updated every time step. When two particles are expected to collide within a time step, all the particles are moved the sub-time step until the two particles are in contact [25]. At that point the collision is treated: the velocities for the two particles involved are updated (Equations (2.8) and (2.9)) [26]. The particles are then moved until the next collision event or the end of the time step Δt. Since monosized spheres are considered, the particle diameter D is constant.

$$
\begin{aligned}
\mathbf{v}_{i,new} &= \mathbf{v}_{i,old} + \frac{\mathbf{J}_i}{m_i} \\
\mathbf{v}_{j,new} &= \mathbf{v}_{j,old} - \frac{\mathbf{J}_i}{m_j}
\end{aligned}
\tag{2.8}
$$

$$
\begin{aligned}
\omega_{i,new} &= \omega_{i,old} + \frac{D}{2I_i}\mathbf{e}_n \times \mathbf{J}_i \\
\omega_{j,new} &= \omega_{j,old} + \frac{D}{2I_j}\mathbf{e}_n \times \mathbf{J}_i
\end{aligned}
\tag{2.9}
$$

$\mathbf{J}_i$ is the impulse exerted on particle i, the normal unit vector $\mathbf{e}_n$ runs from particle i to j through their point of contact $\left(\mathbf{e}_n = \frac{\mathbf{x}_i - \mathbf{x}_j}{|\mathbf{x}_i - \mathbf{x}_j|}\right)$.

When particles interact, they dissipate kinetic energy due to surface friction and material compression/deformation. The collision approach of Yamamoto et al. [26], implemented in this work, has two parameters that control the dissipative effects: a restitution coefficient e and a friction coefficient f_s. Both of these parameters affect the impulse force exerted on the particles. The restitution coefficient determines the momentum loss normal to the collision. The friction coefficient is the ratio of frictional force compared to the normal force.

The impulse $\mathbf{J}$ is the summation of the normal (n) and tangential (t) components ($\mathbf{J} = J_n\mathbf{e}_n + J_t\mathbf{e}_t$). The tangential component lies in the direction of the slip velocity of particle j relative to particle i. These components are defined in Equations (2.10) and (2.11) [26].

$$
J_n = (1+e)m(\mathbf{v}_{j,old} - \mathbf{v}_{i,old}) \cdot \mathbf{e}_n \tag{2.10}
$$

$$J_t = min\left[-f_s J_n, \frac{2}{7}m|\mathbf{v}_{sl}|\right] \tag{2.11}$$

$\mathbf{v}_{sl}$ is the slip velocity between particle surfaces. This work considers the idealized case of fully elastic frictionless collisions. For simplicity, the restitution coefficient is set to one and the friction coefficient is set to zero, representing rigid and perfectly smooth particles respectively. The effect of these parameter choices is not examined in this work. Simulations to date have examined a range of parameters, with the restitution coefficient being varied from 0.7 to 1.0 [13; 14; 27; 28]. Van der Hoef et al. [24] conducted an examination of the impact of both the friction factor and restitution coefficient on gas-fluidization, and concluded that the introduction of energy dissipation promoted heterogeneity, while the introduction of friction showed a slug-types fluidization.

2.2.2 Body Forces in Fluidization

One of the characteristics of a fluidized bed is the ability to separate components based on density. This buoyancy effect is present for both the solid and the fluid. The force $\mathbf{F}_{i,b}$ acting on particle i due to gravitational acceleration g is given by Equation (2.12). The solid density is ρ_s and the domain averaged density is ρ_m.

$$\mathbf{F}_{i,b} = -(\rho_s - \rho_m)\frac{\pi}{6}D^3 g\mathbf{e}_z \tag{2.12}$$

The domain averaged density ρ_m is defined as follows.

$$\rho_m = \phi\rho_s + (1-\phi)\rho_g \tag{2.13}$$

In a physical non-circulating fluidized bed, the gravitational force on the particles is balanced by the upward forces due to drag, buoyancy, and pressure drop. At the bottom of the bed, particles are pushed upwards by high gas velocities and pressure gradients, with a balancing effect from particles above and gravity. Moving up through the bed, the solids volume fraction ϕ decreases. Therefore, based on the volume-averaged continuity for the incompressible gas phase at steady state ($\nabla \cdot [(1-\phi)\mathbf{u}] = 0$), the gas velocity decreases. This reduced gas velocity leads to reduced drag on the particles, and eventually the gravitational forces overcome the drag forces. If the gravitational forces do not overcome the drag on the particles, entrainment occurs and there is a net motion of particles out of the bed. Conversely, if the downward forces dominate, the particles settle to the bottom and fluidization is not achieved.

Our simulations differ from the physical system in a few ways. The pressure gradient is not explicitly included in the simulations, due to the presence of periodic boundary conditions (see Section 2.4.4 for details). Additionally, the size of the simulation domain limits the study to a small portion of the overall fluidized bed. Because of this, the effect of changes in gas velocity, pressure, and solids volume fraction over the bed height cannot be captured in a single simulation.

In order to balance the forces within the system, a buoyant body force $\mathbf{F}_{g,b}$ is applied to the gas.

$$\mathbf{F}_{g,b} = (\rho_m - \rho_g) V_g g \mathbf{e}_z \tag{2.14}$$

The applied body forces on the particles and the fluid result in a net downward motion of the particles and net upward motion of the gas. By considering slip velocity rather than particle and gas velocity, the reference frame is implicitly treated as that of a fluidized bed, with no net particle motion and an increased gas velocity compared to particle settling.

2.3 Wetted Particles in Fluidization

Particle-particle collisions are of interest as they are the mechanism of liquid spreading considered in this work. The particle translational and rotational momentum are conserved as per Equations (2.5) and (2.6). These equations take into account the physics of the particle-particle collisions. This section is devoted to understanding the role that these collisions have in the spreading of liquid through the fluidized bed.

This section begins by describing the various mechanisms for liquid spreading. Following this, an overview of current liquid spreading models is presented, and a novel liquid spreading model is introduced. Following this, the forces between particles due to the presence of liquid are discussed.

2.3.1 Liquid Spreading

Liquid is spread within a fluidized bed through three main mechanisms. The first is through the motion of liquid droplets in the bed. Liquid is injected into the bed along with compressed steam through injection nozzles. Close to injection, the large pressure drop results in the expansion of the steam, breaking up the continuous liquid phase into a fine spray that then coats nearby particles [17]. The other two mechanisms for transferring liquid between particles become more important far from the liquid nozzles. The collision between wet and dry particles leads to wetting of the previously dry particles. Additionally, motion of the wet particles throughout the bed work to distribute liquid. In this work, only the last two mechanisms of liquid spreading are of interest.

For perfectly wetting particles, the presence of liquid results in the formation of a thin liquid layer on the particle surface. Upon interaction of the liquid layer with an adjacent dry particle or particle liquid film, a liquid bridge is formed. For liquid to spread due to particle-particle interactions, a liquid bridge grows between the particles and subsequently ruptures as the particles move apart post-collision.

At low liquid saturations, the bridges created are in a pendular state (< 9.2 % by mass liquid to solid [29]), where primary particles are held together by discrete liquid bridges separated by gas. At the other extreme, fully saturated bonds result in a capillary state (≥ 26.7 % by mass liquid to solid). This is when there are no voids in the liquid between particles. The intermediate state to this is known as the funicular state [30]. This work considers only low liquid saturations, resulting in pendular liquid bridges between two particles.

This liquid bridge grows with time until the Gibbs free energy is minimized [31]. The growth rate and eventual volume of this liquid bridge depends on the interplay between relevant forces, namely viscous forces, capillary forces, and inertial forces. By determining the rate law for liquid bridge growth, an overall liquid bridge volume can be determined. Upon bridge rupture, for two monosized spheres with the same contact angle, the liquid within the bridge will be split evenly. There are several methods that are commonly used to determine liquid spreading. These are discussed below.

Current Liquid Spreading Models

To date, there is little literature regarding the liquid bridge growth rate for pendular particle-particle liquid bridges. Liquid bridge volumes are generally assumed constant over the interaction time of two particle liquid films, varying for some models only with the introduction of a third particle interaction.

Macroscopically, laws can be determined in order to estimate the net spreading effect of wet particle motion and wet particle-particle collisions, allowing for collisions to be treated implicitly. Pougatch [17] defined an effective diffusion coefficient as the sum of the diffusion due to the random motion of particles and the diffusion due to liquid exchange during collisions. A diffusion for liquid exchange was derived by Pougatch, and the diffusion due to motion of particles was derived by Hsiau and Hunt [32]. This work was done for the area near the injection nozzles.

Microscopically, the effects of individual collisions can be examined to determine how liquid propagates during individual particle-particle interactions. The details regarding the fluid flow into the bridge immediately after bridge formation are complicated. Because of this, assumptions regarding the liquid bridge volume must be made.

The most common assumption used for the liquid bridge volume is that of full mobility of the liquid, as in the work of Liu et al. [15] and Mani et al. [33]. All the liquid on a particle is involved in the liquid bridge. Additionally, for aggregates of more than 2 particles, the liquid present on all particles in that aggregate is equally distributed amongst the liquid bridges. This is demonstrated in Figure 2.1.

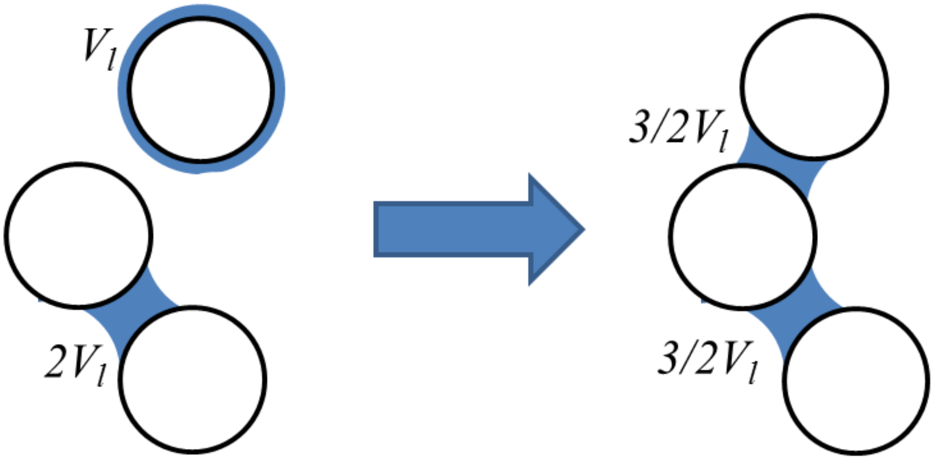

Figure 2.1: Liquid distribution between particles assuming equal spreading.

Geometrical considerations are often used to determine liquid bridge volume, as in the work of Soulie et al. [34]. In order to limit the liquid mobility on the particles, Shi and McCarthy [16] used a spherical cap approximation. This approximation limits the bridge volume to that of the liquid present on a spherical cap, which is defined based on the particle radii as shown in Figure 2.2 [16].

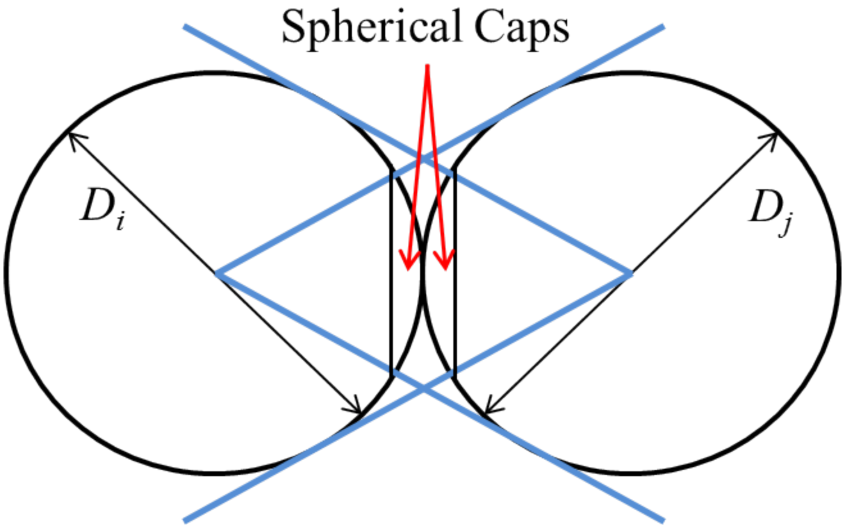

Figure 2.2: Geometry determining spherical cap size, reproduced from [16].

This model uses Equation (2.15) to calculate the contribution of liquid from one particle i into the liquid bridge for the bridge connecting particle i and j. δ_i is the liquid film thickness on particle i.

$$V_{lb,i} = \delta_i \frac{\pi}{2} D_i^2 \left[1 - \sqrt{1 - \left(\frac{D_j}{D_i + D_j} \right)^2} \right] \tag{2.15}$$

The total liquid bridge volume is the sum of the two contributions from Equation (2.15). For monosized spheres, this equation further reduces to $V_{lb,i} = \delta_i \frac{\pi}{2} D_i^2 \left[1 - \sqrt{\frac{3}{4}} \right]$.

Many works are available that consider liquid bridge volumes dependent on the particle size [35–37]. The works to date make the assumption that liquid bridges grow and reach a final volume instantaneously upon bridge formation. However, over small time scales and high liquid viscosities, the time scales of bridge growth may not be negligible. Additionally, the bridge growth will vary depending on the liquid properties and inertial characteristics. These differences cannot be captured with a geometrical approximation of the liquid bridge volume.

While there is a lack of research regarding liquid bridge growth for particle-particle interactions, there is a plethora of information regarding liquid bridge formation resulting in the coalescence of drops. Duchemin et al. [38] determined a growth rate law in the inertial regime, while Gross et al. [39] did the same for the viscous regime. Experiments have additionally been performed to determine the crossover between regimes [40].

The applied model is based on the work of Gross et al. [39], and is described in the next section. For comparison, the spreading models of Liu et al. [15] and Shi and McCarthy [16] are additionally examined.

2.3.2 Interaction-time Dependent Spreading Model

This thesis applies the scaling procedure of Gross et al. [39] for the evolution of a liquid bridge in the viscous dominant regime.

Assume that the dominant forces in the bridge growth are that of surface tension σ and liquid viscosity μ_l. This assumption negates the effect of the relative particle velocities in bridge growth, and is valid when inertial effects are small. With this assumption, a characteristic velocity scale is given as the capillary velocity (Equation (2.16)).

$$u_c = \frac{\sigma}{\mu_l} \tag{2.16}$$

Defining the internal radius of the liquid bridge as b (Figure 2.3), the capillary Reynolds number for bridge growth can be defined as follows.

$$Re_c = \frac{\rho_l u_c b}{\mu_l} = \frac{\rho_l \sigma b}{\mu_l^2} \tag{2.17}$$

The viscous regime is then defined as $Re_c \ll 1$. The momentum balance is then described using a modified version of the Navier-Stokes equations, assuming negligible inertial forces. These are the Stokes equations, described for a constant density liquid with no external body force as follows.

$$\nabla P = \mu_l \nabla^2 \mathbf{u}_l \tag{2.18}$$

With continuity as follows:

$$\nabla \cdot \mathbf{u}_l = 0 \tag{2.19}$$

To determine the range of parameters to remain within the bounds of viscous bridge growth, a maximum bridge radius b_{max} is defined, where $b_{max} = \frac{D}{2}$. By limiting the Reynolds number to significantly less than 1 in Equation (2.17), the surface tension and viscosity are chosen within the ranges of the viscous growth model.

$$Re = \frac{\rho_l \sigma \frac{D}{2}}{\mu_l^2} \ll 1 \tag{2.20}$$

A scaling analysis from Gross et al. [39] results in a relation for the viscous bridge growth rate over time. For the scaling procedure, any rigid translational effect of the particles is neglected, resulting in no dependence on the liquid displaced due to the particle velocity. To date, the translational effect of the particles on the growth of the liquid bridge radius b has not been studied. Therefore, the error associated with this assumption cannot be determined.

The stresses due to the gas are additionally neglected. Focusing in the radial direction of bridge growth (r in Figure 2.3), continuity states that at the meniscus ($r = b$) the liquid flow velocity is determined by the motion of the bridge ($u_b = \frac{db}{dt}$). For liquid bridge diameters significantly smaller than the particle radius, the following geometrical simplification can be made for the external radius of curvature R_{ext}.

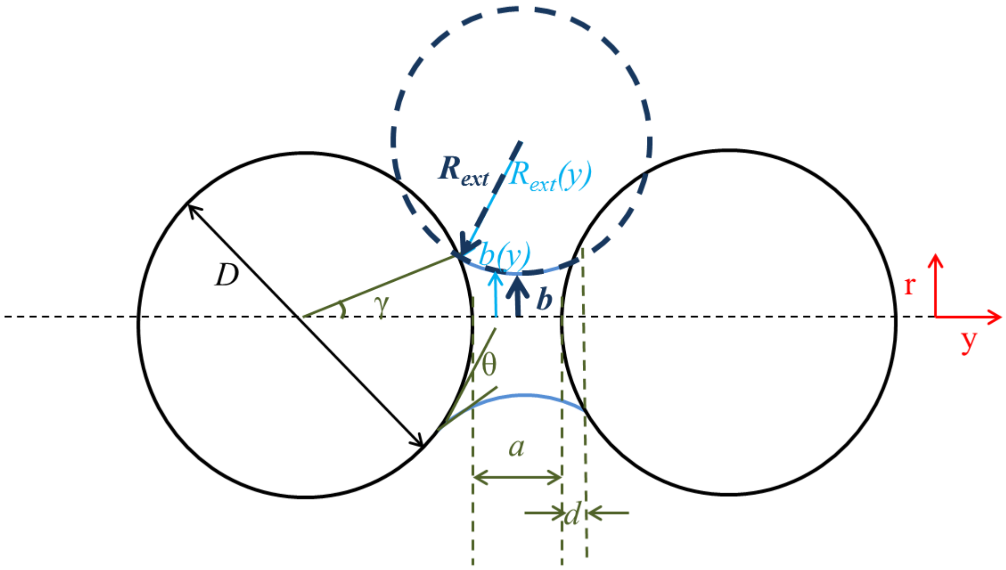

Figure 2.3: Definitions in liquid bridge geometry. The light blue (non-bolded) represents the curvatures prior to the toroidal approximation described in Section 2.3.3 (functions of y). Dark blue (bolded) represents variables with the toroidal approximation. Figure parameter scales are not typical, with the extension of the separation distance to clarify the definition of variables.

$$R_{ext} = \frac{b^2}{D}\frac{1}{1-\frac{2b}{D}} \approx \frac{b^2}{D} \tag{2.21}$$

From Equation (2.18), the following simplifications are made.

(1) The pressure is assumed to vary from a reference of zero to the Young-Laplace pressure (Equation (2.22)) at the surface.

$$\Delta P = \sigma\left(\frac{1}{b(y)} - \frac{1}{R_{ext}(y)}\right) \tag{2.22}$$

For liquid bridges beyond an initial time, b is greater than R_{ext}. Therefore, the pressure term can be approximated as:

$$\frac{\partial P}{\partial r} \approx \Delta P/b = -\frac{\sigma}{R_{ext} b} \tag{2.23}$$

(2) The velocity is assumed to vary smoothly (parabolically) between the center of the bridge (in the direction of b) and the surface. Symmetry enforces $u_l \approx 0$ at the bridge center.

$$\frac{\partial^2 u_l}{\partial r^2} \sim -u_b/b^2 \tag{2.24}$$

Applying these simplifications and Equation (2.21) to the Stokes equations (Equations (2.18) and (2.19)) in the radial direction yields the relation in Equation (2.25).

$$\frac{db}{dt} = \frac{D\sigma}{\mu_l}\frac{1}{b} \tag{2.25}$$

Integrating Equation (2.25) yields Equation (2.26).

$$b(t)^2 - b_0^2 = \frac{D^2}{4}\frac{t-t_o}{\tau_v} \qquad \tau_v = \frac{\mu_l D}{8\sigma} \tag{2.26}$$

The integration constant b_0 can be neglected at later times in the evolution, since at the initial point of bridge formation ($t \approx 0$), the bridge radius b is negligible. Therefore, the growth law is expressed as follows.

$$\frac{2b(t)}{D} \sim \sqrt{\frac{t}{\tau_v}} \tag{2.27}$$

Based on Equation (2.27) and the numerical investigation of Gross et al. [39] Figure 4, the proportionality factor is determined, resulting in Equation (2.28). This factor was consistently achieved by Gross et al. [39] for a range of capillary Reynolds numbers Re_c (0.006 - 0.05) and liquid-gas viscosity ratios μ_l/μ_g (4 - 1000), examined in the liquid bridge size range b/D of 0.075 - 0.35. The dependency on the initial drop diameter was not examined.

$$\frac{2b(t)}{D} = 0.35\sqrt{\frac{t}{\tau_v}}, \qquad \tau_v = \frac{\mu_l D}{8\sigma} \tag{2.28}$$

This equation is beneficial because it allows the effect of liquid properties to be examined with regards to bridge growth. In order to apply this equation, the time for the liquid interaction must be determined. Since the liquid film thickness is modeled as a scalar on the particle, the exchange of liquid occurs when the particles collide.

For particles i and j, with film thicknesses δ_i and δ_j, the total time available for liquid bridge growth can be approximated as the sum of the approach and rebound time through the sum of their films (Equation (2.29)). $v_{rel,n}$ is the magnitude of the relative particle velocities in the direction along the line connecting the particle centers.

$$t_{lb} = \frac{2(\delta_i + \delta_j)}{v_{rel,n}} \tag{2.29}$$

With the determination of the liquid bridge radius b and separation distance between particle surfaces a, the volume can be approximated, as discussed in the following subsection.

The stretching of the bridge is not included in the time for the collision or for the separation distance. This is because as the bridge stretches, the external radius of curvature R_{ext} increases compared to the internal radius of curvature b, which decreases. This results in a decrease in the capillary force, and eventual flipping of the Young-Laplace pressure term from attractive to repulsive. When that occurs, liquid is being expelled from the bridge during stretching, rather than being sucked into it. Upon collision of two particles, the liquid bridge volume is calculated based on $a = \delta_i + \delta_j$, and that volume is redistributed equally between the two particles.

Liquid Bridge Volume Calculation

Looking at a pair of stationary spheres, the presence of a liquid bridge requires that the Gibbs free energy of the system is minimized [31]. This ensures that the surface profile of the bridge has a mean curvature H, defined by two orthogonal principle radii of curvature. The pressure difference between the interior and exterior of the liquid bridge ΔP is then given by the Young-Laplace equation (Equation (2.22)). The challenge in determining the liquid bridge volume is in determining the profile of the liquid-gas interface, specifically in determining $b(y)$ and $R_{ext}(y)$ in Equation (2.22) as a function of separation distance. While the mean curvature H is constant, both principal radii of curvature change along the y-axis.

There are two main approaches used to obtain the liquid bridge profile between two particles. First, the Young-Laplace equation can be numerically solved to determine the liquid bridge profile. However, this solution requires a predetermined liquid bridge volume to determine ΔP, or vice versa. This method is used for known liquid bridge volumes in order to determine the pressure difference. Computationally solving the Young-Laplace equation remains impractical for applications with multiple particles and liquid bridges [31]. The other approach is to approximate the solution by simplifying the shape of the liquid bridge [41; 42]. Commonly, a toroidal approximation is made for the liquid-gas interface profile. That is, $R_{ext}(y)$ is assumed constant. With this approximation $R_{ext}(y)$ becomes R_{ext}. Additionally, while the inner bridge radius $b(y)$ remains a function of position, the neck of the liquid bridge is specified as b for use in calculations.

This approximation was first proposed by Haines [43], and has been used broadly in the study of liquid bridge force [44]. Similarly, parabolic approximations have been used by Pepin et al. [45] and Shi and McCarthy [16]. The use of the toroidal approximation to determine the liquid bridge capillary force is described in Section 2.3.3, with details in Appendix A. Both approximations introduce error, since the mean curvature is not constant along the bridge, as for example between the bridge neck ($y = 0$) and the bridge-film connection ($y = a/2 + d$).

$$\left.\left(\frac{1}{b(y)} - \frac{1}{R_{ext}}\right)\right|_{y=0} \neq \left.\left(\frac{1}{b(y)} - \frac{1}{R_{ext}}\right)\right|_{y=\frac{a}{2}+d} \tag{2.30}$$

In this work, a toroidal approximation of the liquid-gas interface is used. This solution was shown to have a maximum error of <10 % in bridge profile for concave bridges compared to the numerical evaluation of the Young-Laplace equation (2.22) [46].

While the application of the toroidal approximation allows the liquid bridge volume to be determined analytically, the solution remains complicated. By introducing a further liquid-gas interface simplification, the liquid bridge volume is determined more efficiently while still maintaining accuracy. This makes the implementation into a system with multiple particles more practical. The method of calculating liquid bridge volume is shown in Figure 2.4.

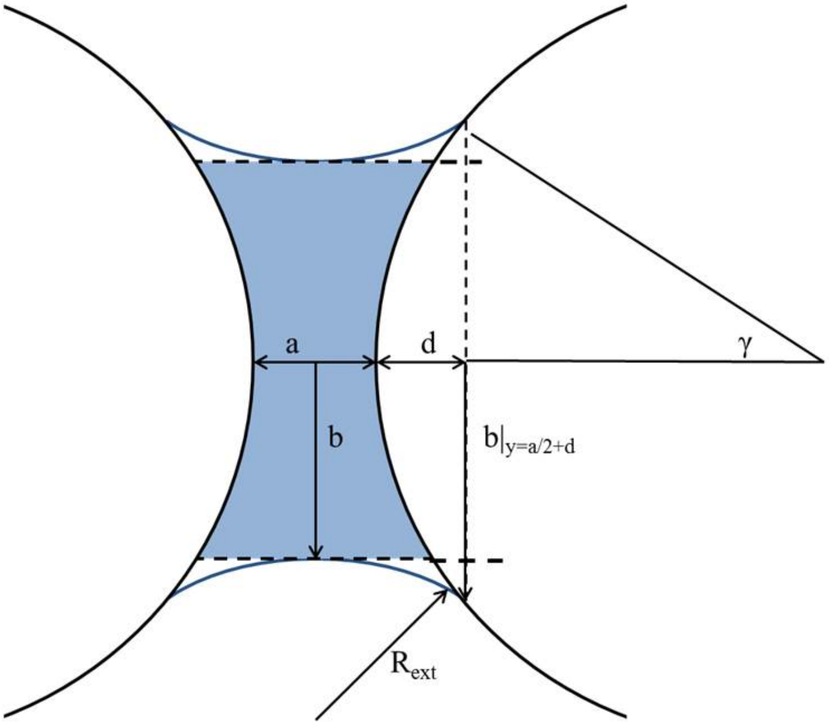

Figure 2.4: Liquid bridge volume approximation.

The volume calculation takes into account the curvature of the particles, but assumes a flat or infinite outer radius of curvature (R_{ext}). Since b is significantly greater than R_{ext}, the volume neglected by this approximation is small, resulting in an approximate 20 % difference in liquid volume for a range of separation distances of $0.1667 \leq a/D \leq 0.0008$ for bridge radii up to $b/D = 0.5$. At initial times the discrepancy in liquid bridge volume is larger, due to the small value of b compared to R_{ext}. Liquid bridge volumes for three values of a/D are presented in Figure 2.5, comparing the toroidal approximation with that used in the simulations. For the toroidal approximation, the external radius is defined through geometry, as follows for a contact angle (shown in Figure 2.3) of zero.

$$(D/2+R_{ext})^2 = (b+R_{ext})^2 + (a/2+D/2)^2 \tag{2.31}$$

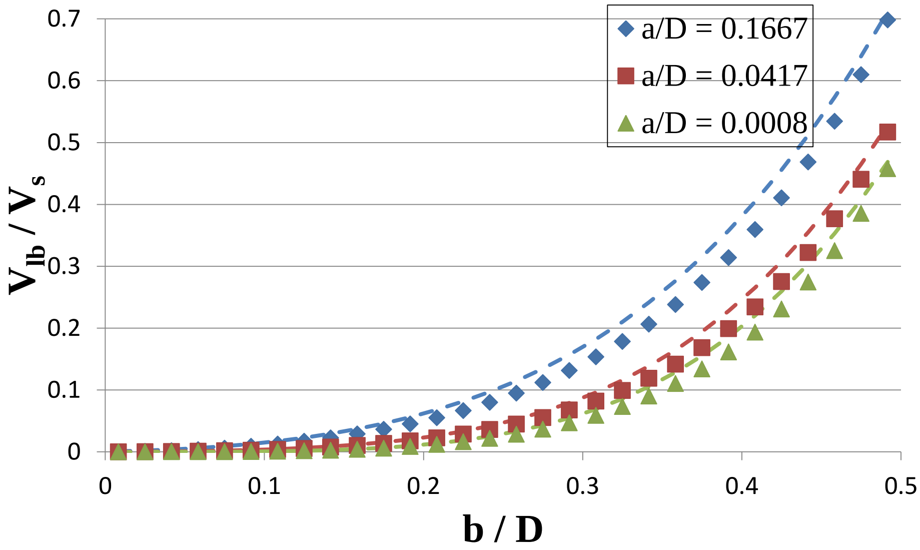

Figure 2.5: Liquid bridge volume over a range of non-dimensional liquid bridge radii b/D for three non-dimensional separation distances. Points represent the simulation value, and the dotted line represents the value based on a toroidal approximation.

This liquid bridge volume approximation used in the simulations is described mathematically as follows. The volume is treated as the cylinder with radius $b \approx b|_{a/2+d}$ (where d is the height of the spherical cap) and then the spherical cap volumes V_{sc} are removed, as shown in Equation 2.32.

$$V_{lb} = \pi b^2(a+2d) - 2V_{sc} \tag{2.32}$$

where, from geometry:

$$d = \frac{D}{2}(1-\cos\gamma) \tag{2.33}$$

$$V_{sc} = \frac{\pi d^2}{3}(\frac{3D}{2} - d) = \frac{\pi}{3}(\frac{D}{2})^3(1-\cos\gamma)^2(2+\cos\gamma) \tag{2.34}$$

γ is the half-filling angle (shown in Figure 2.3). Equation 2.32 can be expanded into Equation 2.35.

$$V_{lb} = \pi b^2 \left[a + (D - D\cos\gamma)\right] - \frac{\pi}{12} D^3 (1-\cos\gamma)^2 (2+\cos\gamma) \tag{2.35}$$

Defining γ as $\gamma = \sin^{-1}\left(\frac{2b}{D}\right)$ allows for the liquid bridge volume to be calculated based on the data available from the simulation, specifically a, b and D.

2.3.3 Forces due to Liquid Bridges

The presence of a pendular liquid bridge results in two non-contact forces between particles: a static capillary force F_c and a dynamic viscous force F_v. These two forces are discussed in this section. The direction relative to the normal motion of two particles is shown in Figure 2.6. The capillary force on a particle is especially significant, as it can be several orders of magnitude larger than the gravitational force [15].

For large liquid bridges, gravity can distort their profile. Additionally, large liquid bridge volumes can introduce a buoyant force due to the partial submergence of sections of the particle [31]. Depending on the characteristic length scale L, the gravitational and buoyancy effects become negligible [47]. The Bond number ($Bo = \frac{\rho_l g L^2}{\sigma}$) can be used to compare surface tension and gravitational effects. Using a liquid density of 1000 kg/m^3, surface tension of $\sigma = 0.005$ N/m (the smallest considered), and length scale $L = 2b_{max} = D$, the Bond number is of order 10^{-6}. Zhu et al. [20] provides a comparison of capillary, van der Waals, electrostatic and gravitational forces for various particle diameters, showing the importance of the capillary force at the hundred micron particle diameter range. Therefore, the gravitational contribution is ignored.

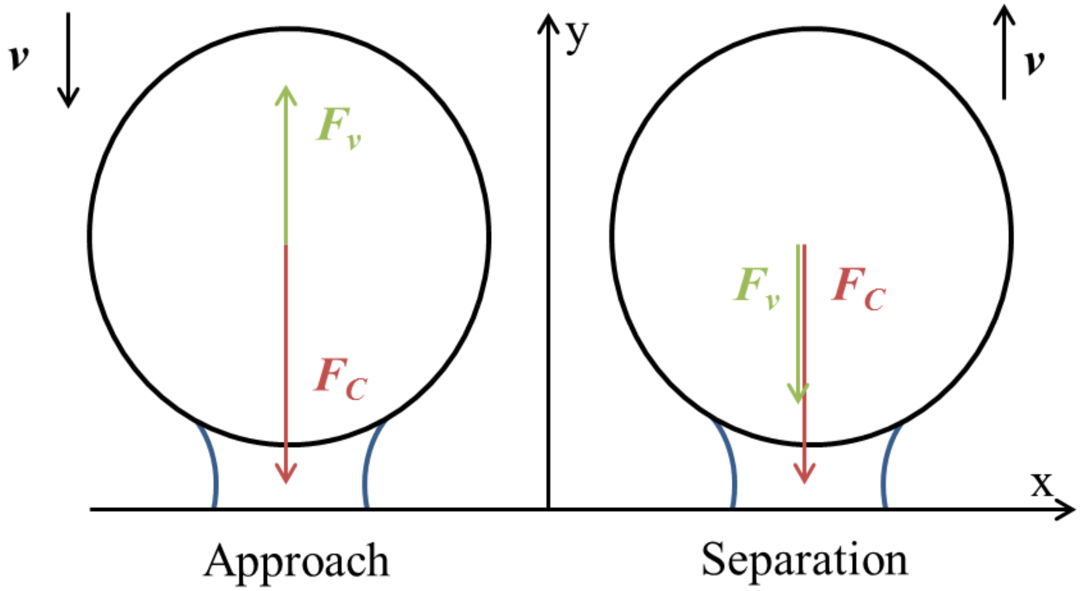

Figure 2.6: Direction of viscous and capillary forces acting on the particle upon approach and rebound. The x-axis is the plane of symmetry.

Capillary Force

The capillary force is a static force. Therefore, in order to determine its magnitude, a quasi-static assumption is made, stating that the liquid bridge profile equilibriates for each time step. Because of this, approaches of particles deviating from that shown in Figure 2.6 still experience a capillary force in the direction of their normal relative velocities. The capillary force acting on the particles due to the liquid bridge depends on the wettability of the particle surface (contact angle θ), the interfacial tension of the bridging liquid σ, the volume of the bridge V_{lb} and the interparticle separation distance a [35]. Simulations require a force model that captures these dependencies efficiently for multiple particle systems.

In Section 2.3.2, the Young-Laplace pressure was introduced. The pressure is defined as $\Delta P = P_l - P_g$. The Young-Laplace pressure can be positive or negative. For thin films, the small separation distance a usually leads to an attractive pressure differential component of the force, since $b(y) > R_{ext}(y)$. As with determining the liquid bridge volume, the challenge in determining the capillary force also lies in determining the liquid-gas interface.

The Young-Laplace equation has been numerically solved to determine the resulting capillary force [13; 34; 47].The work of Soulie et al. [34] uses a numerical approach to determine the liquid bridge volume and force, then fit a capillary force equation based on the particle radii, separation distance, and surface tension. In addition to the computational demands of this approach, the number of variables required for a thorough fit is extensive, resulting in simplifications in the fits currently available.

With the use of the toroidal approximation, and therefore varying mean curvature along the bridge length, the question arises of which distance to take in order to calculate the capillary force on the particles. Fisher [48] proposed the gorge method, which estimates the total force at the neck of the liquid bridge, using Equation (A.3).

$$\mathbf{F}_{c,gorge} = -\pi b^2 \Delta P \mathbf{e}_n \tag{2.36}$$

A competing approach is that of Adams and Perchard [49], which argues that the force should be estimated at the solid-liquid interface. This approach, known as the boundary method, results in the capillary force in Equation (2.37) [42].

$$\mathbf{F}_{c,boundary} = -\pi \left(\frac{D}{2}\right)^2 \sin(\gamma)^2 \Delta P \mathbf{e}_n \tag{2.37}$$

Here, $\Delta P = \sigma\left(\frac{1}{\frac{D}{2}\sin\gamma} - \frac{1}{R_{ext}}\right)$.

Implementation of Equations (2.36) and (2.37) remain difficult due to the unknown value of R_{ext} and γ. Work by Israelachvili [50] and Fisher and Israelachvili [48] use the boundary method to express the capillary force as a function of only separation distance a, liquid bridge volume V_{lb}, contact angle θ and particle diameter D, as shown in Equation (2.38). The derivation of this equation is presented in Appendix A.

$$\mathbf{F}_c = \pi D\sigma\cos\theta\left[1 - \frac{1}{\sqrt{1+\frac{4V_{lb}}{\pi D a^2}}}\right]\mathbf{e}_n \tag{2.38}$$

This equation has shown good agreement with experimental results [42] at separation distances up to $a/D = 0.6$ and liquid bridge volumes $V_{lb}/V_s = 1.9\times10^{-4} - 5.6\times10^{-3}$. At the lower liquid bridge volumes, Equation 2.38 showed excellent agreement. However, minor deviations were observed for higher liquid bridge volumes, specifically at low separation distances of approximately $a/D < 0.02$. This equation has been used in the multiscale fluidized simulation of Dosta et al. [18].

Finally, the range of the capillary force needs to be considered. The force is present whenever a capillary bridge is formed, meaning that a criterion for bridge rupture can be defined. From the work of Lian et al. [51], the rupture distance is defined as follows.

$$a_{rupture} = (1+0.5\theta)V_{lb}^{\frac{1}{3}} \tag{2.39}$$

Mazzone et al. [52] studied the separation of particles and eventual bridge rupture at fixed and varying velocities experimentally. They tracked the filling angle and force required to pull the particle apart using various liquids, and compared their results to three separate dissipative force models. They determined that dynamic liquid bridges are significantly stronger than static liquid bridges of the same shape when the attraction force was due to surface tension only, and that dynamic bridges stretch further before rupturing. This conclusion was also drawn by Pitois et al. [42], who similarly conducted separation experiments. They additionally observed a rupture distance dependency on the square root of the particle relative velocity.

Our aggregation model uses the liquid bridge growth calculation from Section 2.3.2 for the application of a capillary force between particles. For these simulations, the liquid cannot be treated only at the point of collision, since the sticking of particles occurs within the range of overlapping liquid bridges. This model tracks three possible events between particles:

(1) Formation of a liquid bridge
(2) Collision between particles
(3) Breakage of a liquid bridge

The particle pairings connected by liquid bridge are tracked, along with the amount of time they have been connected. During the formation of a liquid bridge (at $a = \delta_i + \delta_j$), the attractive capillary force (Equation (2.38)) is applied on each of the particles. At each time step, the capillary force due to each liquid bridge is updated (based on a new a and V_{lb} value), and applied to the relevant particles. The liquid bridge volume is calculated based on Equation (2.35), where the value of b is based on the interaction-time dependent growth rate (Equation (2.27)) and a changes based on the particle positions.

The collision step does not alter the applied liquid bridge force in any way. After collision, the particle velocities are reversed and the particles move apart. Finally, during breakage of the bridge at $a = \delta_i + \delta_j$, the capillary force between particles is removed.

Viscous Force

The viscous effect of the liquid on the particles is dependent on the motion of the particles. Adams and Perchard [49] used lubrication theory in order to determine the viscous contribution to the pendular liquid bridge force $\mathbf{F}_{v,n}$ between particles in the normal direction as in Equation (2.40).

$$\mathbf{F}_{v,n} = -\frac{3}{8}\pi\mu_l D\frac{D}{a}\mathbf{v}_{rel,n} \tag{2.40}$$

Here, the relative normal approach velocity between the particles is given by $\mathbf{v}_{rel,n}$. Similarly, the tangential component is given by Equation (2.41) [18], with relative tangential velocity $\mathbf{v}_{rel,t}$.

$$\mathbf{F}_{v,t} = -\frac{1}{2}\pi\mu_l D\mathbf{v}_{rel,t}\ln\left(1+\frac{D}{8a}\right) \tag{2.41}$$

Kim and Karilla [53] additionally examined lubrication forces in a continuous medium, and Goldman et al. [54] studied a rigid sphere parallel to a wall separated by a semi-infinite viscous fluid. Both showed a dependence of the force on $\ln\frac{D}{a}$.

The effect of viscosity is not included in this work. A comparison of the surface tension and viscosity effects can be made through the introduction of the dimensionless Capillary number, defined as $Ca = \frac{\mu|\mathbf{v}_{rel,n}|}{\sigma}$. Unfortunately, the relative velocities of particles upon collision $|\mathbf{v}_{rel,n}|$ are an output of the system, and vary substantially on solids volume fraction ϕ. The highest relative velocities occur under lower solids volume fractions. Using an average relative particle velocity obtained from simulations at $\phi = 0.3$ results in a maximum Capillary number of order 0.1. This shows that for a typical case, the capillary force is more relevant than the viscous force. However, as the separation distance grows smaller, the effect of the viscous force becomes more dominant.

2.4 Numerical Model

The numerical method covers the simulation methodology for the problem described above. This includes the method of solving the Navier-stokes equations (Equation (2.4)) indirectly through the lattice-Boltzmann method for the fluid flow, the treatment of particle-particle collisions and the interaction of the particles with the gas. The presence of a thin liquid film on the particles introduces an additional level of complexity. Therefore, the presence of liquid on the particles and relevant interactions are also discussed. Finally, the boundary conditions are discussed. The numerical model used in this work is modified from that used for non-aggregating liquid-solid systems in, for example, Derksen [55]. The models presented for gas fluidization in this section and used in this work have been applied and validated in a number of works [25; 27; 56].

2.4.1 Lattice-Boltzmann Method (LBM)

Lattice-Boltzmann is a mesoscopic kinetic theory originally developed from the theory of lattice gases [57; 58]. This method was chosen due to its ability to handle complex, moving boundaries. An extensive review of the lattice-Boltzmann method in fluid flow problems is presented by Chen and Doolen [59]. The method discretizes flow into elements of unit mass moving with unit speed along lattice edges [60]. Collisions of these elements result in the recalculation of velocities and masses along the discrete directions. These element interactions mimic the viscous behavior of a fluid [27]. From kinetic theory of lattice gases [57], the Boltzmann equation is equivalent to the Navier-Stokes equation with the proper definition of a collision operator $\Omega_i(\mathbf{N})$.

A 4-dimensional face-centered-hyper-cubic (FCHC) lattice is used in many flow simulations [61] with the 3-dimensional projection shown in Figure 2.7. The FCHC lattice has 4 dimensions, with 24 velocity directions $\mathbf{c}_i$ available at each grid point. The 3-dimensional projection has 18 possible directions ($i = 1,2,3,...18$), with weight factors w_i to represent the multiplicity of the edges caused by the projection [62]. This 3-dimensional projection is referred to as a D3Q18 projection for its 3 dimensions and 18 velocity directions. The lattice-Boltzmann equation solves for the evolution of a mass density $N_i(\mathbf{x},t)$ along a velocity direction $\mathbf{c}_i$ at position $\mathbf{x}$ and time t. N_i evolves in two steps. Streaming propagates all variables towards the nearest adjacent node along the velocity direction $\mathbf{c}_i$. Then, collision redistributes the local mass densities at each grid point. These steps are combined in the lattice-Boltzmann equation (Equation (2.42)).

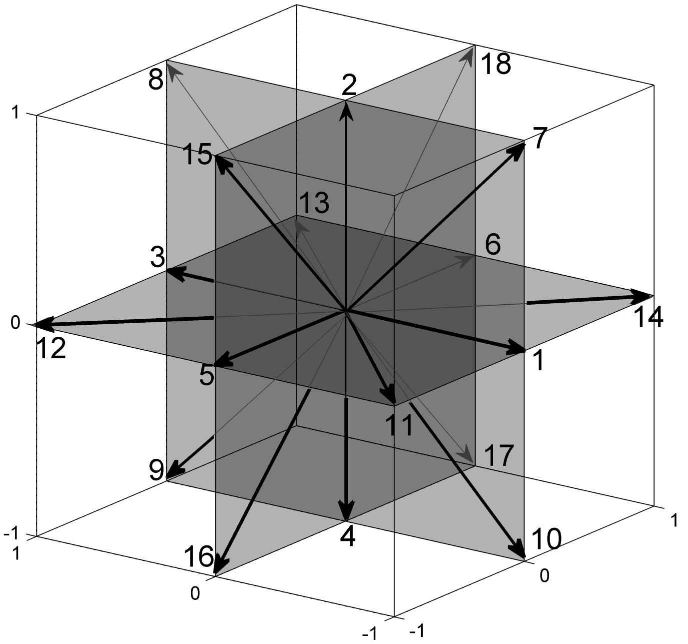

Figure 2.7: D3Q18 projection of 4D FCHC.

$$N_i(\mathbf{x}+\mathbf{c}_i,t+1) = N_i(\mathbf{x},t)+\Omega_i(\mathbf{N}) \tag{2.42}$$

Here, Ω_i is the collision operator. To ensure mass and momentum conservation, Equations (2.43) and (2.44) must be satisfied.

$$\sum_i \Omega_i = 0 \tag{2.43}$$

$$\sum_i \Omega_i \mathbf{c}_i = \mathbf{f} \tag{2.44}$$

From Equation (2.44), the **f** is the external force term used to accelerate the flow, relating to a body force such as buoyancy or gravity [60].

The macroscopic quantities ρ and $\mathbf{u}$ are obtained by summing the individual lattice direction properties, as shown in Equations (2.45) and (2.46).

$$\rho(\mathbf{x},t) = \sum_i N_i(\mathbf{x},t) \tag{2.45}$$

$$\rho(\mathbf{x},t)\mathbf{u}(\mathbf{x},t) = \sum_i \mathbf{c}_i N_i(\mathbf{x},t) \tag{2.46}$$

Further details regarding the numerical method can be found in Somers [60] and Eggels and Somers [62].

2.4.2 Particle Motion

Each time step Δt, the particle positions and velocities are updated using the explicit Euler method. The velocities are determined based on the forces and torques acting on the particles (as described in Equations (2.5) and (2.6), respectively). The particle velocity $\mathbf{v}_i$ and angular velocity ω_i for particle i are updated as follows.

$$\mathbf{v}_{i,new} = \mathbf{v}_{i,old} + \frac{\sum \mathbf{F}}{m}\Delta t \tag{2.47}$$

$$\omega_{i,new} = \omega_{i,old} + \frac{\sum \mathbf{M}}{I}\Delta t \tag{2.48}$$

The particle mass m becomes the difference between solid and internal fluid mass ($m_s - m_{int}$), due to the internal fluid effect discussed in Section 2.4.4, Equation (2.53). Similarly, the moment of inertia I becomes $I_s - I_{int}$. The moment of inertia for a sphere is given as $I = 0.1mD^2$.

The particle positions $\mathbf{x}_i$ and angular position $\mathbf{a}_i$ are updated assuming constant velocity over the time step, as follows.

$$\mathbf{x}_{i,new} = \mathbf{x}_{i,old} + \mathbf{v}_{i,new}\Delta t \tag{2.49}$$

$$\mathbf{a}_{i,new} = \mathbf{a}_{i,old} + \omega_{i,new}\Delta t \tag{2.50}$$

If a collision occurs between time steps, all particle positions are updated to the time of that collision. The collision is treated, resulting in the updating of the velocities of the colliding particles. All other particle velocities are not updated until the next full time step.

2.4.3 Liquid Modeling

In simulating multi-fluid flow, challenges arise in accurately replicating interface phenomena. Prior to liquid bridge formation, the drainage of the thin film between the two approaching liquid layers is on the order of tens of nanometers [63]. In order to model the liquid-gas interface directly in the simulations, a very fine mesh would be required, making the simulations inefficient and unfeasible considering the number of particles to be simulated. Because of this limitation, the liquid presence in the system is not directly simulated, but rather treated as a scalar on the particles. This scalar represents the thickness of the film on the particles. Thin films are used in order to minimize the error due to not resolving the liquid flow. Mono-sized, perfectly wetting spheres with a contact angle θ of zero are simulated.

The simulations performed are organized into two main sections. First a one-way coupled scenario is examined. In this scenario, particle-particle collisions are used to spread the liquid. However, the liquid does not have any effect on the particles (no attractive capillary force). The liquid acts as a passive scalar that is distributed throughout the bed through collisions.

Following this, two-way coupling is examined. In this scenario, the capillary force in Equation (2.38) is applied to the particles. The liquid presence on the particles therefore affects the fluidization dynamics. The liquid is no longer treated as a passive scalar, but rather creates an applied force between particles.

2.4.4 Boundary Conditions

This work uses a uniform lattice to calculate the hydrodynamic parameters through a collision and streaming process. At each discrete time interval a set of equations must be solved at each grid node within the domain. In order for a unique solution to be found, initial and boundary conditions are required. Common boundary conditions used in simulations are open boundaries (inlet and outlet), closed boundaries (walls), symmetric boundaries, and periodic boundaries.

The scale of industrial applications for fluidized beds, specifically coking, is of the order 10 m+. In order to fully-resolve the gas dynamics, a fine mesh size of order 10^{-5} m is required, based on a particle size of 145 μm [6] and a simulation particle diameter of $>$10 lattice units [64] (12 lattice units are used in the simulations). Computational limitations result in an overall domain size of order 10^{-3} m. Due to the large discrepancy of scales between industrial applications and the simulations, variables that change as a function of height (pressure, particle velocities, fluid velocities, solids volume fraction) will see a negligible variation over the simulation domain. This allows for the implementation of periodic boundary conditions in the vertical direction. The mechanisms considered for liquid spreading are dominant far from the sides of the reactor. This additionally allows for the consideration of periodic boundary conditions in the horizontal directions. By modifying the solids volume fraction ϕ, sections of the overall fluidized bed are implicitly examined.

The next section discusses the implementation of the solid-gas boundary for particles immersed in the flow.

Immersed Boundary Method

The development of boundary conditions that allow for a moving, curved boundary has been an ongoing area of research in LBM. A common method of handling these boundaries is the bounce-back approach. For this approach, the distribution function N_i that propagates towards a solid-fluid boundary node bounces back halfway to that node and returns back to its fluid node. The resulting force on the boundary depends on the momentum exchange at the interface [65]. The curved surface of the boundary can be treated in two ways with this method. One way is to approximate the boundary as a staircase structure following the contours of the lattices [65]. This is problematic as shifts in the object result in sudden changes to the surface. This can be remedied by interpolating the N_i populations on the curved surface based on the lattice nodes surrounding the boundary to approximate the unknown N_i populations [66].

Instead of the bounce back approach described above, a direct-forcing technique based on the method of Derksen and Van Den Akker [67] is implemented to achieve no slip at the gas-solid interface. This technique is adapted to LBM from the work on no slip boundary conditions in spectral simulations by Goldstein et. al. [68]. Instead of interfering at the mesoscopic level to alter the density distribution function N_i, this method locally alters the macroscopic fluid velocity.

The object is represented by a set of M control points at the objects surface. These points are approximately equidistant apart and at a resolution slightly higher than that of the fluid lattice resolution (Figure 2.8). The surface velocity of the solid $\mathbf{v}_j$ at node $j = (1, 2....M)$ is determined and compared to the local fluid velocity, which is determined via interpolation from surrounding fluid node velocities $\mathbf{u}_i$. From this difference, a force is calculated and applied to the surrounding nodes.

The force and torque acting on the object are determined based on Equations (2.51) and (2.52).

$$\mathbf{F}_s = -\sum_{j=1}^{M} \mathbf{F}_j(\mathbf{x}, t) \tag{2.51}$$

$$\mathbf{T}_s = \sum_{j=1}^{M} \mathbf{r}_j \times \mathbf{F}_j(\mathbf{x}, t) \tag{2.52}$$

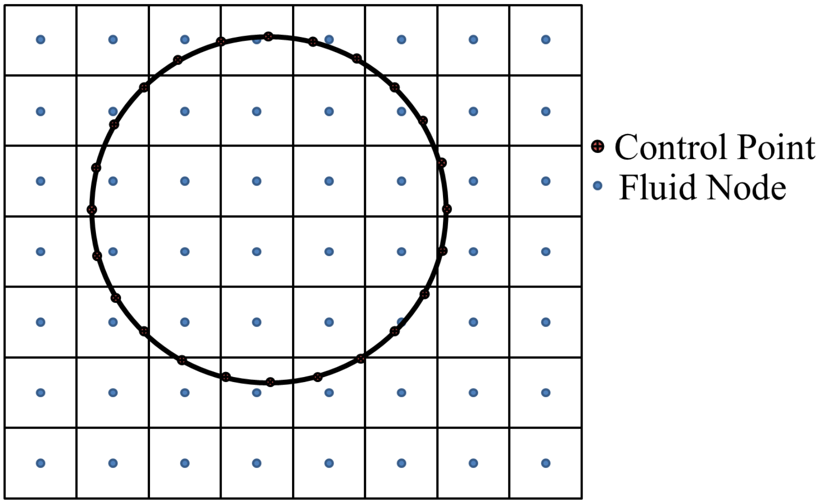

Figure 2.8: Overlap of fluid nodes and surface control points used for the immersed boundary method

The use of both a bounce-back and immersed boundary method have been shown to have an unphysical dependence of the fluid kinematic viscosity on the resulting drag force. Ladd [64] first calibrated the viscosity effect and introduced the concept of a hydrodynamic radius for the bounce-back approach. This was later done by ten Cate et al. [69] for the immersed boundary method. Due to the interpolation and extrapolation procedure between the particle nodes and fluid nodes, the fluid experiences a larger drag force in the simulation than predicted for that particle radius. Therefore, a hydrodynamic radius is chosen that is smaller than the input radius, differing by approximately one lattice spacing [69]. The calibration procedure involves simulation of a single sphere of input radius in a periodic domain at a given kinematic viscosity and determining the hydrodynamic radius required for an accurate drag force.

One characteristic of this forcing technique is the presence of fictitious fluid within the solid object. This is advantageous because when a fluid node is moved from the interior of the object to the exterior, fluid is already present and therefore the state of the node does not need to be changed [65]. However, a disadvantage of this is that the internal fluid has an effect on the external fluid by contributing to the dynamics of the particle. Suzuki and Inamuro [70] found that the effect of the internal fluid was insignificant for Reynolds numbers less than 10. However, their work was focused on significantly smaller density ratios of order 1.

A solution to this problem is described in Derksen and Sundaresan [25]. Because of the solid boundary, the internal fluid mimics the behavior of a rigid body, nearly matching the translational and rotational velocity of the surrounding object.

By treating the adaptive force $\mathbf{F}_s$ as the summation of the force exerted on the external fluid and the force to produce rigid body motion of the internal fluid, an equation for the external force can be determined. Momentum balances on the internal fluid and solid, with the inclusion of the buoyancy forces described in Equations (2.12) and (2.14), result in Equation (2.53). The rotational component is treated similarly.

$$(\rho_s - \rho_g)\frac{\pi}{6}D^3\frac{d\mathbf{v}}{dt} = -\mathbf{F}_s - (\rho_s - \rho_g)\frac{\pi}{6}D^3 g\mathbf{e}_z \tag{2.53}$$

2.4.5 Initialization

Prior to the inclusion of a capillary force, a steady-state fluidized bed must be established. The particles are initialized in a hexagonal close-packed configuration, spaced as far apart as possible given ϕ, with random velocities. They are then allowed to move freely, without the influence of the gas. The particle randomness is examined by determining the radial distribution function $g(r)$ of the particles.

The radial distribution function represents the probability of finding a particle within a shell dr at a radial distance r away from a reference particle.

The radial distribution function is significantly different for an organized and random system, as shown in Figure 2.9.

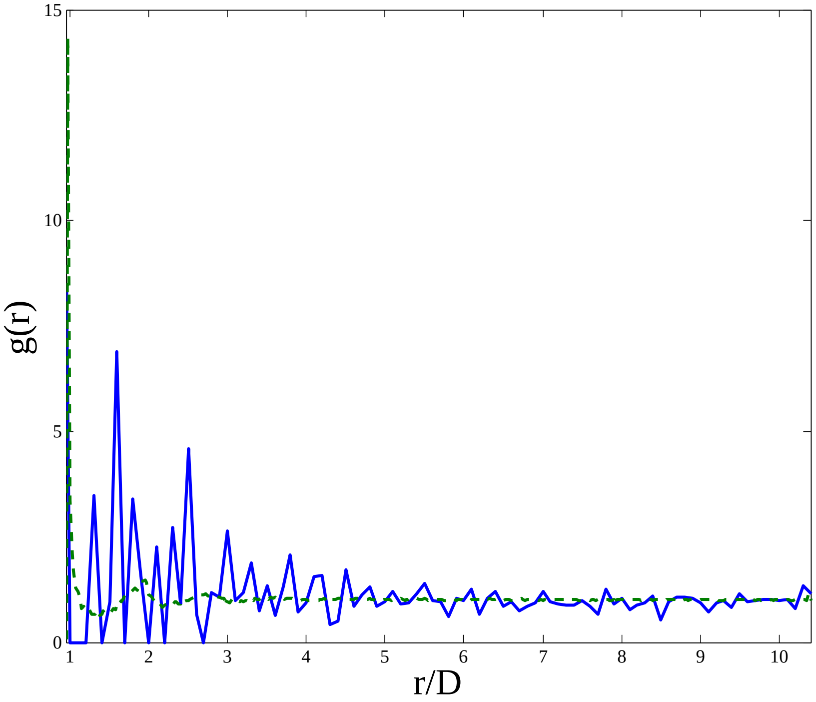

Figure 2.9: Comparison of radial distribution function $g(r)$ for random particle configuration (dotted line) and hexagonal close-packed configuration (solid line). $\phi = 0.3$.

The hexagonal close-packed configuration shows a clear preference of particle centers at specific distances, whereas the randomly distributed system shows a generally smooth decay to $g(r) = 1$, showing no preference in particle location. After the particle positions have been randomized (typically at around $tU_\infty/D = O(400)$), the gas phase is activated, and the particle velocities are set to zero. From here, the gas-solid fluidized bed is allowed to develop until a point where the frequency of collisions is stabilized. At this point, the fluidized bed is assumed to have reached its dynamic steady state. The liquid film is then initialized with specific values of surface tension, liquid viscosity, and film thickness. For the diffusion simulations, separate scalars are introduced to represent each of a set of initial conditions to be tested. For the aggregation simulations, all particles are given an identical liquid film thickness.

When simulating liquid diffusion, four different domains are considered. In order to develop the initial steady state for the rectangular domains, the cubic domain liquid-free steady state is stacked onto itself. The system is then allowed to run for $tU_\infty/D = 220$ prior to introduction of the liquid film thickness scalar.

2.4.6 Gas-Solid Fluidization Properties

To ensure the fluidization properties are consistent with those observed in a fluid coker, the characteristic dimensions (length, time, mass) are scaled based on the macro-scale observations of Song et al. [6]. The relevant properties are presented in Table 2.1 [6].

Table 2.1: Properties scaled for simulation.

Gas Density ρ_g, kg/m^3	2.28
Gas Viscosity μ_g, $Pa \cdot s$	2.5×10^{-5}
Particle Density ρ_s, kg/m^3	1600
Mean Particle Diameter D, μm	145
Density Ratio ρ_s/ρ_g, $-$	701
Archimedes Number Ar, $-$	174

A range of solids volume fractions is considered, from $\phi = 0.3$ to $\phi = 0.55$. This results in simulation domains with between 140 and 1188 particles.

Scaling is based on the following dimensionless parameters:

$$Re = f\left[Ar, \frac{\rho_s}{\rho_g}, \phi\right] \tag{2.54}$$

where Re is the particle Reynolds number ($Re = \frac{UD\rho_g}{\mu_g}$, with U the characteristic velocity scale), Ar is the Archimedes number ($Ar = \frac{gD^3\rho_g^2(\frac{\rho_s}{\rho_g}-1)}{\mu_g^2}$), the solid to gas density ratio is $\frac{\rho_s}{\rho_g}$, and the overall solids volume fraction is ϕ. The length scale chosen is the particle diameter D.

A Reynolds number is introduced based on the terminal settling velocity of a single sphere in an unbounded medium ($Re_\infty = \frac{U_\infty D \rho_g}{\mu_g}$), where the settling velocity U_∞ is calculated based on the correlation of Schiller and Naumann [71], relating the Archimedes number with the Reynolds number for $3.6 \leq Ar \leq 10^5$ (Equation (2.55)).

$$Ar_\infty = 18 Re_\infty + 2.7 Re_\infty^{1.687} \tag{2.55}$$

By implementing Re_∞, the fluidization can be completely defined using input parameters. At constant ϕ and ρ_s/ρ_g, an increase in Re_∞ will lead to an increase in Re.

For scaling to the simulation domain, it is beneficial to note that the method of Eggels and Somers [62] is applicable for certain ranges of dimensionless flow variables (based on domain units of $\Delta x = \Delta t = 1$). Specifically, $\rho_g \approx 8$ and $10^{-5} \leq \frac{\mu_g}{\rho_g} \leq 0.25$. The value of $\frac{\mu_g}{\rho_g}$ is held constant at 0.01 within the simulations.

Results are non-dimensionalized using the characteristic scales introduced, leading to a non-dimensionalized time of $\frac{tU_\infty}{D}$ and velocity of $\frac{\mathbf{u}}{U_\infty}$, $\frac{\mathbf{v}}{U_\infty}$.

2.4.7 Liquid Properties

Liquid Spreading

The addition of liquid into the gas-solid fluidized bed introduces additional variables of importance. Those variables are the liquid film thickness δ, and for the interaction-time dependent spreading model the liquid viscosity μ_l and surface tension σ. A dimensionless parameter for the liquid film thickness is $\frac{\delta}{D}$.

Using the single particle terminal settling velocity U_∞ and particle diameter D

to non-dimensionalize the viscous time scale from Equation (2.28) yields the following.

$$T_v = \frac{\mu_l U_\infty}{8\sigma} \tag{2.56}$$

This bridge growth parameter can be used to compare the effects of liquid viscosity and surface tension simultaneously. A range of T_v values from 0.40 to 11.9 is examined, with an initial non-dimensional film thickness δ/D of 0.08. These are representative of commercial systems [2; 6; 8; 72], but does not cover the full range of liquid viscosity changes. With the introduction of liquid bridge capillary force, the parameters studied change.

Aggregation due to Liquid Bridges

With the addition of a capillary force in Chapter 4, an additional non-dimensional parameter is necessary. A dimensional analysis to determine the necessary dimensionless parameters of this system is performed as follows.

For simplicity, inertial and capillary components only are considered.

$$F_c = \rho_s \frac{\pi}{6} D^3 \frac{d^2a}{dt^2} \tag{2.57}$$

Combining Equation (2.38) and Equation (2.57) in Equation (2.58), the parameters affecting aggregation are determined.

$$\rho_s \frac{\pi}{6} D^3 \frac{d^2a}{dt^2} = \pi D \sigma \left[1 - \frac{1}{\sqrt{1 + \frac{4V_{lb}}{\pi D a^2}}} \right] \tag{2.58}$$

$$a = f(D, \sigma, \mu_l, \rho_s, t) \tag{2.59}$$

This leads to the following non-dimensional parameters. Since both the liquid and solid densities are constant, the ratio of the two is used instead of the solid density. This leads to the use of the capillary Reynolds number Re_c.

$$\frac{a}{D} = f\left(\frac{\rho_s}{\rho_l}, \frac{t\sigma}{\mu_l D} = \frac{t}{\tau_v}, \frac{\rho_s \sigma D}{\mu_l^2} = Re_c \frac{\rho_s}{\rho_l}\right) \tag{2.60}$$

The last two non-dimensional groups are of significance, relating to the bridge growth rate described for liquid spreading and the capillary Reynolds number.

By non-dimensionalizing Equation (2.58), the Reynolds number is shown to be the controlling parameter for aggregation. At early times in the bridge growth, the liquid bridge volume can be approximated as $V_{lb} \approx \pi b^2 a$. Since the liquid bridge volume increases over time, the effect of the last term in Equation (2.58) decreases over the collision time. Therefore, the force equation is examined at early times, when the simplified volume expression is valid. Combining this approximation with the viscous bridge growth rate (Equation (2.28)) into Equation (2.58) yields the following.

$$\rho_s \frac{\pi}{6} D^3 \frac{d^2 a}{dt^2} = \pi D \sigma \left[1 - \frac{1}{\sqrt{1 + \frac{0.98\sigma t}{a\mu_l}}}\right] \tag{2.61}$$

Non-dimensionalizing this equation, the characteristic velocity is selected as the capillary velocity ($U = u_c = \frac{\sigma}{\mu_l}$) and a characteristic length is selected as the particle diameter ($L = D$). This results in Equation (2.62). The starred values are non-dimensional parameters.

$$\frac{d^2a^*}{dt^{*2}} = \frac{6\rho_l}{\rho_s}\frac{\mu_l^2}{D\rho_l\sigma}\left[1-\frac{1}{\sqrt{1+\frac{0.98t^*}{a^*}}}\right] \tag{2.62}$$

$$= \frac{6\rho_l}{\rho_s}\frac{1}{Re_c}\left[1-\frac{1}{\sqrt{1+\frac{0.98t^*}{a^*}}}\right] \tag{2.63}$$

For the aggregating simulations, computational resources limit the cases that can be studied. With the inclusion of a capillary force, multiple liquid properties can no longer be simulated simultaneously in one simulation, since these properties will now have an effect on the fluidization behavior. Therefore, the range of physical properties is decreased from that studied in Chapter 3.

For each solids volume fraction, an independent set of conditions is tested. Due to differences in particle proximity, leading to differences in collision frequency and particle velocities, higher solids volume fractions are expected to result in easier aggregation. Surface tension, liquid viscosity, and film thickness are modified to attempt to achieve total aggregation, no aggregation, and partial aggregation for various ϕ. The gas and solid parameters are taken from Song et al. [6], as described in Section 2.4.6. The ranges of non-dimensional liquid properties are shown in Table 2.2. The ranges of parameters used for the capillary Reynolds number fall within the range expected in commercial systems [8]. The film thickness range is representative of the lower extremes in film thickness observed commercially, with thin films being below $20\mu m$ or $\delta/D = 0.14$ [3; 8; 73].

Table 2.2: Parameter ranges for aggregation due to liquid bridges.

Capillary Reynolds Number Re_c, [-]	$2.2\times10^{-9} - 4.4\times10^{-4}$
Film Thickness δ/D, $[-]$	$8\times10^{-4} - 8\times10^{-2}$

By initializing with a homogeneously wetted system, the effect of liquid spreading is eliminated within these simulations, allowing for the aggregation behavior to be studied independently. Only the interaction-time dependent spreading model is considered in determining the liquid bridge volume for the force calculation.

2.4.8 Assumptions

In the modeling of liquid spreading and aggregation, the following assumptions are made.

- Spherical, smooth, monosized rigid particles
- Binary, elastic collisions between particles
- Coating liquid is Newtonian
- Liquid wets the particle perfectly, with a constant contact angle of zero
- Thin liquid films are applied to the particles ($\delta/D < 0.14$ [8])
- Viscous bridge growth ($Re_c << 1$)
- No external gas flow through the simulation domain

Chapter 3

Liquid Spreading due to Binary Collisions of Particles

In fluid coking, the even distribution of liquid bitumen on the particles is important for the overall efficiency of the process [8]. Liquid is spread through primary and secondary spreading. Primary spreading occurs at injection, where jet-bed interactions affect the initial mixing of liquid into the bed. Secondary spreading predominantly has an effect further from the fluid coker walls. It is the spreading of liquid through the collision of wet and dry particles, and through the random motion of wet particles in the bed.

Gray [4] hypothesized that in fluid coking, the spreading rate of liquid in the fluidized bed is dominated by primary rather than secondary spreading. The effect of primary spreading has been extensively studied [17]. However, there have been no studies to date that focus specifically on the effect of individual particle motion on liquid spreading, fully resolving the gas hydrodynamics within the fluidized bed of a fluid coker.

In order to determine the efficiency of spreading within a fluidized bed, individual particle-particle interactions need to be studied. In accordance with Section 2.3.1, the spreading of liquid between particles connected via liquid bridges has been studied and treated in various ways. However, the liquid spreading models to date are based on geometrical considerations alone [16]. There is currently no liquid spreading model that directly accounts for the properties of the liquid forming the bridge. Due to the high temperatures and ongoing reaction of the liquid phase in fluid coking, the liquid properties vary significantly over short periods of time. In this chapter, a liquid spreading model that accounts for liquid viscosity and surface tension is applied to a fluidized bed system and compared with existing liquid spreading models.

To quantify the effect of liquid spreading due to particle-particle collisions, diffusion coefficients are determined in the horizontal and vertical directions. These diffusion coefficients are obtained for three liquid spreading models: two based on geometry taken from literature and one on viscous liquid bridge growth over time. This last model allows for the liquid properties to be considered. No capillary forces are included in this chapter. Instead, this chapter focuses on a one-way coupled system, where liquid spreading due to fluidization is examined without aggregating effects. The effect of aggregation is considered in Chapter 4.

The chapter is organized as follows. First, the problem is described and the relevant equations reviewed. Following this, the implementation of the three models used for liquid spreading (introduced in Section 2.3.1) will be discussed. The analysis procedure for determining diffusion coefficients will then be outlined along with numerical and system size effects. Finally, results comparing liquid spreading models, liquid properties, solids volume fractions, and directionality will be presented.

3.1 Problem Statement

Liquid spreading is studied, quantified through the development of an effective liquid diffusion coefficient, through a fluidized bed by means of wet particle motion and collisions between wet and dry particles. The problem being considered can be described on two scales. First the small-scale interaction of two particles and the relative liquid bridge growth between those particles is discussed, resulting in liquid transfer. Then, the overall problem of the spreading of liquid due to particle-particle collisions in a fluidized bed is discussed.

3.1.1 Liquid Spreading Between Two Particles

Consider two identical solid spherical particles of diameter D approaching from opposite directions, as shown schematically in Figure 3.1a. Particles are approaching with initial translational velocities of magnitude v. The relative tangential and angular velocities of the particles are not considered for the liquid bridge dynamics. The particles i and j are fully-coated with a Newtonian liquid of thickness δ_i and δ_j.

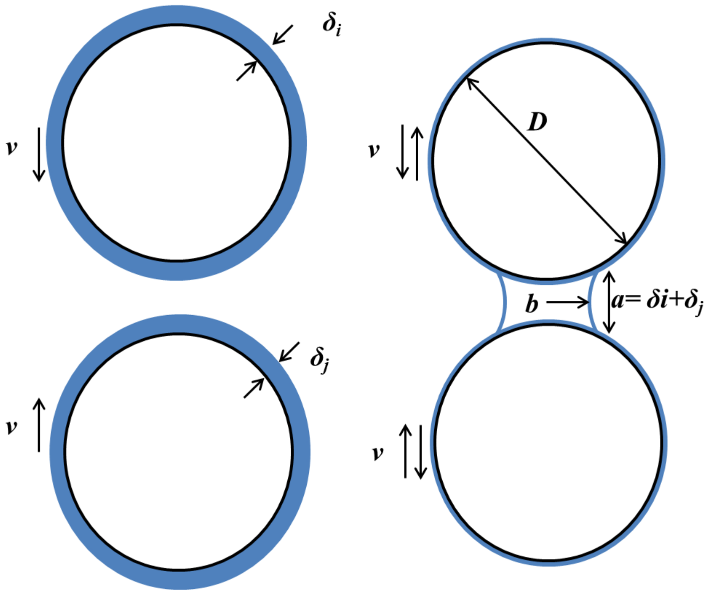

a) Particle approach.

b) Bridge formation and rupture.

Figure 3.1: Process of liquid spreading.

Once the liquid layers touch each other, a liquid bridge is formed between the particles, as shown in Figure 3.1b.

This liquid bridge grows until one of the following events:

(1) A maximum bridge diameter equal to the particle diameter is reached

(2) All the liquid on both particles has moved into the bridge

(3) The bridge ruptures

A collision can be viewed in three separate stages: approach, collision, and rebound. During the approach stage, particles move from a distance of their cumulative film thicknesses ($a = \delta_i + \delta_j$) to a distance where the particles collide ($a = 0$). The particles collide elastically, transferring momentum. Upon rebound, the particle move away from the contact position to the initial separation distance

($a = \delta_i + \delta_j$), where they separate. The liquid bridge radius grows from the point of initial contact of the films ($a = \delta_i + \delta_j$), up until the point of bridge rupture. For monosized spheres with equal contact angles θ, the rupture of the liquid bridge spreads the liquid from within the bridge equally among both particles.

3.1.2 Spreading within a Fluidized Bed

To determine the effective diffusion coefficient for liquid spreading, the fluidized bed behavior is examined. A fluidized bed is a complicated system, with inhomogeneities in gas-particle dynamics based on direction and solids volume fraction. Differences between different solids volume fraction systems in collision frequency and particle velocity fluctuations, along with the development of large-scale structures all effect how liquid moves. A schematic of a simulated fully-periodic fluidization domain of monosized spheres is shown in Figure 3.2. The solids volume fraction is defined as $\phi = N_{tot} \frac{\pi D^3}{6 N_x N_y N_z}$.

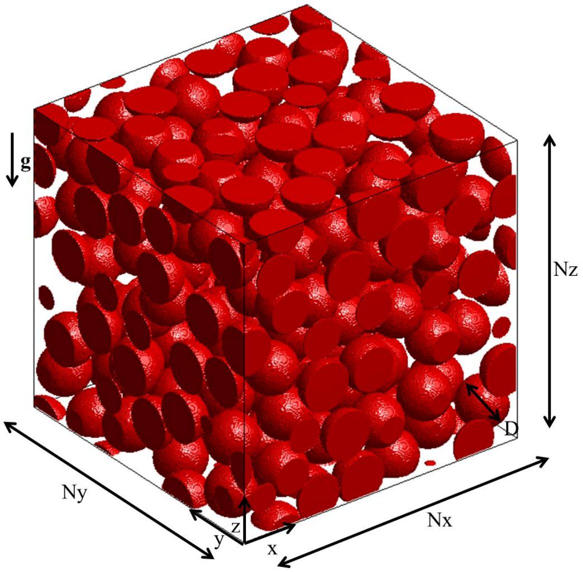

Figure 3.2: Dimensions in fully periodic simulation domain.

3.2 Model Development

This section focuses on the implementation of the three spreading rules introduced in Section 2.3.1.

3.2.1 Equal Spreading

This liquid spreading rule assumes full liquid mobility [15; 33], and is the simplest of the spreading rules considered. During particle interaction, the liquid bridge is formed instantaneously with a volume equivalent to the sum of the liquid on both interacting particles. Liquid is spread at the point of collision within the simulations, resulting in spreading only between two particles at a time. For two particles i and j with film thicknesses δ involved in a collision, the liquid bridge volume is calculated as follows.

$$V_{lb} = \pi D^2(\delta_i + \delta_j) \tag{3.1}$$

Because the particles are of the same size and wet completely, the liquid is then equally distributed, resulting in the new film thickness being calculated using Equation (3.2).

$$\delta_{(i,j),new} = \frac{1}{2}(\delta_i + \delta_j) \tag{3.2}$$

3.2.2 Geometrical Spreading

Geometrical spreading assumes a limited mobility of liquid during particle-particle collisions, based on the spherical cap approximation described in Section 2.3.1 and shown in Figure 2.2 [16]. For monosized spherical particles i and j, the contribution of particle i ($V_{lb,i}$) and total liquid bridge volume ($V_{lb,tot}$) are given in Equations (3.3) and (3.4).

$$V_{lb,i} = \frac{\pi}{2}D^2\left[1 - \sqrt{\frac{3}{4}}\right]\delta_i \tag{3.3}$$

$$V_{lb,tot} = \frac{\pi}{2}D^2\left[1 - \sqrt{\frac{3}{4}}\right](\delta_i + \delta_j) \tag{3.4}$$

From Equations (3.3) and (3.4), a new film thickness post collision can be calculated (Equation (3.5)).

$$\begin{aligned}\delta_{(i,j),new} &= \delta_{(i,j)} - \frac{V_{lb,(i,j)}}{\pi D^2} + \frac{V_{lb,tot}}{2\pi D^2} \\ &= \delta_{(i,j)} + \frac{1}{4}\left[1 - \sqrt{\frac{3}{4}}\right]\left(\delta_{(j,i)} - \delta_{(i,j)}\right) \end{aligned} \tag{3.5}$$

3.2.3 Interaction-time Dependent Spreading

The interaction-time dependent spreading rule is more complicated than the previous models, taking into account the time in which the particle films have overlapped, along with the surface tension and liquid viscosity. The surface tension and liquid viscosity are important to study for the application of coking. This is because the injected liquid properties change rapidly under the high temperatures within the coker. By examining a range of liquid properties, discrete points in time during the reaction process are studied.

The details of this method were discussed in Section 2.3.2. The interaction time and bridge diameter are calculated based on Equations (2.29) and (2.28), respectively. From this, the liquid bridge volume is calculated based on Equation (2.35). Since the liquid bridge grows during rebound, the total volume is calculated based on $a = (\delta_i + \delta_j)$.

To ensure liquid conservation, the liquid bridge volume cannot exceed the sum of liquid on both particles. V_{lb} is taken as the minimum between the sum of liquid on both particles and the volume calculated by the growth model. As with the previous spreading rules, the bridge volume is then split evenly between particles. In this spreading rule, however, the liquid contribution from each particle has not yet been discussed. In this case, the contribution is determined using Equation (3.6).

$$V_{lb,i} = \frac{\delta_i}{\delta_i + \delta_j} V_{lb,tot} \tag{3.6}$$

For particles of equal diameter, the total volume of liquid on each particle is proportional to its liquid film thickness through the equation $V_{lb,i} = \pi D^2 \delta_i$. Therefore, for the case of an infinitely long collision (where all the liquid on both particles is transferred into the bridge), Equation (3.6) ensures the proper calculation of liquid from each particle, and therefore ensures liquid mass conservation. Additionally, in a wet-dry collision all the liquid is provided by the wet particle. In a collision of equally-wetted particles, the liquid is provided equally by both particles, resulting in no net transfer. With little insight into the physical rates of liquid transfer based on film thickness, Equation (3.6) provides a simple model that satisfies the boundary cases and ensures liquid mass conservation.

The new film thickness on each particle is therefore determined as in Equation (3.7).

$$\delta_{(i,j),new} = \delta_{(i,j)} - \frac{V_{lb,(i,j)}}{\pi D^2} + \frac{V_{lb,tot}}{2\pi D^2} \tag{3.7}$$

3.3 Analysis Methodology

The goal of this work is to determine whether the liquid spreading can be modeled as a diffusion process and to determine effective liquid diffusion coefficients based on fluidization characteristics, liquid properties, and direction. Because of the anisotropy between the horizontal and vertical directions (due to gravitational effects vertically), the diffusion coefficient is examined in both a horizontal and vertical direction separately.

Four different domain sizes are considered, as presented in Table 3.1.

Table 3.1: Domain sizes considered.

Domain	Nx/D	Ny/D	Nz/D
1	6.25	6.25	6.25
2	10.4	10.4	10.4
3	6.25	6.25	12.5
4	6.25	6.25	25

Because the particle velocities are higher in the z-direction, the expansion of the domain is examined in this direction. In order to examine the directions separately, the 3-dimensional diffusion is simplified into an effectively 1-dimensional diffusion by setting the initial condition as shown in Figure 3.3.

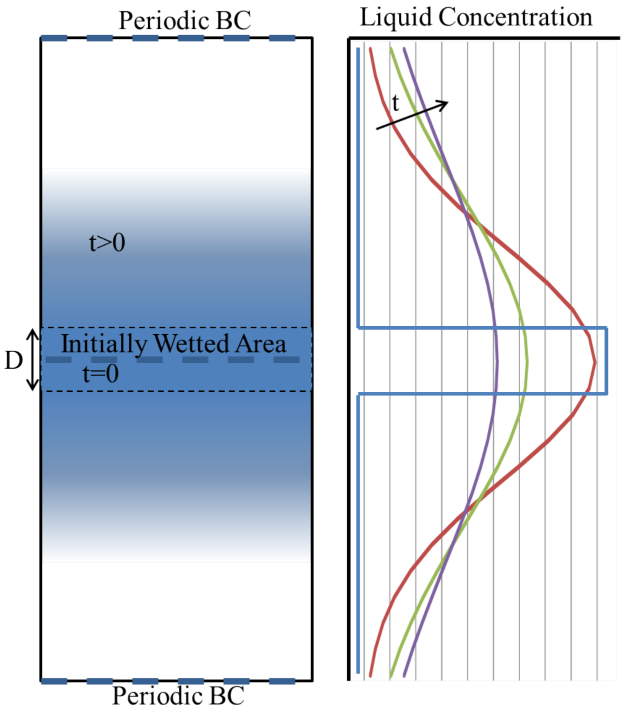

Figure 3.3: Schematic of initial condition for determining diffusion coefficient and idealized data curves expected.

Initially, particles within a plane of thickness D are coated with liquid, where any particle with a center within this slice is equally coated with a thickness $\delta/D =$

0.08. The dependence of the initial liquid film thickness on the rate of spreading is not considered in this chapter. This liquid is then allowed to spread through the fluidized bed. This process is shown in Figure 3.4.

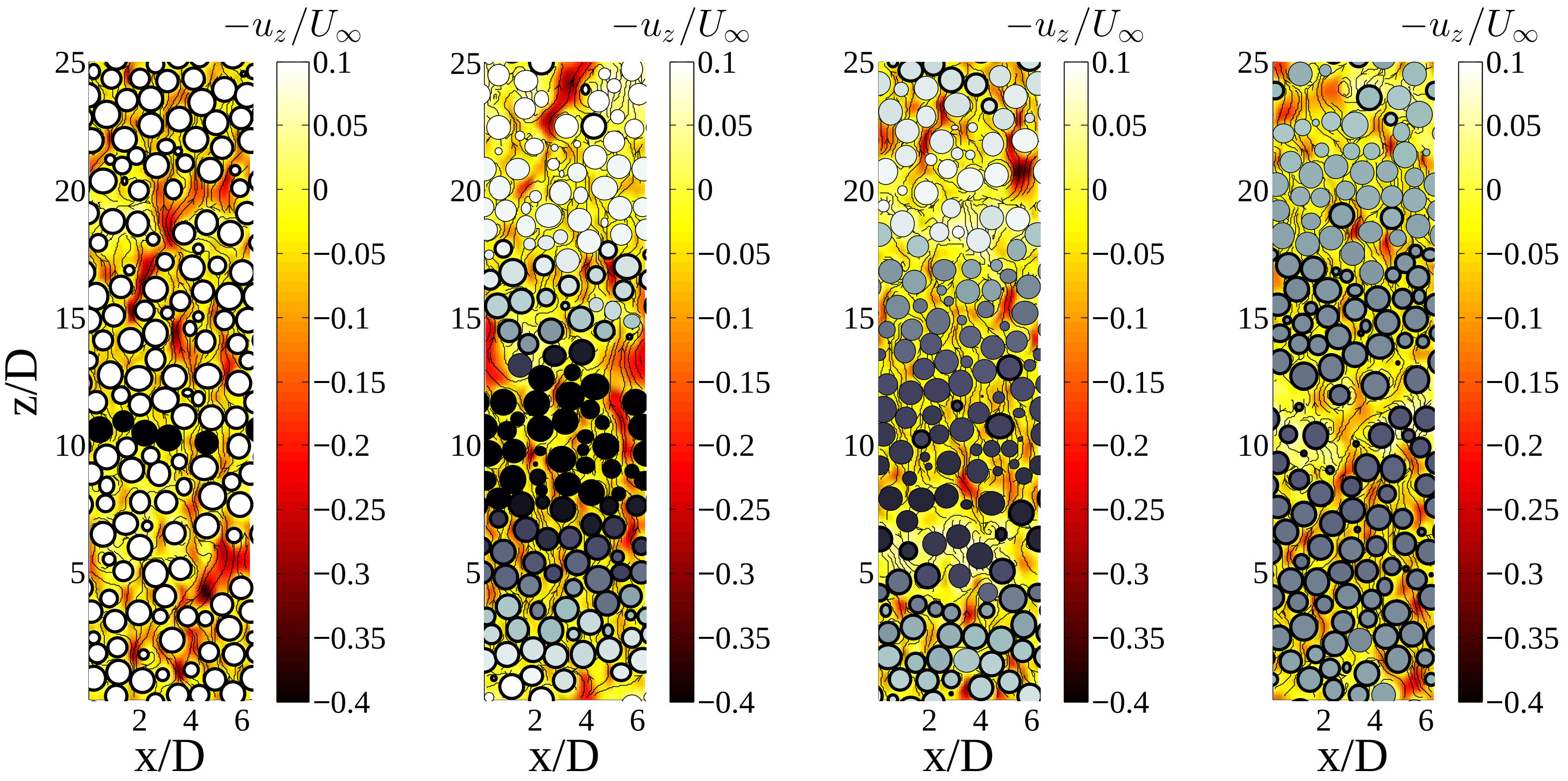

Figure 3.4: Visualizations of vertical liquid spreading. From left to right, $tU_\infty/D = 0$, 75, 145, 219. Liquid content on the particles scales from black to white, where white particles are dry. $\phi = 0.5$, domain size 4, interaction-time dependent spreading rule with $T_v = 0.40$ (lower limit selected to provide largest contrast over time).

By tracking the evolution of the liquid mass concentration $C(x,t)$ over time, and fitting a curve of the form in Equation (3.8) to the results, an effective liquid diffusion coefficient Γ is obtained.

$$C(x,t) = \frac{\frac{\rho_l V_{l,tot}}{A}}{\sqrt{4\pi\Gamma t}} exp\left(\frac{-x^2}{4\Gamma t}\right) \tag{3.8}$$

A is the cross-sectional area of the diffusion plane and x is the direction of diffusion (either horizontal or vertical).

In order to apply Equation (3.8) to the simulation results, it is modified into Equation (3.9). Details of the derivation and manipulation are discussed in Appendix B.

$$\frac{1}{\Delta p}\sum_{i=1}^{N_{plane}} \frac{h_i}{D}\delta_i = \frac{1}{\sqrt{4\pi\Gamma t}} exp\left(\frac{-(x-\beta)^2}{4\Gamma t}\right)\sum_{i=1}^{N_{tot}}\delta_i \tag{3.9}$$

where Δp is the thickness of the analysis slice, h_i is the thickness of the particle within the slice ($h_i = \Delta p$ if both sides of the analysis slice cut through the particle), and β is the deviation of the curve fit peak from the simulation domain center. N_{plane} refers to the number of particles in the analysis plane, and N_{tot} is the total number of particles in the system.

Equations (3.8) and (3.9) have a different initial condition than that of the simulation domain due to the finite thickness of the initially wetted plane within the simulations. These equations implement a Dirac delta initial condition, which is not feasible in the simulations. Because of this, error is expected at initial times in the results. Therefore, the diffusion coefficient only after some time can be deemed reliable. Additionally, at later times, the periodic boundary conditions begin to affect the results. The motion of liquid from one side of the domain into the other results in excess liquid re-entering the domain from the other side. This effect is examined by comparing various domain sizes (Section 3.4.1) and by tracking the liquid content at the boundaries.

The comparison between Equation (3.9) and the simulation results is done via a non-linear fit with the use of the MATLAB nlinfit function. Using this, the data is fit with regards to the peak β and the diffusion coefficient Γ. Additionally, the peak location β can be matched manually by examining the average particle velocity over time. Horizontally, the peak location should remain constant. Vertically, however, the peak position is expected to move downwards due to the average downward particle velocity. The figures shown in this section all refer to the vertical direction. This direction expresses more instability, and is therefore considered when examining the analysis methodology.

Figure 3.5 shows the data and relevant curve fit for five times. The fitting of the data shows good quality visually, and results in a residual error of less than 0.025 at all times. The error is the residual of the fit, defined in Equation (3.10).

$$E = \frac{\sum_i (X_i - \overline{X})^2}{Q - p} \tag{3.10}$$

The numerator is the sum of the residuals with X_i and $\overline{X}$ the left-hand side of Equation (3.9) and the fit value at that position, respectively. Q is the number of data points, which depends on the thickness of the analysis slice. p is the number of fitting parameters, which is equal to two for a fit peak (β and Γ) and one for a fixed peak (Γ).

At later times, non-uniformities in the profile appear away from the main peak. Physically, this is explained through rapid spreading of liquid over the particle surface (compared to motion of particles) when particles come into contact and exchange liquid. The numerical treatment accentuates this rapid liquid motion, with liquid spreading over the particle surface instantaneously at the time of collision. This leads to sudden increases in liquid over the analysis slice range covered by an interacting particle, and therefore the appearance of bulges. These bulges are more significant for spreading rules that spread liquid more effectively, with larger volumes being transferred per collision.

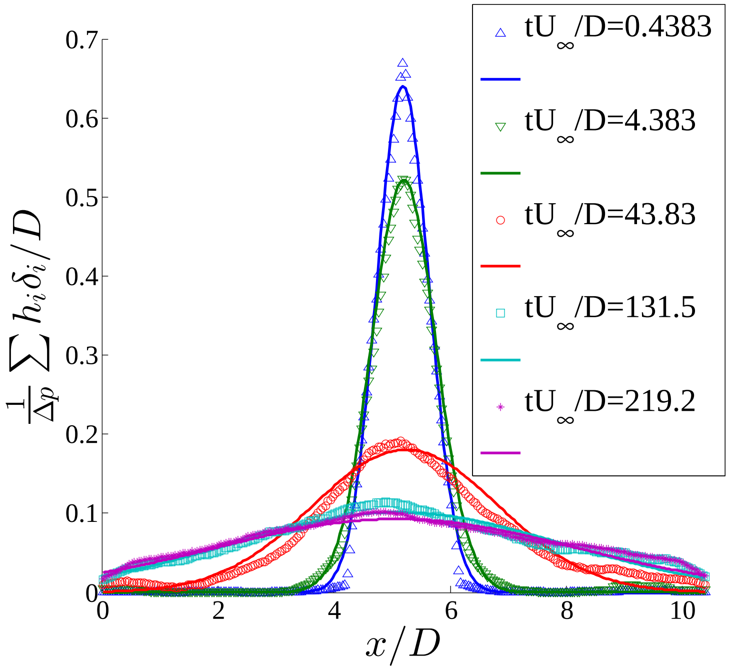

Figure 3.5: Fits of experimental data to Equation 3.9 for $\phi = 0.5$, domain size 2, based on 10 realizations, vertical direction, interaction-time dependent spreading rule with intermediate spreading rate $T_v = 4.18$ at various non-dimensionalized times tU_∞/D. Symbols represent data, lines represent MATLAB fit.

In order to qualitatively check the validity of treating the spreading as a diffusion process, Equation (3.9) can be normalized. This is done by dividing both sides of Equation (3.9) by the peak concentration (at $x = \beta$), as in Equation (3.11).

$$\frac{\sum_{i=1}^{N_{plane}} h_i\delta_i\Big|_x}{\sum_{i=1}^{N_{plane}} h_i\delta_i\Big|_\beta} = exp\left(\frac{-(x-\beta)^2}{4\Gamma t}\right) \tag{3.11}$$

By plotting the left hand side of Equation (3.11) against $(x-\beta)/\sqrt{4t}$, Γ is left as the only depending variable. Therefore, after an initial period, the curves are expected to overlap, as shown in Figure 3.6.

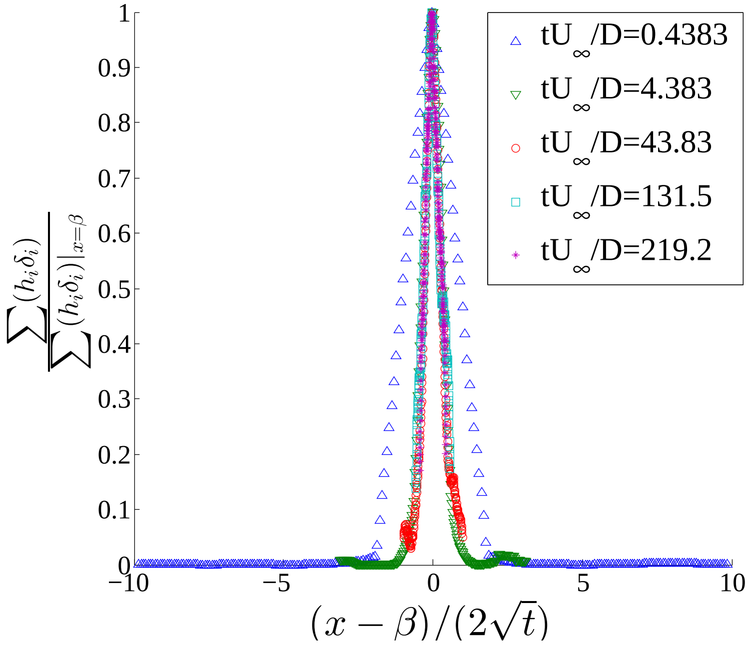

Figure 3.6: Fits of experimental data to Equation 3.11 for $\phi = 0.5$, domain 2, based on 10 realizations, vertical direction, interaction-time dependent spreading rule with $T_V = 4.18$ at various non-dimensionalized times tU_∞/D.

The analysis slice was taken as $\Delta p/D = 0.008$. Comparison of five slice thicknesses showed analysis thickness independence at this thickness, as shown in Figure 3.7. The lower solids volume fractions of ϕ =0.3 and 0.4 showed the largest deviation in vertical diffusion coefficient over time, and are therefore considered below.

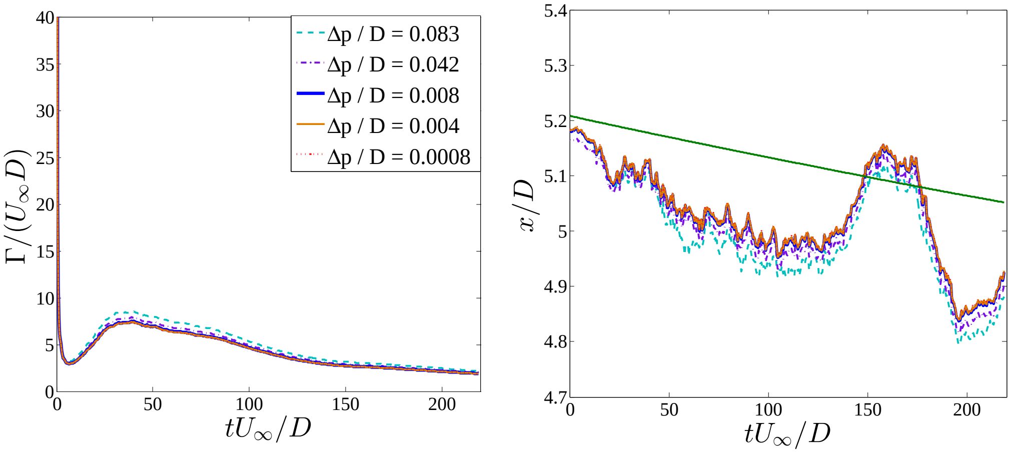

(a) Vertical diffusion coefficient over time.

(b) Position of peak over time.

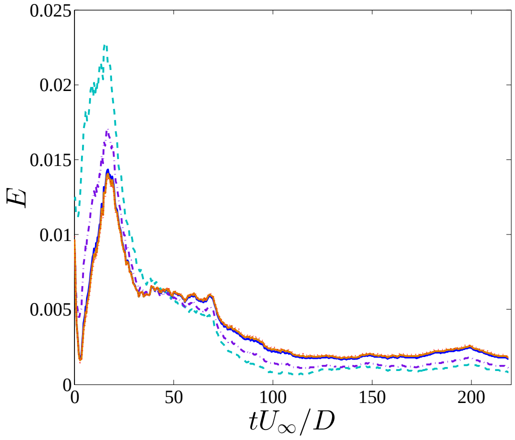

(c) Residual squared error over time.

Figure 3.7: Position of peak fit over time for various analysis thicknesses. The red (dotted), orange (solid), and blue (solid thick) lines overlap, showing independence on the slice thickness at $\Delta p/D = 0.008$. The line with constant slope downward in (b) represents the net downward particle motion. $\phi = 0.3$, domain size 2, vertical direction, interaction-time dependent spreading rule with $T_v = 11.9$.

Significant noise is expected in the results. This is due to the discrete nature of the spreading, specifically the fact that particle-particle collisions move liquid over the particle surface instantaneously. In order to minimize the noise in the results, analysis of multiple initially wetted planes is performed. The multiple resulting concentration profiles are super-imposed prior to curve fitting to determine Γ. Since for one-way coupling the liquid does not affect the fluidization, this is accomplished by applying multiple realizations to the same simulation. Changes of the resulting diffusion coefficient and associated error are examined as the number of realizations is increased, as shown in Figure 3.8. There are two data sets of 3 and 5 realizations in Figure 3.8 to show the discrepancies that occur based on which realizations are compared.

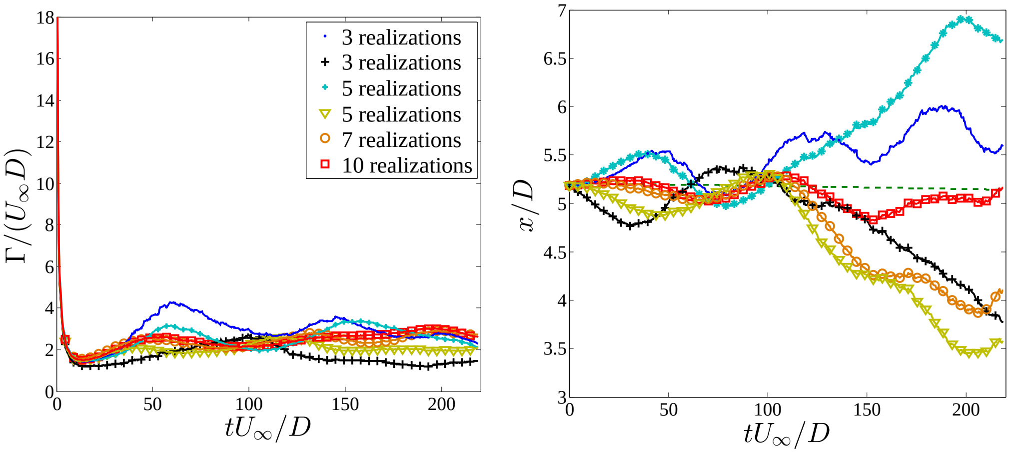

(a) Vertical diffusion coefficient over time.

(b) Position of peak over time.

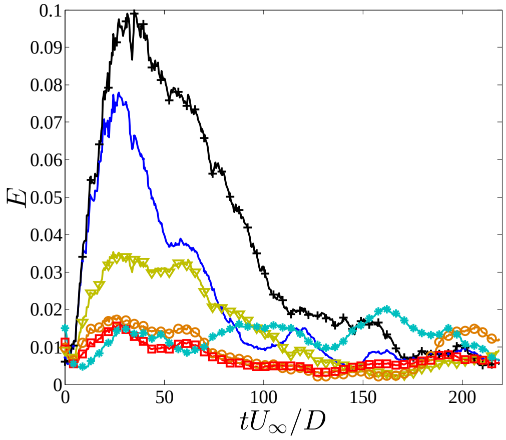

(c) Residual squared error over time.

Figure 3.8: Results averaged over different numbers of realizations. The dashed green line in (b) represents the net downward particle motion. $\phi = 0.4$, domain size 2, vertical direction, interaction-time dependent spreading rule with $T_v = 11.9$.

The number of realizations has a clear impact on the results of the fit. As expected, with only 3 or 5 realizations being considered, the data is scattered for both the error and peak fit, additionally showing more fluctuations in the diffusion coefficient than the higher number of realizations. As more realizations are included in the fit, the curves align more with one another, the error in the fit E is significantly reduced (by almost an order of magnitude between 3 and 10 realizations at $tU_\infty/D = 40$), and fluctuations in the effective vertical liquid diffusion coefficient are reduced. The peak position fits for 7 and 10 realizations vary by just over a particle diameter at their maximum, leading to a peak in the error for 7 realizations at $tU_\infty/D = 210$ compared to 10 realizations. In general, the uncertainties for 7 and 10 realizations are significantly reduced compared to the 3 and 5 realization results. Our simulation domain sizes allow for between 6 and 25 realizations, with a maximum of 10 realizations horizontally and 25 realizations vertically.

Finally, a choice must be made as to whether to use a fixed peak approach or fit peak approach. Using a fixed peak approach treats the variable β in Equation (3.9) as the mean downward particle motion, as shown for example as the dashed line in Figure 3.8b. A fit peak approach uses β as a result of the MATLAB fit. Comparison of a fixed and fit peak is shown in Figure 3.9.

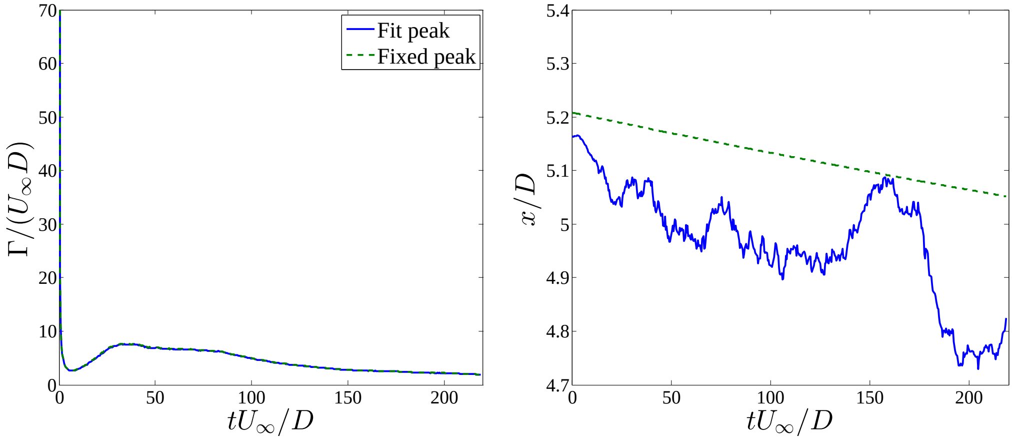

(a) Vertical diffusion coefficient over time.

(b) Position of peak over time.

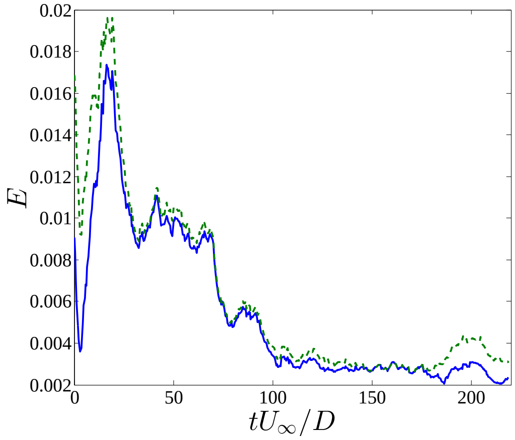

(c) Residual squared error over time.

Figure 3.9: Comparison of a fit peak (solid) and a fixed peak (dashed) for $\phi = 0.3$, domain size 2, vertical direction, interaction-time dependent spreading rule $T_v = 11.9$. When only one curve is visible, the two curves overlap.

From Figure 3.9b, there is a deviation between the location of the fit and fixed peak. While the figure looks drastic, the scale shows that over the entire simulation time, the peak varies by less than half a particle diameter. The difference in peak position results in an increase in fixed peak error (Figure 3.9c) compared to fit peak error. However, Figure 3.9a demonstrates that this variance does not have an effect on the overall diffusion coefficient, with the fit and fixed peak curves overlapping. The diffusion coefficient is determined based on the fixed peak results.

The diffusion rate is treated as a fitting parameter in the nonlinear fit. Therefore it is determined at each time, independent of the previous values. For a diffusion process, the diffusion coefficient is expected to be constant for all times. However, because of the deviation between the fit curve and simulation initial conditions, the initial diffusion coefficients are expected to be inaccurate. The diffusion curves show this transition, with the diffusion coefficient stabilizing over time from an initial peak. This is promising, as it shows that the liquid spreading can in fact be modeled as a diffusion process.

The diffusion coefficient is averaged after the initial peak and before the boundary conditions are said to influence the result. To prevent the influence of the boundaries, the volumes of liquid within the analysis slices farthest from the initial peak are examined and summed. The 3 % of the domain length farthest from the fit peak is considered as being within the boundary region for each of the respective domain lengths (selected as 2 lattice nodes for the smallest domain, with the ratio of boundary to domain maintained for other domains). The boundary is said to have an effect once the volume within the considered region reaches 5% of the total liquid volume. This boundary condition is reached for the equal spreading rule in the majority of cases both vertically and horizontally (with the exception of domain 4 in the vertical direction). Additionally, quicker rates of spreading for the interaction-time dependent spreading rule reach this boundary in the vertical direction (for smaller domains). With liquid spreading more quickly vertically than horizontally, this boundary is generally not reached in the horizontal direction for either the interaction-time dependent spreading or the geometrical spreading. The cases examined using the equal spreading rule could not be averaged for the majority of domains, with the system not stabilizing prior to the liquid concentration reaching the limiting concentration on the boundaries. These values were averaged for the times obtained for the fastest interaction-time dependent spreading for comparison purposes. However, without direct knowledge of the impact of the boundaries on the result, these results are uncertain.

The majority of diffusion trends drop from an initial peak to a steady state, with some showing an additional rebound after the initial drop and prior to stabilization. This rebound is concurrent with a spike in the fit error (example is present in Figure 3.9c for tU_∞/D up to between 100 and 120). If the rebound occurs, the diffusion curve is averaged after the rebound stage, through examination of the diffusion coefficient and associated error graphs. For example, Figure 3.9 is averaged starting at $tU_\infty/D = 120$. This time is chosen since the error of the fit (Figure 3.9c) has levelled off at this time, resulting in a more accurate fit for the vertical diffusion coefficient. This particular case does not reach the boundary condition within the simulation time, and is averaged to the simulation end. While minor changes in the diffusion coefficient still occur within the averaging time, these differences are within a magnitude of $\Gamma/U_\infty D < 2$ in the vertical direction, accounting for less than a 1% difference from the initial value in this case (the initial value is out of the frame of Figure 3.9a in order to focus on the diffusion coefficient at later times).

The varying spreading rules and liquid properties reach a steady state at different times, resulting in required interpretation for the start time for averaging. The stabilization time required for the diffusion coefficient increases as the liquid transferred per collision increases, since the error associated due to random particle motion is amplified by the larger liquid transfer volumes, and therefore the spreading model used. The equivalent spreading rule takes the longest to stabilize, followed by the interaction-time spreading rule from low to high values to T_v, as shown in

Figure 3.10. The geometric spreading rule results in intermediate spreading, with the diffusion coefficient stabilizing effectively.

The domain size has an effect on how quickly the diffusion coefficient stabilizes. For smaller domains, the boundaries may interfere before the diffusion coefficients stabilize. Conversely, larger domains take longer for diffusion coefficient stabilization due to the presence of larger scale phenomena, with some cases not having stabilized by the end of the simulation time (Figure 3.10b). The effect of the domain is discussed in detail in Section 3.4.1.

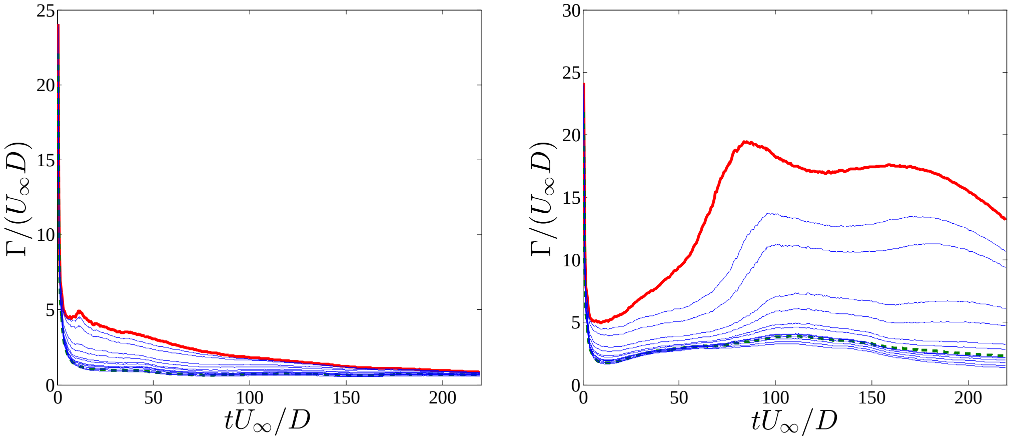

(a) Domain 1.

(b) Domain 4.

Figure 3.10: Vertical diffusion coefficient trends over time for different domains with $\phi = 0.4$. This solids volume fraction showed the largest fluctuations in vertical diffusion coefficient over time. The thick solid red line represents the equivalent spreading rule, the thick green dashed line represents the geometrical spreading rule (when not visible this curve is present among the dense lines), and the remaining blue curves represent the interaction-time dependent spreading rule with 12 values of T_v ranging from 0.4 to 11.9. Diffusion coefficients increase with decreasing values of T_v.

Since many of the curves clearly do not reach a stable diffusion curve within the simulation time, those cases are not considered throughout the remainder of the analysis. Only the vertical direction diffusion curves show this delayed transience

(Figure 3.10). The horizontal diffusion trends are not shown because they stabilize quickly. This is expected as the particle momentum is significantly greater vertically than horizontally, resulting in more instability due to individual particle behavior.

3.4 Results and Discussion

Based on the procedure described above, the non-dimensionalized effective liquid diffusion coefficients for a range of parameters are determined. The resulting diffusion coefficients are examined as they relate to a variety of properties. First, the effect of the domain size on the results is exained in order to determine whether the results are dependent on the domain size. Following this, the three spreading rules are compared, examining a range of liquid properties (depicted through the non-dimensional parameter T_v) for the interaction-time dependent spreading rule. Finally, the effect of the solids volume fraction ϕ is examined. Both the horizontal and vertical directions are analyzed.

The main fluidization characteristics that effect the diffusion rate are as follows:

(1) Particle-particle collision frequency

(2) Variance in particle velocity and granular temperature

(3) Mean particle velocity

(4) Large-scale instabilities in the fluidized bed

Comparison of these fluidization characteristics allows for a better understanding of how the system parameters effect the outcome. A good way to gauge the velocity fluctuations in the fluidized bed is through the granular temperature T, defined as follows [74].

$$T = \frac{1}{3}(\overline{\mathbf{v}^2} - \overline{\mathbf{v}}^2) \tag{3.12}$$

However, since the analysis is divided into horizontal and vertical directions, the variance is also split into horizontal and vertical elements. For the vertical direction, the variance is described in Equation (3.13).

$$var(v_z) = \overline{v_z^2} - \overline{v_z}^2 \tag{3.13}$$

In the horizontal direction, the mean particle velocities ($\overline{v_x}$ and $\overline{v_y}$) are approximately zero. The variance is averaged over the x and y directions.

$$var(v_{(x,y)}) = \frac{1}{2}(\overline{v_x^2} + \overline{v_y^2}) \tag{3.14}$$

Both of these values are normalized based on the terminal settling velocity U_∞.

3.4.1 Domain Size Effects

Horizontal Direction

First, the effect of the domain in determining the horizontal diffusion coefficients is examined, as shown in Figure 3.11.

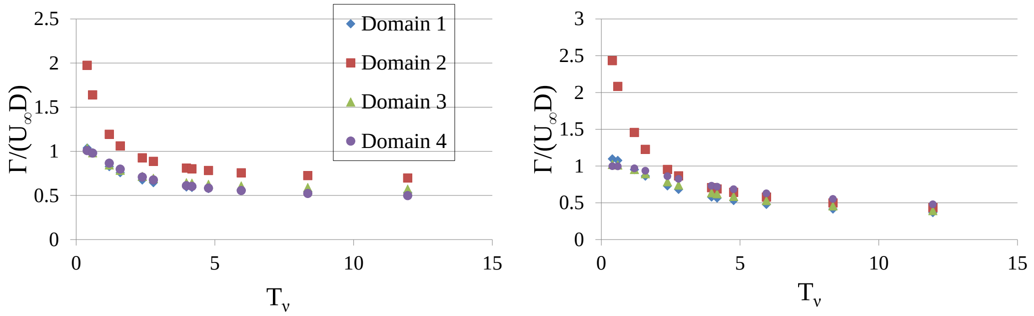

(a) $\phi = 0.3$. (b) $\phi = 0.4$.

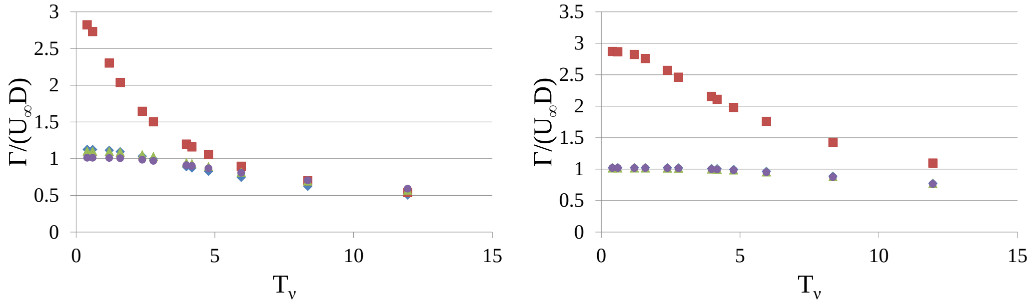

(c) $\phi = 0.5$. (d) $\phi = 0.55$.

Figure 3.11: Horizontal diffusion coefficient as a function of T_V for different domains. Only interaction-time dependent spreading shown.

The domains with horizontal length of 6.25D (domains 1,3, and 4) show excellent consistency in the diffusion coefficient for all values of T_V and all solids volume fractions ϕ. This shows that the horizontal diffusion coefficients are independent of the vertical length, as expected. However, the lengthening of the domain in the horizontal direction results in an increase in the resulting diffusion coefficients, as seen when comparing domain 2 with the other domains. The discrepancies in diffusion coefficient are especially noticeable for lower values of T_V. The higher values of T_V overlap for $\phi = 0.4$ and $\phi = 0.5$ and show a reduced difference for $\phi = 0.3$ and $\phi = 0.55$.

Since the differences in diffusion coefficients are most prominent at low T_V values, the fluidization properties that affect this range of data are examined. For high

T_v values, the interaction time between liquid films is an important factor in the amount of spreading. Due to the slow growth of liquid bridges, the interaction time effect dominates over the collision frequency and particle motion. However, for lower T_v values, this dependency becomes less important as bridges reach their maximum size more quickly. Therefore, for lower T_v values, the frequency of particle collisions and the motion of particles through the bed become the dominant effect. These fluidization characteristics are examined in Figure 3.12 to see if differences are present between the domains.

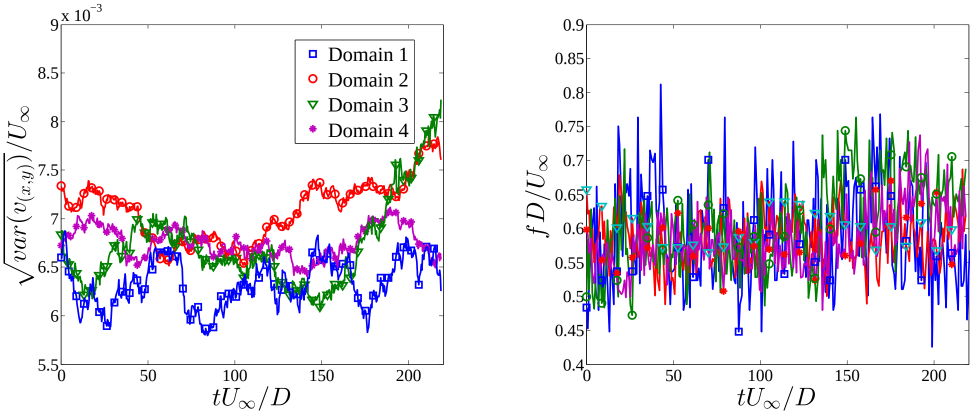

(a) Average horizontal particle velocity magnitude over time.

(b) Collision frequencies over time, averaged every $tU_\infty/D = 0.88$.

Figure 3.12: Comparison of fluidization characteristics affecting horizontal diffusion at low T_v values for $\phi = 0.55$.

From Figure 3.12b, the fluctuations in collision frequency are greater for smaller domains and the average collision frequencies are the same for all domains. The average horizontal particle velocity magnitudes also do not show a large discrepancy between domains. Figure 3.12a shows some deviation at later times. However, these velocity differences are in the order of 10^{-3} of the single particle settling velocity, and over an order of magnitude less than the corresponding vertical values. Conclusions regarding domain selection are presented after the vertical direction is discussed.

Vertical Direction

The effect of the domain on the vertical diffusion coefficients is shown in Figure 3.13. The vertical direction is expected to experience higher diffusion coefficients due to the presence of external forcing in this direction.

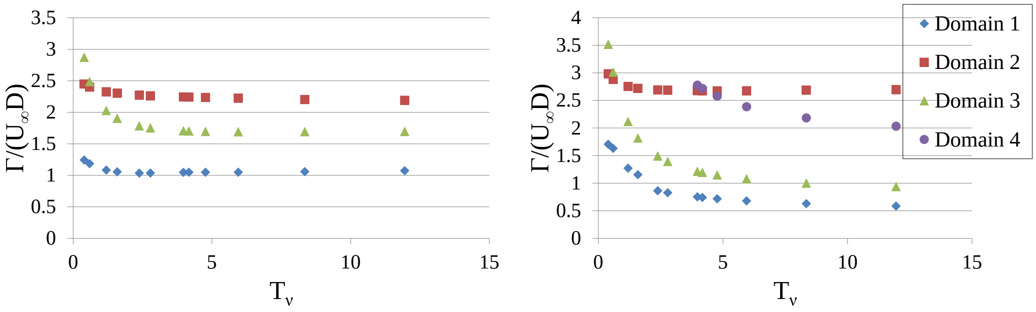

(a) $\phi = 0.3$. (b) $\phi = 0.4$.

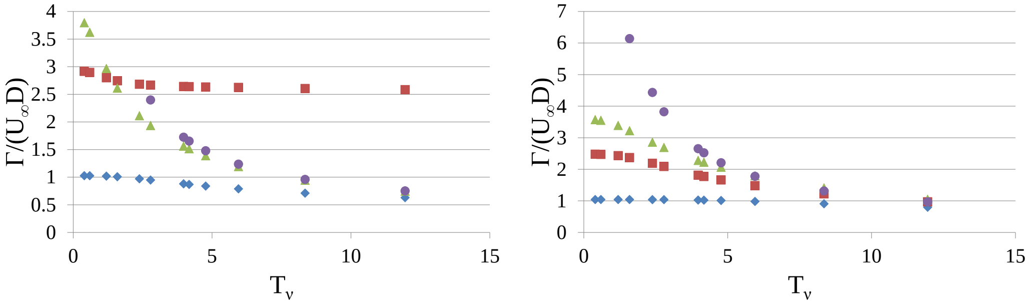

(c) $\phi = 0.5$. (d) $\phi = 0.55$.

Figure 3.13: Vertical diffusion coefficient as a function of T_v for different domains. Data that did not reach a steady state in the diffusion coefficient is not included.

From Figure 3.13, it is observed that for lower solids volume fractions (Figures 3.13a, 3.13b) the varying domains show different diffusion coefficients for the entire range of T_v values. Conversely, Figures 3.13c and 3.13d show a domain dependence at lower T_v values (with the exception of $\phi = 0.5$, domain 2).

Domains 1 and 2 additionally show less of a dependence on the value of T_v than domains 3 and 4. This is especially noticeable in Figure 3.13c, where domains 1 and 2 are largely independent of T_V.

In order to compare the domains, the differences present in terms of the mean vertical particle velocity, granular temperature, and instabilities are examined. The collision frequency has already shown no deviation between domains at $\phi = 0.55$ (Figure 3.12b). Instabilities are examined through space-time plots of the particle concentration [56]. The domain is split into cross-sections (thickness $\Delta p/D = 0.04$), and the local solids volume fraction ϕ within that slice is computed. This is done for the entire simulation time.

The presence of wave instabilities results in variances in solids volume fraction based on location. Therefore, different heights within the simulation experience different collision frequencies and particle velocities, and therefore different rates of liquid spreading and dominant mechanisms for liquid transfer. With sections of the bed reaching local solids volume fractions in the range of 0.1, the collision frequencies in these ranges will be low and the effect of particle velocities to spread liquid will dominate. In the dense regions, the particle collisions are the dominant method of liquid spreading. The effect of solids volume fraction is analyzed in section 3.4.3. With multiple realizations of each system being used in the determination of the diffusion coefficient, the initially wetted planes cover area of both high and low local solids volume fraction. However, because of the complex nature of the mechanisms for liquid spreading, this averaging of realizations will not result in the same diffusion coefficient as that of a system without wave instabilities.

These wave patterns have been previously studied in simulations of both liquid and gas-fluidized beds [25; 75–78]. Glasser et al. [76] showed that two-dimensional travelling waves (bubbles in the case of high amplitudes) are formed due to the presence of these one-dimensional travelling waves. The space-time plots for $\phi =$

0.4 are presented in Figure 3.14 for each of the domains.

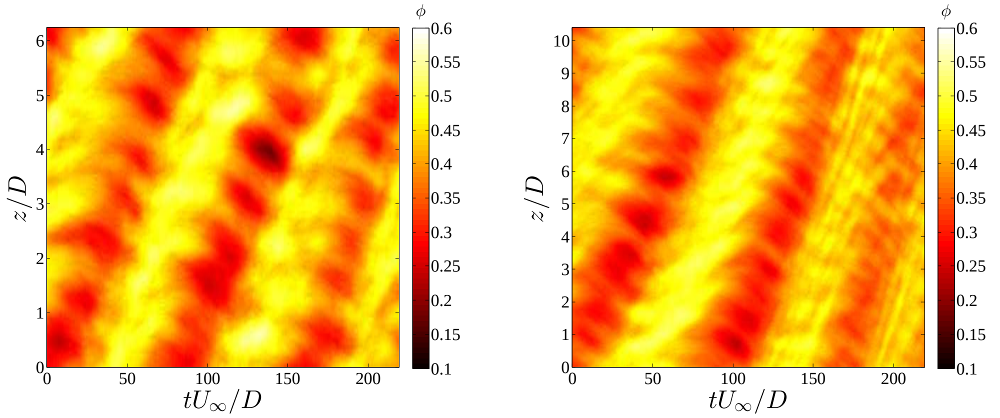

(a) Domain 1. Slope ≈ 0.080.

(b) Domain 2. Slope ≈ 0.116.

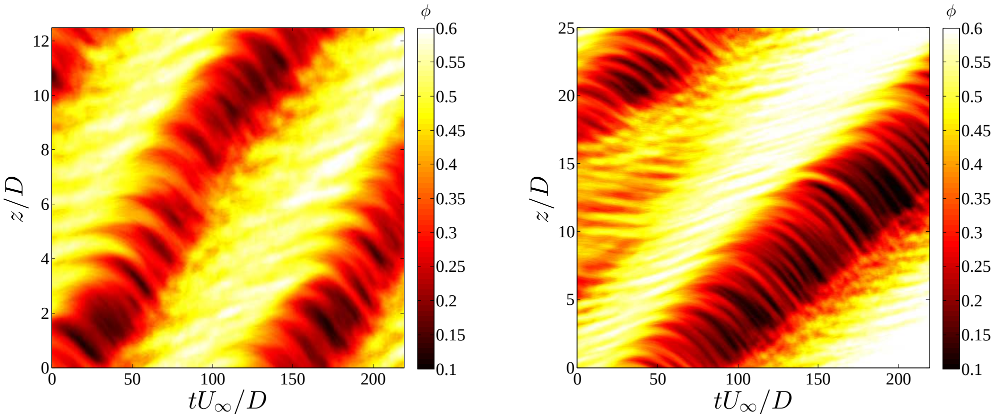

(c) Domain 3. Slope ≈ 0.093.

(d) Domain 4. Slope ≈ 0.110.

Figure 3.14: Space-time plots of local solids volume fraction ϕ through cross-sections of the domain. Average solids volume fraction $\phi = 0.4$.

Each plot in Figure 3.14 is scaled to the same size for visual consistancy, resulting in differences in the appearance of the wave slopes (given in the subheadings of Figure 3.14. The slope for domain 1 shows a deviation from the other slopes, with a 36 % difference compared to domain 2. The other three domains differ in slope by at most 0.023, or 22 %. These slopes are obtained by visually examining Figure 3.14, with three slope values being averaged per domain size. Larger vertical lengths allow for the formation of larger-amplitude instabilities, which are otherwise inhibited by the periodicity of the domain. Additionally, shorter horizontal lengths inhibit bubble formation [79]. This leads to the development of slugs rather than two and three-dimensional instabilities. While the boundaries of the simulations here are fully-periodic, the inhibitory effect will still be present if the bubble formation exceeds the scale of the simulation domain. Due to the similar heights of domains 2 and 3, the visible discrepancy in the amplitudes of the travelling waves is likely due to domain 3 being shorter horizontally and the resulting inhinibition of multi-dimensional instabilities.

The mean vertical particle velocities and vertical velocity variance are presented in Figure 3.15 as a function of time, for $\phi = 0.4$. From Figure 3.13b, the deviation in diffusion coefficient is significant between domains for the entire range of T_v values. Therefore, this solids volume fraction is examined, looking at mean particle velocity and vertical velocity fluctuations.

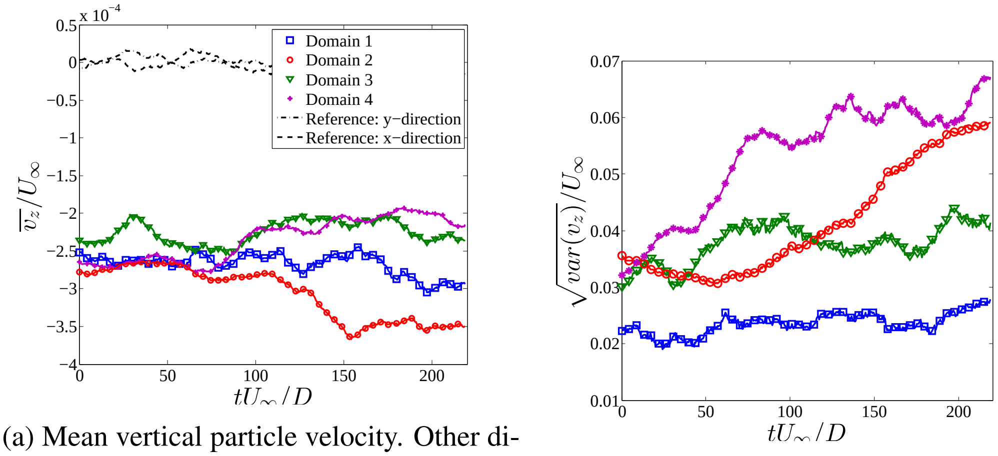

(a) Mean vertical particle velocity. Other directions shown for domain 1 to provide context.

(b) Vertical velocity fluctuations.

Figure 3.15: Comparison of fluidization characteristics for varying domain sizes at $\phi = 0.4$.

Figure 3.15a is generally steady, with a slight deviations of order 10^{-4} for domain 2 and domain 4 at later times. The average velocities remain similar for all domains. Figure 3.15b shows that the vertical velocity fluctuations for domains 2 and 4 are unsteady. Examination of the collision frequency for domain 4 at $\phi = 0.4$ shows that, despite being initialized from a dynamically steady domain 1 and allowed to run for $tU_\infty/D = 220$, the collision frequency is not steady. However, the collision frequency for domain 2 is steady, as shown in Figure 3.16.

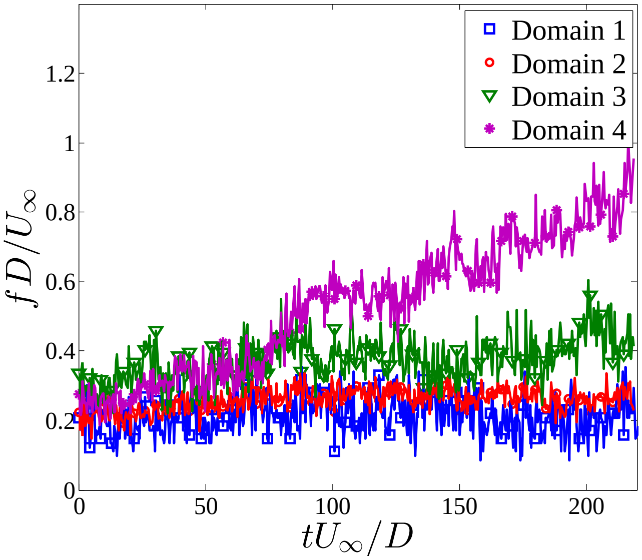

Figure 3.16: Collision frequency at $\phi = 0.4$, for different domain sizes.

Domain Choice

Having examined the vertical trends relating the domain size to the resulting diffusion coefficients, the results for domain 4 are inaccurate due to the unsteady behavior observed with regards to the collision frequency. Considering the remainder of the domains, the differences in resulting diffusion coefficient point to a lack of domain size independence, with variations in collision frequency, formation of instabilities, and particle velocities between domains.

Larger domains are necessary to ensure domain size independence. Due to time and computational restrictions, larger systems are currently impractical. The remaining analysis will be performed using domain 3. While domain 4 would be the optimal choice due to its large height, it did not reach a steady state for all solids volume fractions. Domain 3 provides the largest height of the three simulation domains considered (that reached a steady state), and shows qualitative agreement in the space-time plots with domain 4.

3.4.2 Comparison of Liquid Spreading Rules

A comparison of the liquid spreading rules is shown in Figure 3.17. For clarity, only the lowest and highest values of T_v are shown. The minimum and maximum values used in the averaging of these cases are additionally presented in the form of error bars. The error bars are greatest for equal spreading, and decrease for increasing values of T_v for interaction-time dependent spreading. The quicker spreading models are more susceptible to fluctuations, and take longer to equilibrate.

The equal spreading model results in the largest rate of liquid spreading, for all fluidized bed properties. This is expected since equal spreading transfers the maximum amount of liquid every collision. The geometrical spreading model shows a similar trend, but with significantly slower diffusion. This is also expected, since the difference between these models is simply a factor of $2/(1-\sqrt{3/4})$ in the liquid bridge volume. This factor does not directly relate to the diffusion coefficient due to the additional steps and effects that control the rate of liquid spreading. For the equal and geometrical spreading rules, the relevant properties affecting liquid spreading are the motion of particles and the collision frequency. The interaction-time dependent spreading rule additionally depends on the liquid properties and the relative velocity of colliding particles.

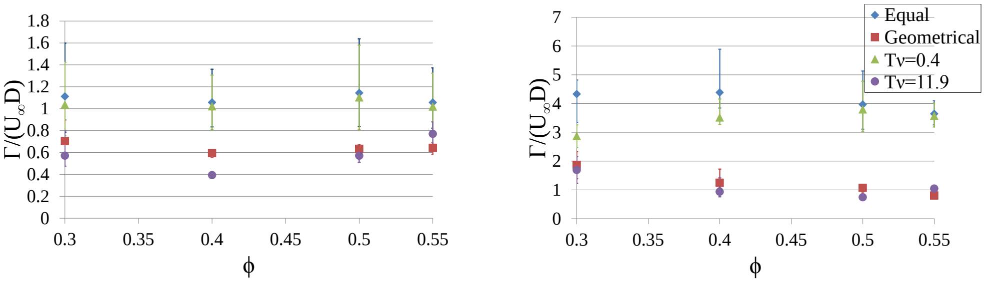

(a) Horizontal direction.

(b) Vertical direction.

Figure 3.17: Diffusion coefficient for varying solids volume fractions; comparison of equal spreading, geometrical spreading, and lower and upper bounds of the interacton-time dependent spreading rules. Error bars show minimum and maximum values from averaging in time.

From Figure 3.17a, it is observed that the differences between the equal spreading diffusion rates horizontally based on ϕ are minimal, and well within the averaging bounds. For the geometrical spreading, there is a decrease of 0.1 in diffusion at $\phi = 0.4$. This shows that in general, the horizontal diffusion coefficient is independent of the solids volume fraction. The competing effects of collision frequency and velocity fluctuations are therefore comparable in the horizontal direction, since the dominance of one would result in a clear trend towards more aggregation in either low of high solids volume fraction. If liquid spreading were to be dominantly through particle collisions the diffusion would be quicker for denser systems, whereas if liquid spreading were to be primarily through particle motion the lower solids volume fractions would result in larger diffusion coefficients. In the vertical direction (Figure 3.17b), a different trend is visible. Here, the increase in solids volume fraction leads to a decrease in diffusion coefficient. Since the vertical velocity fluctuations are expected to be larger than those horizontally, this trend is additionally expected.

Figure 3.18 examines the steady state collision frequency compared to the velocity fluctuations horizontally and vertically. The square root of the granular temperature is also presented in Figure 3.18 (triangles). The mean vertical particle velocity is two orders of magnitude smaller than the deviations observed for all solids volume fractions, and is therefore deemed negligible for liquid spreading compared to collisions and variance in particle motion.

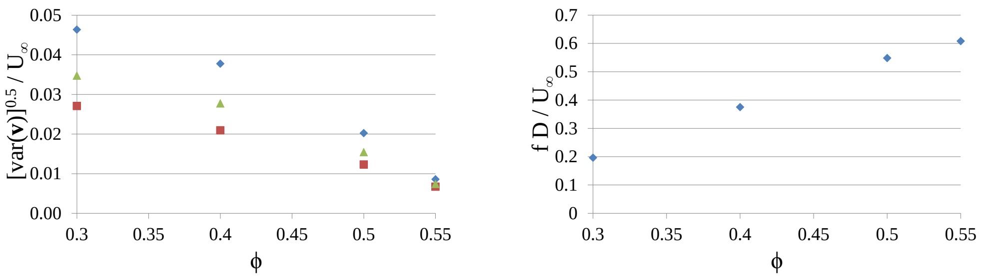

(a) Average particle velocity fluctuations.

(b) Collision frequency.

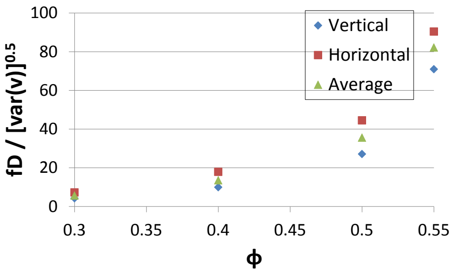

(c) Comparison of collision frequency and mean particle velocity fluctuations.

Figure 3.18: Comparison of fluidization characteristics affecting liquid diffusion, independent of liquid properties.

As expected, larger particle velocity fluctuations are observed for lower solids volume fractions, with the vertical direction increasing by a factor of 5.4 and the horizontal direction increasing by a factor of 4.0. The collision frequency trend is approximately linear, while the changes in velocity fluctuation become more significant in the higher ranges of solids volume fraction. Figure 3.18c compares the collision frequency to the standard deviation in the velocity fluctuations. This shows a non-linear trend in the ratio of these two effects.

The three liquid spreading rules result in discrepancies in the resulting diffusion coefficient. Differences are small for the horizontal direction, with a maximum difference in non-dimensionalized diffusion coefficient for $\phi = 0.4$ of 0.7. Vertically, this maximum difference in non-dimensional diffusion coefficient was larger at 3.4 (also for $\phi = 0.4$). For the majority of solids volume fractions both vertically and horizontally, the geometrical spreading results in a diffusion coefficient higher but comparable to the interaction-time dependent spreading at $T_v = 11.9$. Similarly, the averaging differences associated with the top range of the interaction-time dependent spreading ($T_v = 0.4$) puts the equal spreading rule within the range of the interaction-time dependent spreading (except for the vertical case at $\phi = 0.3$). While the equal and geometrical spreading rules result in differences in diffusion coefficient, they are generally both encompassed by the range of results obtained through the interaction-time dependent spreading rule.

The horizontal diffusion coefficients showed little to no dependence on solids volume fraction. Vertically, however, the geometrical spreading, equal spreading, and interaction-time dependent spreading at $T_v = 11.9$ resulted in decreases of approximately one in the non-dimensional diffusion coefficients over the range of solids volume fractions. The smaller solids volume fractions resulted in quicker liquid spreading.

The interaction-time dependent spreading at $T_v = 0.4$ shows a different trend than the other rules for vertical spreading, with an increase in the diffusion coefficient from $\phi = 0.3$ to $\phi = 0.55$. The interaction-time dependent spreading has the additional component of relative particle collision velocity in determining the liquid transferred per collision. This effect is discussed in the next section, which focusses on the interaction-time dependent spreading rule. This rule allows for the comparison of liquid properties, making it the most applicable for industrial processes.

3.4.3 Effects of T_v

The dimensionless parameter T_v controls the spreading of liquid between any two particles during a collision. To understand the overall spreading of liquid, comparison of this dimensionless parameter is essential. The diffusion coefficients for the interaction-time dependent spreading models range from $T_v = 0.4 - 11.9$. The top limit of T_v results in the slowest spreading of all the models. This is expected, since T_v is based on the ratio of liquid viscosity to surface tension, with a higher T_v value relating to a higher liquid viscosity or lower surface tension. The viscosity limits liquid motion into the bridge, while the surface tension promotes it. Figure 3.19 shows that, as expected, higher T_v values result in lower diffusion coefficients. However, the trend of diffusion coefficient vs. T_v value is non-linear, and differs for different solids volume fractions.

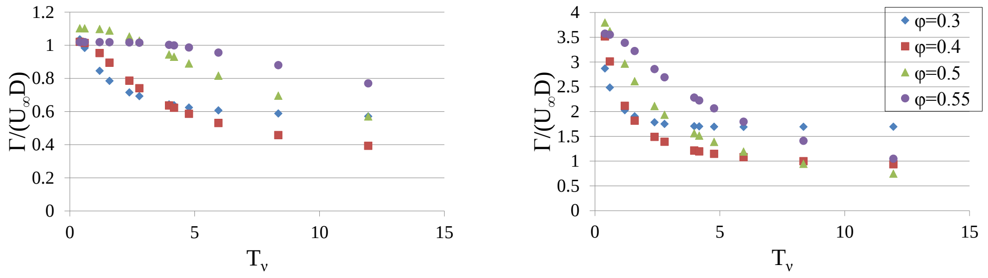

(a) Horizontal direction.

(b) Vertical direction.

Figure 3.19: Diffusion coefficient for interaction-time dependent spreading as a function of T_v at varying solids volume fractions.

An independence of liquid diffusion on T_v is observed at both extremes of the T_v values for certain solids volume fractions. In Figure 3.19a, the lower values of T_v at $\phi = 0.5$ and 0.55 level off. At these properties, the rate of bridge growth is high, the particle velocities are low, and the interaction time for bridge growth is high. These properties allow for the bridge to grow to its maximum volume, resulting in near-equal spreading (as shown in Figure 3.17a).

Additionally, the diffusion becomes independent of T_v for high values of T_v at low solids volume fractions, as shown in Figure 3.19b for $\phi = 0.3$. These conditions are as follows: particle velocity fluctuations are high (Figure 3.18a), collision frequencies are low (Figure 3.18b), and interaction times are short due to large relative collision velocities (Figure 3.20a). These properties result in fewer collisions and less liquid being spread per collision. However, the diffusion rates are larger for this solids volume fraction than for others. The particle motion itself therefore results in the efficient spreading of the liquid. This conclusion can also be drawn for the horizontal diffusion (Figure 3.19a), but not to the same extreme, since the horizontal fluctuations are smaller than those vertically.

The relative collision velocities between particles are presented below in Figure 3.20. The relative collision velocity distributions are averaged over a time $tU_\infty/D = 44$.

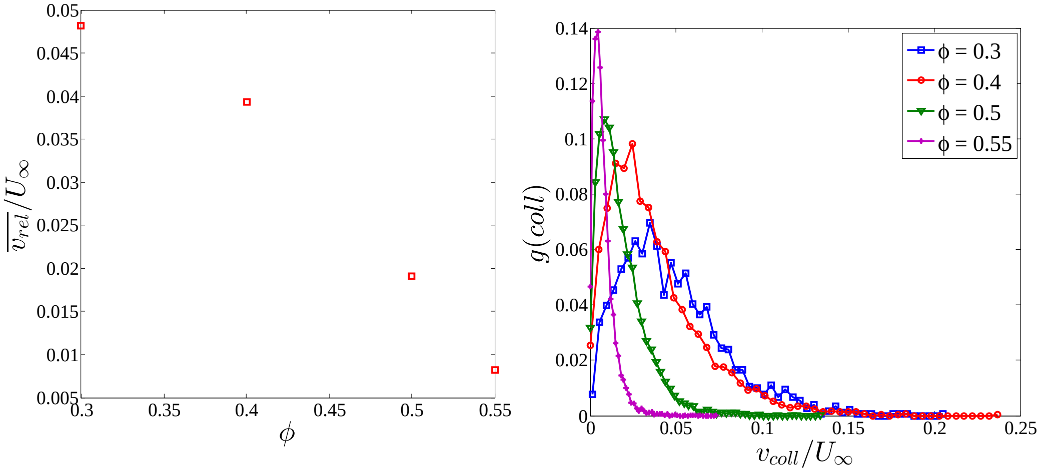

(a) Average relative velocity of colliding particles.

(b) Relative collision velocity distribution.

Figure 3.20: Comparison of relative particle collision velocities for varying solids volume fractions.

Figure 3.20 shows that, as expected, higher solids volume fractions have slower relative velocities of particles upon collision. This trend relates directly to Figure 3.17b, $T_v = 0.4$, where the diffusion coefficient follows that of the equal spreading rule for $\phi = 0.55$ and 0.5, but is significantly decreased for $\phi = 0.4$ and 0.3.

By examining the dominant effects influencing liquid spreading for high and low T_v values, conclusions can be made as to the dominant factors effecting the diffusion. Specifically, high solids volume fraction systems spread liquid predominantly through particle collisions, whereas lower solids volume fraction systems spread liquid through particle motion.

3.5 Conclusions

The effect of three liquid spreading models on the rate of liquid spreading within a fluidized bed in the horizontal and vertical directions was studied. For the third liquid spreading model, the effect of liquid properties was examined, specifically surface tension and viscosity, on the spreading. A dimensionless parameter T_v was introduced to combine the effects of liquid properties, and ranged from $T_v = 0.4 - 11.9$. The bed was examined at four different solids volume fractions, ranging from $\phi = 0.3$ to $\phi = 0.55$.

Four domain sizes were compared in order to determine whether results were domain-size independent. Unfortunately, the domain was found to have an effect on the resulting liquid diffusion. The introduction of larger domains was impractical, and therefore the domain with the largest vertical height that had reached a steady state was chosen. The vertical direction is of particular interest due to the external gravitational force in this direction, resulting in larger fluctuations in particle velocities. The presence of large-scale instabilities was visible in these simulations, and showed qualitative agreement with instabilities shown in a longer system. The presence of these instabilities is limited in smaller domains due to the periodicity of the boundaries, with their presence being more representative of larger-scale systems as a precursor to bubble development. These instabilities result in areas of high and low solids volume fraction compared to the volume-averaged solids volume fraction, leading to differences in dominant liquid spreading mechanisms in different sections of the bed.

The assumption was made that the process could be modeled as diffusive. By comparing the simulation liquid concentrations over time and a similar case analytical solution for diffusion, the resulting effective liquid diffusion coefficient was averaged over the simulation time. This diffusion coefficient was based on the combined effect of liquid spreading due to particle-particle collisions and that of the motion of wetted particles through the simulation domain. The mean downward particle velocity was approximately two orders of magnitude smaller than the relative particle velocity fluctuations, and was not considered a significant factor in liquid spreading.

The horizontal diffusion coefficients were found to be smaller, but of similar order as those vertically. Of the three spreading rules considered, the equal spreading rule resulted in the fastest diffusion. The geometrical spreading rule showed significantly slower diffusion, with the interaction-time dependent spreading rule encompassing the range between the other two models. Because this model allows for variation of liquid properties, it was the most useful for examining a system representative of fluid coking.

The examination of liquid properties on effective diffusion coefficients determined that, for varying solids volume fractions, the dominant methods of liquid spreading varied. Focusing on low liquid viscosity at early times within the lifespan of the liquid, horizontal spreading rates were shown to be approximately independent of the bed height (represented by the solids volume fraction). With the increase in liquid viscosity over time a decrease in liquid spreading was observed, with sections of lower solids volume fraction showing a decrease in effective liquid diffusion coefficient of over 50 %. Vertically, liquid diffusion coefficients showed a dependance on solids volume fraction for the full range of liquid properties. For liquid properties representative of early stages after injection, sections with higher solids volume fraction showed the largest rates of spreading. With the increase in viscosity (or decrease in surface tension) diffusion coefficients dropped by between 50 and 80 %. The range of liquid parameters examined did not cover the total range experienced within a fluid coker, with the T_v value representing the ratio of liquid viscosity to surface tension varying by two orders of magnitude.

While more prominent vertically, the lower solids volume fractions showed sharper decreases in diffusion coefficient at earlier times (lower viscosities), followed by the eventual independence of the diffusion coefficient on liquid properties. Higher solids volume fractions did not experience a liquid property independent region for later times in the liquid lifespan. From these trends, it was concluded that the main mechanisms for liquid spreading in lower solids volume fractions was that of particle motion. At higher solids volume fractions, the spreading was dominated by exchange during collisions.

Effective liquid diffusion coefficients ranged in value from $\Gamma/(U_{\infty}D) = 0.39 - 1.14$ horizontally and $\Gamma/(U_{\infty}D) = 0.74 - 4.39$ vertically, depending on liquid properties and solids volume fraction.

Chapter 4

Aggregation due to Liquid Bridges

Aggregation of particles is common in industrial processes that involve liquid spraying, such as coating, flocculation, granulation, and drying [9]. For some applications, aggregation is a desired effect, increasing the size of a product through the introduction of a binding liquid. This is applied in various industries, including chemical, food, fertilizer, pharmaceutical, and detergent [3]. However, aggregation is a negative consequence of other industrial applications, such as fluid coking, catalytic cracking, and biomass co-firing.

In fluid coking, aggregation occurs when bitumen-coated coke particles collide and stick. This results in granules of up to several hundred coke particles [3], reducing process efficiency (uniformity and rate of mixing). The presence of aggregates results in a lower surface area to volume ratio compared to single particles, resulting in higher settling rates and reduced surface area for heat transfer. Less heat transfer results in slower bitumen cracking, and shifts the production towards the formation of petroleum coke away from the production of light gaseous hydrocarbons. Excess aggregate production can lead to fouling, slugging or defluidization [3].

The fluidization behavior and aggregation behavior are interdependent. Fluidization behavior is influenced by particle size, shape, roughness, and density. For aggregating particles, the properties of aggregates determine the fluidization characteristics. Therefore, an understanding of aggregation is important to characterize the resulting fluidization behavior. Aggregation behavior is dependent on the flow conditions. Frequent collisions and gas-particle drag result in dynamic formation and breakage of aggregates, depending on the strength of the binding liquid, velocity of surrounding gas, and relative velocity of collisions. The aggregating strength of the liquid is dependent on its surface tension and viscosity, since aggregates form due to the formation of pendular liquid bridges between adjacent particles. A significant amount of work has gone into understanding the fundamentals of the aggregation process [35; 80].

An understanding of wet granulation requires examination on the micro-scale. The competing forces acting on two particles attached via liquid bridge, resulting in their eventual aggregation or splitting, must be determined. As reviewed in Section 2.3.3, the related non-contact inter-particle forces are capillary and viscous forces.

For the application of fluidized beds, the coalescence models to date are limited. Larger scale simulations determine an overall restitution coefficient and collision outcome (sticking or separation) [3]. Smaller scale simulations account for the liquid bridge forces directly, accounting for particle-gas interaction by calculating a net porosity in fluid nodes due to particles and calculating a fluid node drag that is applied to sub-grid particles [18]. However, to date there have been no simulations that fully resolve the gas dynamics surrounding the particles, allowing the gas to directly influence the aggregate formation and breakage.

In many coalescence models, the attractive capillary force is dependent on the liquid bridge volume [13; 18]. To date, simulations have used a constant liquid bridge volume for the calculation of the capillary force. As discussed in Section

2.3.2, the liquid bridge volume grows as a function of time, and is dependent on the liquid viscosity and surface tension. This additional dependency on liquid properties indirectly allows for various residence times of bitumen to be modeled. This is because, after injection, cracking of the bitumen results in drastic changes in properties over a short time, with viscosity increasing by 4 orders of magnitude within 10 seconds of cracking [8].

In this chapter a millimeter cubed portion of a fluidized bed is simulated, fully resolving the gas-particle interactions and implicitly modeling the liquid presence through the application of a capillary force on the particles. The effect of aggregation on the fluidization is examined, relating the drag on the particles due to the gas to the aggregation due to liquid bridges. The changes in aggregate size distribution and mean slip velocity of the particles are examined by modifying the type and amount of liquid.

4.1 Problem Statement

We examine the formation of aggregates by means of pendular liquid bridge formation. The problem is described in two stages. First, the interaction of two particles is discussed in terms of the application of an attractive capillary force. This is followed by the effect that liquid bridges have on multi-particle systems in a gas fluidized bed.

4.1.1 Capillary Forces between Two Particles

Consider two identical solid spherical particles of diameter D approaching, as shown schematically in Figure 4.1a. For this problem, particles are approaching with initial translational velocities of magnitude v.

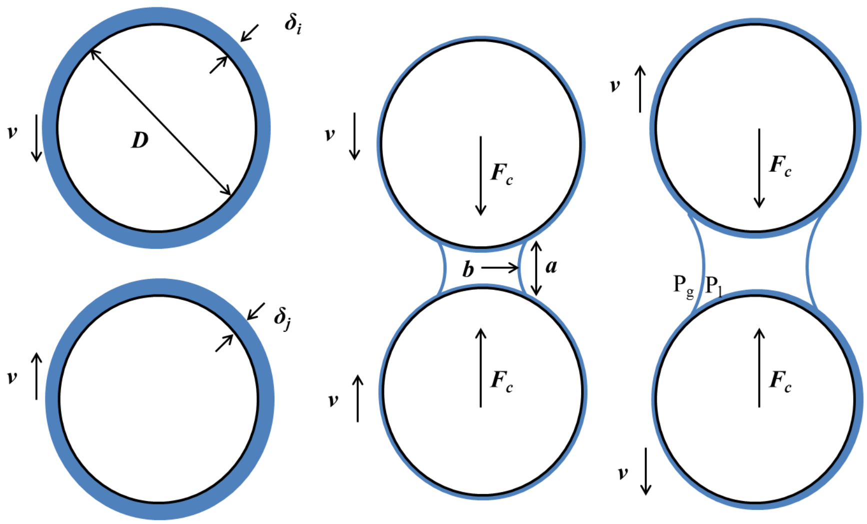

a) Particle approach. b) Bridge formation. c) Bridge growth.

Figure 4.1: Evolution of liquid bridge.

Once the liquid layers touch, a liquid bridge is formed between the particles, as shown in Figure 4.1b. The liquid bridge results in various forces being imposed on the particles. As discussed in Section 2.3.3, only the capillary force is introduced in the simulations. The capillary force is due to the Young-Laplace pressure difference between the liquid in the bridge and the gas outside of the bridge $(P_l - P_g)$. A lower pressure within the liquid bridge pulls the particles towards one another. The capillary force equation implemented in the simulations is Equation (2.38).

For this model, asymmetry in the force applied exists due to the growth of the liquid bridge. For two particles to remain connected (independent of collisions with other particles and drag force), the initial relative velocity and increase in relative velocity due to capillary force during approach must be overcome by the decrease in relative velocity due to capillary force upon rebound.

The liquid bridge volume V_{lb} grows over time when particles are within $0 < a < \delta_i + \delta_j$. The bridge radius is limited to $D/2$ and liquid mass conservation is ensured, with the total volume of liquid in the bridge not exceeding the sum of liquid on the respective particles. The associated capillary force is also applied over this time.

The liquid characteristics that effect the resulting capillary force are the liquid film thickness δ and the capillary Reynolds number Re_c (details in Section 2.4.7. The film thickness affects the time in which the particle films remain overlapped, which relates to the liquid bridge volume. Additionally, thicker films result in capillary force being applied to a larger range of particles. The capillary Reynolds number affects the rate of liquid bridge growth, and therefore the strength of the applied force.

4.1.2 Aggregation in a Fluidized Bed

Consider a gas-solid fluidized bed. The particles are equally wetted with a uniform film thickness δ. The solids volume fraction of the fluidized bed is given by ϕ (and varies over position). Because the particles are wet, liquid bridges form between adjacent particles, resulting in temporary attraction of the particles. The particles may either remain aggregated or break up, depending on interactions from other particles or the dynamics of the surrounding gas.

The dynamics in the system result in a dynamic aggregate size distribution due to the balance between capillary and hydrodynamic forces. As an aggregate grows, decreased surface area is exposed to the gas, and reduced particle concentration voids are created. The local drag force in these voids is lower than the volume-averaged drag force in the system, resulting in increases in gas velocity. This is balanced by high particle concentration regions, where the velocity of the gas is significantly reduced. The apparent density of an aggregate is larger than within the surrounding mixture, resulting in the aggregate settling more quickly. This results in an increase in gas velocity upwards and particle settling downwards.

These increased velocity magnitudes result in larger slip velocities at aggregate surfaces, eventually leading to the breakage of particles from aggregates. This balancing of effects leads to the development of an aggregate size distribution. By tracking aggregate sizes and gas-solid slip velocity experienced by the particles, the impact of introducing a capillary force on the fluidization can be determined. An aggregate size distribution can be calculated and tracked over time. If the capillary forces are significantly stronger than the hydrodynamic forces, complete aggregation of the particles will occur. Conversely, dominant hydrodynamic forces will result in breakage of aggregates quickly, resulting in a non-aggregating system. A balance of these forces will result in a dynamically steady aggregate size distribution, with continuous formation and breakage of aggregates.

4.2 Model Development

The motion of one particle, based on Newton's Second Law and considering capillary forces due to the liquid bridge is described in Section 2.1, Equation (2.5). Assuming the liquid bridge is small enough to ignore the effects of gravity, the capillary force is determined by the capillary pressure. The capillary force used is shown in Equation (2.38).

With all particles being equally coated, the value $\delta_i + \delta_j$ will be constant and equal for all interacting particles. The liquid bridge volume V_{lb} is based on the viscous bridge growth discussed in Section 2.3.2.

All simulations are performed in a 10.4D cubic domain.

4.2.1 Analysis Methodology

To examine the effect that the capillary force has on the fluidization behavior, it is important to track the formation and breakage of liquid bridges, and examine the resulting aggregates that are formed. Overall, the formation of aggregates should lead to changes in the volume-averaged particle-gas slip velocity and the volume-averaged settling Reynolds number.

In order to determine aggregate sizes, the overlapping of liquid films is tracked throughout the simulation time. Particles are deemed to be connected when their liquid films overlap. Summing the connected particles determines the aggregate sizes, and therefore aggregate size distributions.

Since the particles have a net downward motion and the fluid a net upward motion, the relevant velocity to consider for the Reynolds number and drag force is the volume-averaged slip velocity between solid and gas U_{sl}, as defined in Equation (4.1).

$$U_{sl} = (1 - \phi)\left(\overline{u_z} - \overline{v_z}\right) \tag{4.1}$$

From this, the average drag force acting on a particle due to the gas, $\mathbf{F}_{s,d}$, can be determined as follows. Since the liquid has no direct impact on the gas phase, a force balance on the gas phase results in the buoyancy force described in Equation (2.14) balancing the drag force from the particles (or $\mathbf{F}_{g,b} = -\mathbf{F}_{g,d}$). Therefore, the drag force on a particle can be defined as in Equation (4.2).

$$
\begin{aligned}
\mathbf{F}_{s,d} &= -\frac{\mathbf{F}_{g,d}}{N_{tot}} && (4.2)\\
&= (\rho_m - \rho_g)\frac{V_g g}{N_{tot}}\mathbf{e}_z && (4.3)\\
&= (\rho_m - \rho_g)V_s g\frac{(1-\phi)}{\phi}\mathbf{e}_z && (4.4)
\end{aligned}
$$

With the assumption that the solids volume fraction ϕ is constant throughout the domain, this average drag force on a particle is constant and an input of the simulation [56]. The output of the simulations, specifically U_{sl}, can therefore be expressed by non-dimensionalizing the particle drag force [56; 81; 82].

$$
F_d = \frac{\mathbf{F}_{s,d} \cdot \mathbf{e}_z}{3\pi\mu_g D U_{sl}} \tag{4.5}
$$

The volume-averaged settling Reynolds number is defined as follows.

$$
Re_{sl} = \frac{\rho_g D U_{sl}}{\mu_g} \tag{4.6}
$$

4.3 Results and Discussion

With the implementation of the capillary force, the effect of various properties on fluidization and aggregate formation can be examined. The properties considered are the solids volume fraction, liquid properties and film thickness (specified in Table 2.2). The results are organized as follows. First the collision frequency f and average number of liquid bridges per particle N_{lb} are examined, in order to separate cases into fully-aggregating, partially-aggregating, and non-aggregating systems. Space-time plots of local solids volume fractions and three-dimensional visualizations are additionally used to qualitatively examine the aggregation behavior.

For the partially aggregating systems, the effect of solids volume fraction ϕ and liquid film thicknesses δ on the volume-averaged Reynolds number Re_{sl} and average normalized drag force on a particle F_d are examined.

4.3.1 Presence of Aggregates

To ensure that the addition of an external capillary force results in aggregation, characteristics of the resulting fluidization behavior are examined and the results are visualized. A consequence of aggregation is an increase in collision frequency. The particles within an aggregate will continue to bounce off one another, but are drawn in again due to the presence of the capillary force or collisions with surrounding particles. By comparing the non-aggregating case with aggregating cases, the significance of the applied attractive force on aggregation is examined, as shown in Figure 4.2. The simulations are all initialized with the same gas and particle dynamics. The steady state collision frequencies for the curves represented by circles and squares in Figure 4.2 are 0.14 and 0.18, respectively.

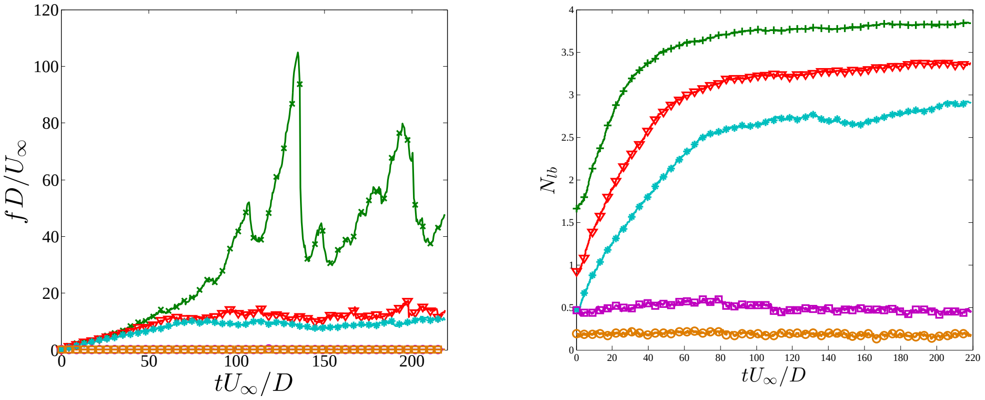

(a) Collision frequency over time. Thick curves overlap just above the x-axis.

(b) Volume-averaged number of liquid bridges per particle.

Figure 4.2: Particle interactions for $\phi = 0.3$, comparing the aggregating cases tested: $Re_c = 4.4 \times 10^{-4}$ for green crosses ($\delta/D = 0.08$), red triangles ($\delta/D = 0.04$), and light blue stars ($\delta/D = 0.02$). $Re_c = 2.2 \times 10^{-6}$ for purple squares ($\delta/D = 0.02$), and orange circles ($\delta/D = 0.008$).

From Figure 4.2, certain ranges of properties (Re_c and δ/D) show a distinct increase in the collision frequency. However, for lower values of Re_c and δ/D, the effect of the external force seems to be negligible. Similarly, the number of liquid bridge connections increases from an initial state to a new steady state for the aggregating cases. As expected, higher capillary Reynolds number Re_c and larger liquid film thickness δ result in more aggregation. Comparing the light blue stars and purple squares shows that, even for the same liquid film thickness and solids volume fraction, the aggregation behavior significantly differs based on liquid properties. The higher capillary Reynolds number results in a faster liquid bridge growth, resulting in a higher attractive force between particles.

Because two aggregating particles are defined as having their liquid films overlap ($a \leq \delta_i + \delta_j$), the initial non-aggregating system will have a number of spheres within the range $a \leq \delta_i + \delta_j$. The initial values of 4.2b differ due to varying initial film thicknesses, with larger film thicknesses having higher numbers of particles within the range.

A clearer picture of the evolution of aggregates can be achieved by examining a two-dimensional slice of the domain over time. The evolution of the aggregating system is shown in Figure 4.3 for $\phi = 0.3$, $Re_c = 4.4 \times 10^{-4}$, $\delta/D = 0.02$ (light blue stars in Figure 4.2).

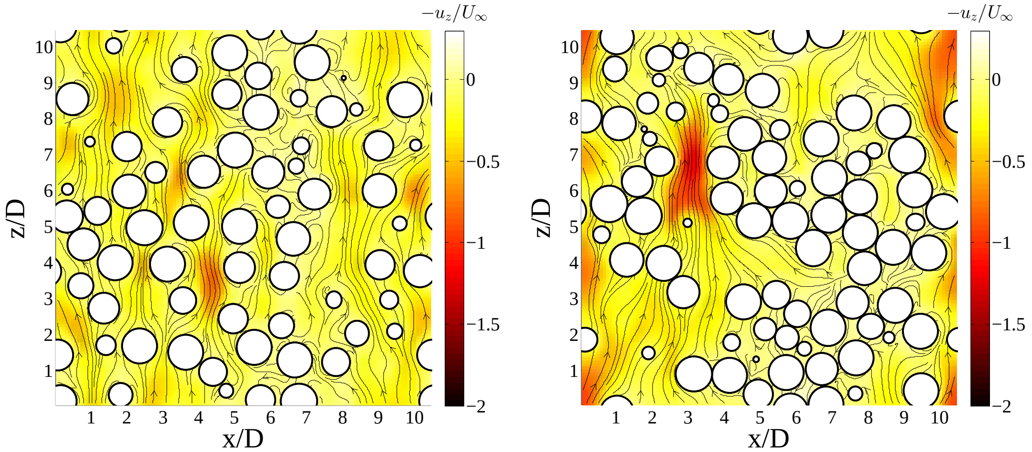

(a) $tU_\infty/D = 0$.

(b) $tU_\infty/D = 57$.

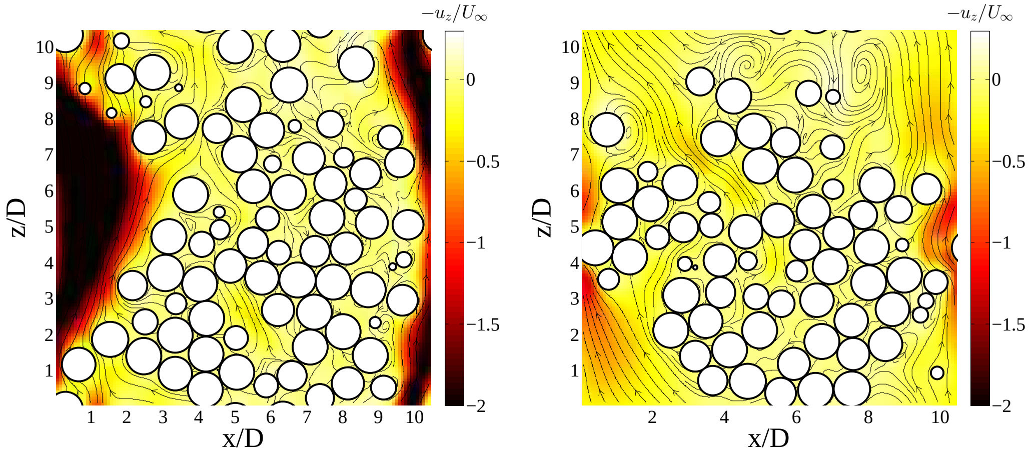

(c) $tU_\infty/D = 114$.

(d) $tU_\infty/D = 215$.

Figure 4.3: Visualizations of aggregate formation over time. $\phi = 0.3$, $Re_c = 4.4 \times 10^{-4}$, $\delta/D = 0.02$.

In Figure 4.3, one large aggregate forms over time. The system starts off being well-dispersed (Figure 4.3a). Over time, larger particle-free zones emerge, with particles clearly clumping. While this figure clearly shows a change in fluidization behavior, a three-dimensional visualization allows for a more complete qualitative examination of the effect of a capillary force on the fluidization. Based on Figure 4.2, the time can be determined when a new dynamic steady state is reached. The three least aggregating cases for $\phi = 0.3$ are visualized in Figure 4.4, along with their respective space-time plots. The two cases not shown aggregate completely, showing behavior similar to that of Figure 4.4a.

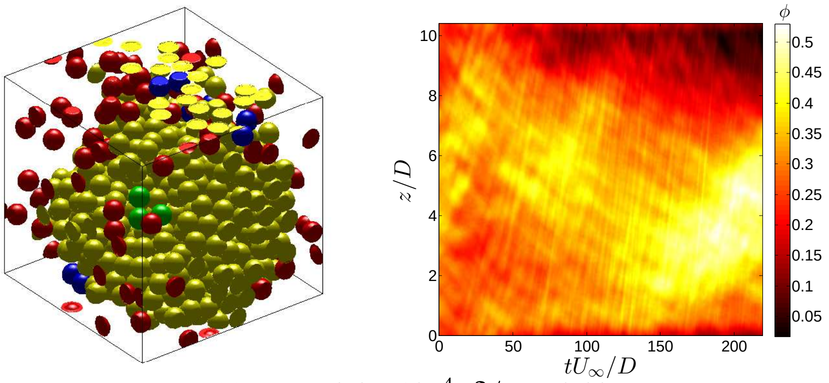

(a) $Re_c = 4.4 \times 10^{-4}$, $\delta/D = 0.02$.

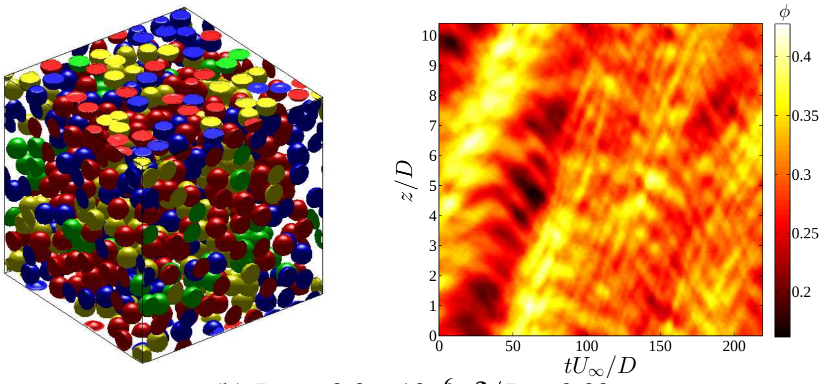

(b) $Re_c = 2.2 \times 10^{-6}$, $\delta/D = 0.02$.

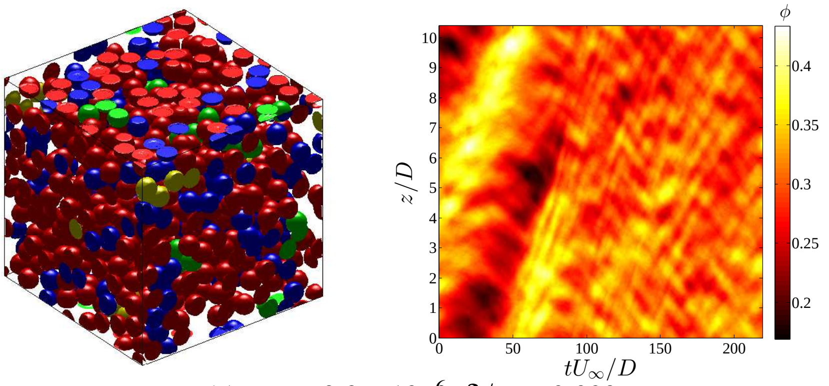

(c) $Re_c = 2.2 \times 10^{-6}$, $\delta/D = 0.008$.

Figure 4.4: Visualization of particle positions and aggregate sizes at $tU_\infty/D = 175$ and space-time plots of local solids volume fraction for $\phi = 0.3$. Particles are colored according to the size of aggregate to which they belong. Single particles are red, doubles are blue, triples are green, and aggregates of four or more are yellow.

Figure 4.4 shows that the liquid properties and liquid film thickness play a significant role in the resulting aggregation behavior. In Figure 4.4a, a domain-size aggregate develops. A decrease in the capillary Reynolds number Re_c results in a larger variety of aggregate sizes. Finally in Figure 4.4c, a decrease in liquid film thickness results in less aggregation, with the majority of particles being single. However, the presence of a capillary force continues to impact the fluidization, with the breaking of the wave-type instabilities observed in non-aggregating systems (as shown for example in Figure 3.14.

In systems of monosized spheres, the presence of wave instabilities has been shown experimentally [78; 83] and mathematically, through numerical integration of volume-averaged equations of motion [84]. However, the behavior and presence of these one-dimensional instabilities in gas-fluidized beds of aggregating particles has not been extensively studied. With the introduction of an aggregating force, particles within close proximity (in the peaks of the wave instabilities) are likely to aggregate, resulting in increased slip velocities and therefore faster settling. The aggregates that form physically lower within a wave peak are less hindered by particles below, and separate from the wave. This is shown in Figures 4.4b and 4.4c, with the waves breaking into smaller, distinct sections beginning at the lower section of the wave. With the addition of an aggregating force, an aggregate size distribution is achieved. This mimics a polydisperse system of particles, which has been shown to bubble less pronouncedly [78], and consequently have smaller scale instabilities.

The development of an aggregate of the order of the domain creates a physically unrealistic system. Because of the periodic boundary conditions, this aggregate interacts with itself over the boundaries. Therefore, the simulation space is no longer representative of a large homogeneous system, and the drag force and resulting volume-averaged particle settling Reynolds number cannot be used. In order to determine liquid ranges that lead to partial aggregation for all solids volume fractions

ϕ, a different range of parameters is considered for each solids volume fraction. The capillary Reynolds number Re_c and non-dimensionalized liquid film thickness δ/D studied for each solids volume fraction ϕ are summarized in Table 4.1. Additionally, the effect of the capillary force is described, in terms of fully-aggregating, partially-aggregating, and non-aggregating behavior.

This classification is based on the figures shown above: particle collision frequency, average number of liquid bridges per particle, three-dimensional visualization and space-time plots of particle concentration. Cases that show no change in any of these figures are considered non-aggregating. Fully-aggregating systems show space-time plots with all particles migrating into one area, and three-dimensional visualizations showing almost exclusively aggregates of four or more particles and large spaces with few particles present. Additionally, increases in collision frequency and average number of liquid bridges per particle are observed, often not reaching a steady state within the simulation time. Systems showing changes in average number of liquid bridges and particle collision frequencies, but not resulting in complete aggregation are characterized as partially-aggregating and analyzed further.

Table 4.1: Aggregate simulation properties and resulting behavior.

Solids Volume Fraction, ϕ	Capillary Reynolds Number, Re_c	Liquid Film Thickness, δ/D	Aggregate Behavior
0.3	4.4×10^{-4}	0.08	fully
		0.04	fully
		0.02	fully
	2.2×10^{-6}	0.02	partially
		0.008	partially
0.4	4.4×10^{-4}	0.08	fully
		0.04	fully
		0.02	fully
		0.008	fully
	2.2×10^{-6}	0.04	fully
		0.02	partially
0.5	4.4×10^{-4}	0.08	fully
		0.04	fully
		0.02	fully
		0.008	fully
	2.2×10^{-6}	0.02	fully
		0.008	partially
	2.2×10^{-9}	0.0008	non
0.55	4.4×10^{-4}	0.08	fully
		0.008	fully
	2.2×10^{-6}	0.02	fully
		0.008	fully
	6.6×10^{-8}	0.008	fully
	2.2×10^{-9}	0.0008	non

Table 4.1 shows that the majority of simulations result in full aggregation, limiting the further analysis of steady state slip Reynolds number and non-dimensionalized drag force. Comparison of the system at different solids volume fractions ϕ with the same liquid properties and film thicknesses shows that, as expected, higher solids volume fractions result in more aggregation.

The formation of aggregates is a competition between the hydrodynamic forces of the gas-particle and particle-particle interactions, and the attractive forces between particles due to a liquid bridge capillary force. The higher inertia present in the lower solids volume fraction systems results in an increased likelihood of connected particles escaping one another's liquid-induced attraction. Conversely, higher solids volume fraction systems have slower moving particles and more frequent collisions. The lower particle momentum results in particles more frequently not overcoming the capillary force and escaping the liquid bridge. While the close proximity of particles increases collision frequency, promoting momentum transfer and therefore aggregate breakage, it also hinders particle motion.

For the highest solids volume fraction $\phi = 0.55$, the close proximity of the particles insures that the system practically always aggregates, since any sort of physically realistic liquid film thickness results in a large portion of particles being considered as aggregating initially. The lower particle inertia and higher collision frequency result in more particle connections being formed and maintained, leading to large aggregate formation. For these cases, the distinguishable difference observed between a fully-aggregating and non-aggregating system is the collision frequency f and the number of liquid bridges per particle N_{lb}. The non-aggregating simulation at $\phi = 0.55$ show no significant deviation from the initial condition for either f or N_{lb}. Since no partially-aggregating case was found for $\phi = 0.55$, this solids volume fraction will not be considered in the remainder of the chapter.

4.3.2 Changes in Drag Force due to Aggregation

For the aggregation cases that do not completely aggregate, changes in particle drag force F_d and volume-average particle slip Reynolds number Re_{sl} are examined. In order to compare aggregating systems for a range of properties, the average drag force is normalized based on its non-aggregating value ($F_d/F_d|_{t=0}$).

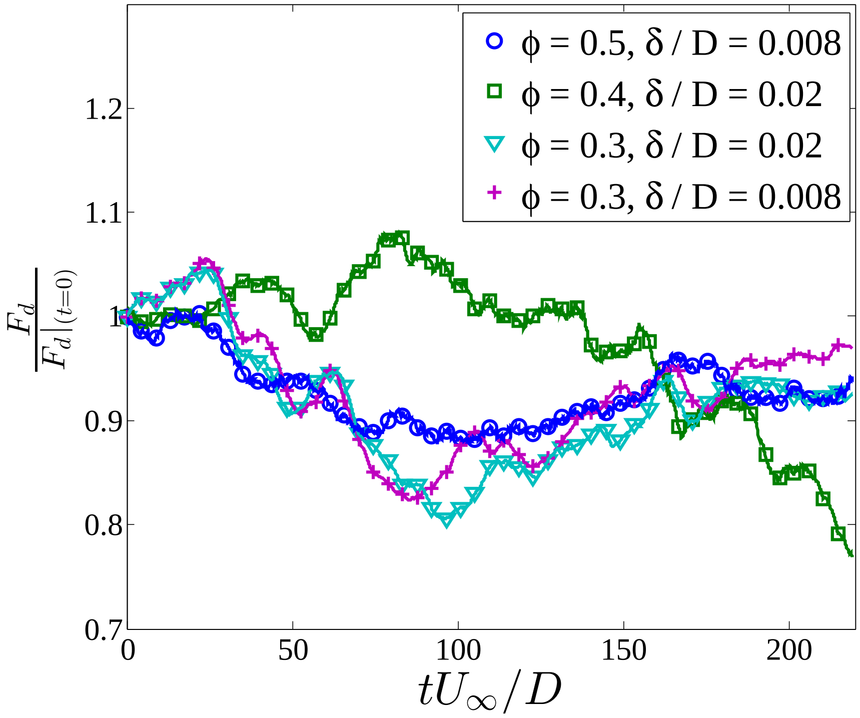

Figure 4.5: Normalized drag force as a function of time for partially-aggregating cases. $Re_c = 2.2 \times 10^{-6}$.

The drag force trend for $\phi = 0.4$, $\delta/D = 0.02$ does not reach an aggregate steady state in the simulation time. This case was simulated for an additional non-dimensional time totalling to 490, but did not reach a steady state. Examining the vertical space-time plot shows that the wave instabilities observed were stable for the first half of the simulation time, but then dispersed (Figure 4.6a). Space-time plots of concentration in the x-direction showed the development of a large aggregate (Figure 4.6b). Since horizontally the particle velocities are slower than vertically, this more prominant aggregation is not unexpected. The dispersion of the wave instabilities vertically occurs at a similar time as the dispersion of the horizontal aggregate, and represents a peak in the volume-averaged slip Reynolds number (Figure 4.6c).

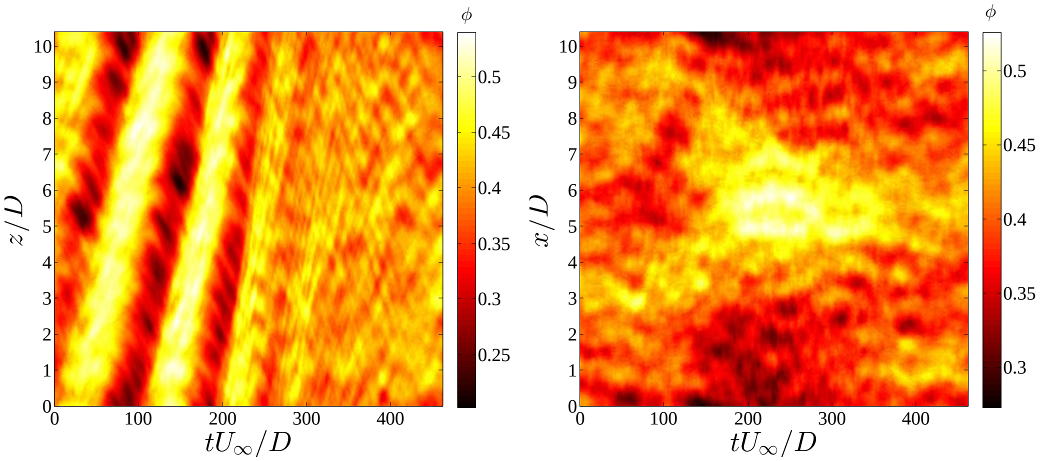

(a) Vertical direction space-time plot of concentration.

(b) Horizontal direction space-time plot of concentration.

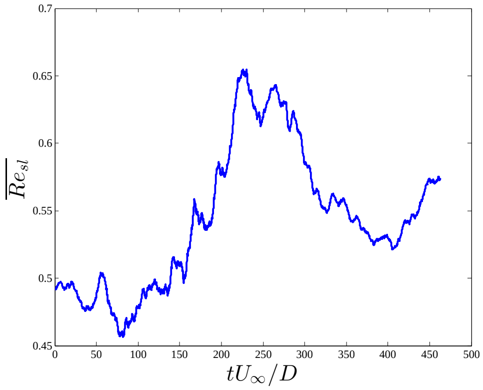

(c) Volume-averaged slip Reynolds number.

Figure 4.6: Evolution of concentration and Reynolds number over time for extended simulation. $\phi = 0.4$, $\delta/D = 0.02$, $Re_c = 2.2 \times 10^{-6}$.

Figure 4.5 shows similar trends for the data at $\phi = 0.3$ and $\phi = 0.5$, with the drag force decreasing by less than 10 %. Aggregate size distributions for the partially-aggregating systems are presented in Figure 4.7. The case for $\phi = 0.4$ is averaged from $tU_\infty/D = 400$, even though the system is not yet steady in terms of the slip velocity. This provides insight into the aggregate sizes once the accumulation in the horizontal direction is dispersed. The remaining results are averaged over 150 realizations, after the aggregating system has reached its aggregate steady state, over a time span of $tU_\infty/D = 65$. The aggregate size distributions are mass-weighted. $g(N_{agg})$ represents the fraction of the total mass of particles in the simulation present in aggregates of size N_{agg}.

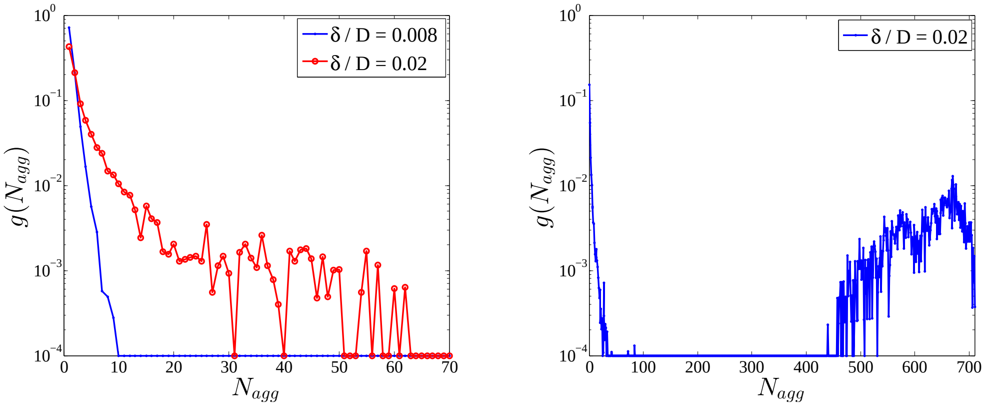

(a) $\phi = 0.3$. From thinner film to thicker film, $\overline{N_{agg}} = 1.40, 4.39$. $N_{tot} = 648$.

(b) $\phi = 0.4$. $\overline{N_{agg}} = 445$. $N_{tot} = 864$. This simulation is not steady.

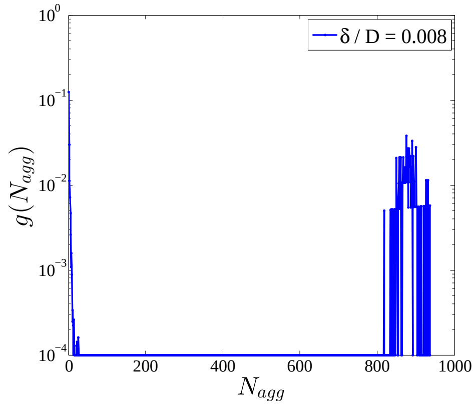

(c) $\phi = 0.5$. $\overline{N_{agg}} = 716$. $N_{tot} = 1080$.

Figure 4.7: Aggregate size distributions for $Re_c = 2.2 \times 10^{-6}$. $g(N_{agg})$ values below 10^{-4} are set to 10^{-4} for plotting purposes.

Figure 4.7a shows that thicker films result in larger aggregate sizes, shifting the aggregate size distribution to the right. Additionally, higher solids volume fractions result in an aggregate size distribution skewed to the right. While the case at $\phi = 0.4$

did not reach a steady state, the aggregate size distribution shows a large range of aggregate sizes, with the largest being approximately 52% of the total particle count. Additionally, although the case for $\phi = 0.5$ reached a new aggregate steady state drag force, the aggregate size distribution leans towards a fully-aggregating system.

By examining the initial system, the extent of the aggregating effect can be gauged. Comparison of the initial average aggregate size to the steady state average aggregate size is shown in Table 4.2.

The mass-averaged aggregate size $\overline{N_{agg}}$ is defined in Equation (4.7) [56].

$$\overline{N_{agg}} = \sum_{N_{agg}=1}^{N_{tot}} N_{agg} g(N_{agg}) \tag{4.7}$$

Table 4.2: Change in mean aggregate size and volume-averaged particle Reynolds number. $Re_c = 2.2 \times 10^{-6}$.

ϕ	δ/D	$\overline{N_{agg}}\|_{t=0}$	$\overline{N_{agg}}$	$\overline{N_{agg}}/\overline{N_{agg}}\|_{t=0}$	$Re_{sl}\|_{t=0}$	Re_{sl}	$Re_{sl}/Re_{sl}\|_{t=0}$
0.3	0.008	1.51	1.32	0.93	0.948	1.03	1.08
0.3	0.02	3.33	4.39	1.31	0.948	1.04	1.10
0.4	0.02	126	445	3.53	-	-	-
0.5	0.008	584	716	1.23	0.248	0.268	1.07

Despite the case $\phi = 0.3$, $\delta/D = 0.008$ showing a drop in normalized drag force $F_d/F_d|_{t=0}$ in Figure 4.5 and an aggregate size distribution with aggregates of up to 10 particles, Table 4.2 shows a slight decrease in the average aggregate size at the new steady state. This is counter-intuitive, given the slight increase in particle Reynolds number. However, case $\phi = 0.3$, $\delta/D = 0.02$ shows a clear increase in aggregate size, but with a similarly small increase in the Reynolds number.

Because of the lack of partially aggregating cases and limits due to domain size, the analysis of the effect of ϕ, δ/D and Re_c on the particle volume-averaged Reynolds number and drag force cannot be further quantified.

4.4 Conclusions

In this chapter an attractive capillary force was applied to the previously developed interaction-time dependent bridge growth model, for aggregating systems in gas-fluidized beds. Various solids volume fractions, film thicknesses, and liquid properties were examined. The resulting development of aggregates was analyzed by tracking the evolution of particle-particle collision frequency, average number of liquid bridges per particle, and average drag force per particle over time. Additionally, space-time plots of local solids volume fraction in the vertical direction were examined. From these observations, the extent of the aggregation was determined, classifying the system as fully, partially, or non-aggregating.

Further analysis was performed on the partially aggregating cases, determining the aggregating dynamic steady state average drag force and average particle Reynolds number based on the slip velocity. Additionally, aggregate size distributions were examined, and the change in the mean aggregate size was determined. Cases where complete aggregation occurred could not be further analyzed, since the interaction of these aggregates with themselves over the domain boundaries was unphysical, and not representative of a large-scale fluidized system.

For the majority of cases simulated, the capillary force introduced to produce aggregation was significantly stronger than the competing hydrodynamics, resulting in aggregation of the majority of particles into one large aggregate. For the highest solids volume fractions ($\phi = 0.55$), the close proximity of particles and low particle velocities resulted in complete aggregation for all reasonable cases. In order to observe no aggregation effect at this solids volume fraction, the film thickness and liquid property variable Re_c had to be reduced by two and three orders of magnitude, respectively.

As expected, decreasing the solids volume fraction resulted in less aggregation. Additionally, thicker liquid films on the particles and a higher Re_c (representing the relationship between surface tension and liquid viscosity) led to larger aggregate formation. The formation of a partially aggregating system resulted in an increase in the volume-averaged particle Reynolds number and a decrease in the average drag force per particle.

Due to the lack of partially aggregating cases, conclusions regarding how liquid properties and solids volume fraction affect the fluidization within a fluid coker could not be drawn. Physical liquid properties present in commercial fluid coking resulted in aggregate sizes greater than those simulated for the solids volume range $\phi = 0.3 - 0.5$, for the majority of cases. Further analysis of aggregating systems requires larger domains that are able to capture the larger scales required.

Chapter 5

Conclusions

5.1 Summary

The primary goal of this work was to improve the understanding of the physics behind liquid spreading due to particle collisions and aggregation in a fluid coker. By quantifying liquid spreading and aggregation, and examining how liquid affects the fluidization, the results can be incorporated into larger scale simulations or work to enhance knowledge of the overall fluid coking process. The work was divided into two sections: examination of liquid spreading and aggregation in a homogeneously wetted system. A range of parameters was studied in order to implicitly examine various heights within the fluid coker by varying solids volume fraction, as well as to examine various times in the evolution of the liquid phase by varying liquid viscosity and surface tension. To study these effects, direct numerical simulations of gas-solid fluidization were performed using the lattice-Boltzmann method. The liquid phase was introduced as a scalar on the particles, representing the liquid film thickness on the particles. For studies of liquid spreading, the liquid scalar was passive, not affecting the fluidization behavior. Studies of aggregation introduced an external force on the particles relative to the liquid scalar. The solids volume fractions considered ranged from $\phi = 0.3$ to $\phi = 0.55$. In this section, the main observations are summarized.

5.2 Conclusions regarding Liquid Spreading

The main goal of this section was to examine the micro-physics of transferring liquid as a result of particle-particle collisions and to determine liquid spreading rates. The spreading of liquid was examined by simulating liquid motion from an initial plane of wet particles throughout the domain. By examining a wetted-plane initial condition, the liquid spreading horizontally and vertically could be analyzed independently. The particle velocities are greater in the vertical direction and therefore liquid spreading was expected to be greater vertically. Concentration profiles were determined based on location and time, and a non-linear fit was performed in order to determine effective liquid diffusion coefficients. The key conclusions from this section are as follows:

- The spreading of liquid through the gas-fluidized bed can be approximated as a diffusion process. Comparison of normalized concentration profiles throughout the simulation time resulted in overlapping curves, and therefore an approximate diffusion coefficient.
- Four domain sizes were examined. This includes two cubic domains with lengths representative of 0.9 *mm* and 1.5 *mm* within a fluid coker respectively. Additionally, two rectangular domains were considered, both with a square base of length 0.9 *mm*, and heights of 1.8 *mm* and 3.6 *mm*. A dependence on the resulting diffusion coefficients was observed in both the horizontal and

vertical directions. Horizontally, only the largest cubic domain showed differences in the diffusion coefficient compared to the other domains, with the non-dimensionalized diffusion coefficient varying by a factor of 2.8 at most. Differences between domain sizes decreased with increasing liquid viscosities or decreasing surface tensions. Vertically the domain size dependence was more drastic, with the diffusion coefficient varying by up to a factor of 3.7 between the steady-state domains. The domain chosen for the analysis was the second largest in the vertical direction. Qualitative differences in wave instability amplitudes were observed between cubic and rectangular domains. Larger domains are required to ensure domain size independence. The domains required need to allow for the formation of two-dimensional instabilities. Therefore, the horizontal direction should be increased while maintaining the height, with a cubic domain of 3.6 *mm* being considered and compared with the previous domains.

- Three liquid spreading rules were examined, and resulted in differences in effective liquid diffusion coefficient. The equal spreading [15; 33] and geometrical spreading [16] rules are independent of liquid properties. Therefore, in order to study how liquid spreading changes over time, a third interaction-time dependent spreading rule was developed based on the work of Gross et al. [39]. The equal and geometrical spreading rules resulted in non-dimensionalized diffusion coefficients that varied by factors of at most 1.8 and 4.5 for the horizontal and vertical directions, respectively. The interaction-time dependent spreading rule encompassed the results of the other two spreading rules for the liquid properties examined.

- Liquid spreading was found to be quicker vertically than horizontally for all solids volume fractions by a factor of between 1.4 and 4.3. This factor was greater at lower solids volume fractions, due to the increased velocities of particles vertically.

- Increase of the liquid viscosity and decrease in surface tension resulted in a decrease in the rate of liquid spreading, regardless of the solids volume fraction. Therefore, over the lifespan of liquid within a fluid coker, the large increase in liquid viscosity will result in decreases to the rate of liquid spreading. While surface tension is additionally considered, the change in this liquid parameter over time is minor compared to the 4 magnitude change observed for viscosity within 10 seconds of liquid injection. Only a fraction of the viscosity range experienced within a fluid coker is considered, with the ratio of surface tension and viscosity being varied by 2 orders of magnitude. Over the range considered, the diffusion coefficients in the vertical and horizontal directions dropped by factors of 2.6 and 5.1, respectively.
- At early times in the liquid lifespan (represented by low liquid viscosities), higher solids volume fractions resulted in quicker liquid spreading. As the viscosity increased (or surface tension decreased), the low solids volume fraction systems showed a larger decline in diffusion coefficient initially, followed by a diffusion coefficient independent of the liquid properties. This independence on liquid properties at high viscosities and low surface tensions was not observed for higher solids volume fractions. These trends resulted in quicker liquid spreading vertically for lower solids volume fractions at the high viscosity limit.
- Four mechanisms for liquid spreading were considered and analyzed: the mean particle velocity, the variance in the particle velocities, the speed of

collisions, and the frequency of collisions. The mean particle velocity was found to not affect spreading, as this velocity was several orders of magnitude lower than the deviations in velocity. The other three mechanisms were found to contribute to the liquid spreading. Variances in particle velocities dropped by factors of 5.6 and 3.4 for the vertical and horizontal directions, respectively, with the relative increase of the solids volume fraction from 0.3 to 0.55. The average relative velocities of collision followed a similar trend, decreasing by a factor of 6 over the same range of solids volume fractions. These effects were balanced by the collision frequency, which increased by a factor of 3. Because of these competing effects, the solids volume fraction that resulted in the quickest spreading varied based on liquid properties.

- When scaled back into a physical system, the effective liquid diffusions determined ranged from 5.12×10^{-5} - 3.04×10^{-4} m^2/s vertically and 2.70×10^{-5} - 7.89×10^{-5} m^2/s horizontally. Defining a diffusion length as $\sqrt{4\Gamma t}$ and setting the time equal to 10 seconds, the distance over which liquid spreads was calculated. Horizontally, this distance ranged from 0.032 - 0.056 m. Liquid spread more quickly vertically, reaching a distance of between 0.04 and 0.11 m. Considering the size of the fluid coker compared to the liquid transfer characteristic lengths, the effect of liquid spreading due to particle-particle collisions and particle motion is minimal.

5.3 Conclusions regarding Particle Aggregation

In order to examine the aggregation of particles due to liquid bridges, the liquid film thickness scalar was used to determine the proximity at which a capillary force was applied to nearby particles and the growth of the force over the interaction time. The goal of this section was to quantify the aggregation by examining the aggregate sizes and aggregate size distributions. The effect of aggregation on the fluidization behavior was examined by comparing changes in particle slip velocity (through volume-averaged per particle drag and volume-averaged particle Reynolds number). The main conclusions are as follows:

- A thinner liquid film on the particles resulted in less formation of liquid bridges and therefore less aggregation.
- The capillary force between particles was dependent on the surface tension and liquid bridge volume. With the interaction-time dependent spreading rule from the previous section determining the liquid bridge volume, an additional dependence of the liquid viscosity on the capillary force was introduced. A higher surface tension and lower viscosity resulted in a lower capillary force between particles, therefore decreasing the likelihood of aggregate formation due to a capillary force.
- For the majority of cases, the size of the resulting aggregates was beyond the scale of the simulation domain, with over 90 % of the particles forming one large aggregate, restricting further analysis. Larger domains are required for these cases in order to accurately examine the effect this aggregation plays on particle settling.
- The close proximity and lower particle velocities in denser systems resulted in more aggregation, with complete aggregation for all cases representative of fluid coking (in terms of liquid properties) with solids volume fraction of $\phi = 0.5$ and greater.

- The formation of aggregates of a scale smaller than the domain were analyzed in terms to volume-averaged per particle drag force and volume-averaged particle Reynolds number. Increases in mean aggregate size resulted in increases in particle slip Reynolds number and decreases in per particle non-dimensionalized drag force. Conclusions applicable to fluid coking could not be drawn since for the majority of cases, one large aggregate was formed.

5.4 Future Work

Some potential areas of future research are described below.

Improvement of simulation efficiency: In the simulations, the domain size was insufficient to ensure domain-size independence. Simulation times can be improved through optimization (of the interacting particle tracking and applied capillary force calculation) and parallelization, allowing for larger domains to be considered.

Improvement of current simulation models: There are currently limitations on the models used for liquid spreading and aggregation. Extensions that would improve the applicability to practical problems would include introducing a viscous force, taking into account liquid bridge stretching, and tracking the liquid on the particle surface to allow for partially-wetted particles. With multiple sizes of particles within a fluid coker, allowing for the presence of particles of different sizes would be beneficial. Additionally, combination of the liquid spreading and aggregation models would result in a more powerful tool for the investigation of aggregate formation in fluidized beds.

Study of liquid bridge growth: To date there is a lack of understanding of the physics involving liquid film drainage of a wetted particle and the resulting liquid bridge growth. Therefore, liquid spreading models are dependent either on geometry or simple scaling procedures. Experimental or simulation work focusing on film drainage into a liquid bridge would allow for a more comprehensive liquid spreading model to be developed. By introducing particle motion into these studies, the effect of relative particle velocities on the liquid bridge volume could be determined, allowing for liquid properties to be studied where the particle relative velocities are high compared to the capillary bridge growth velocities.

Interactions of particles: The liquid spreading model used in this thesis limits liquid spreading to those of binary collisions. Extending liquid spreading to account for interacting liquid films would allow for liquid to be spread amongst multiple particles.

Bibliography

[1] Canadian Association of Petroleum Producers. Basic Statistics, August 2013. URL `http://www.capp.ca/library/statistics/basic/Pages/default.aspx`.

[2] M R Gray, Z Zhang, W C McCaffrey, I Huq, L Boddez, Z Xu, and J A W Elliott. Measurement of adhesive forces during coking of athabasca vacuum residue. *Industrial & Engineering Chemistry Research*, 42:3549–3554, 2003.

[3] P Darabi. *Mathematical modeling of interaction of wet particles and application to fluidized beds*. PhD thesis, The University of British Columbia, 2011.

[4] M R Gray. Fundamentals of bitumen coking processes analogous to granulation: a critical review. *The Canadian Journal of Chemical Engineering*, 80 (3):393–401, 2002.

[5] W L Nelson. *Petroleum Refinery Engineering, 4th Edition*. McGraw-Hill, New York, 1958.

[6] X Song, J R Grace, H Bi, C J Lim, E Chan, B Knapper, and C McKnight. Experimental simulation of the reactor section of fluid cokers : comparison of FCC and fluid coke particles. *The Canadian Journal of Chemical Engineering*, 84:161–169, 2006.

[7] ExxonMobil Research and Engineering. Fluid coking conversion technologies, August 2013. URL `http://www.exxonmobil.com/Apps/RefiningTechnologies/Files/sellsheet_05_fluidcoking.pdf`.

[8] R Radmanesh, E Chan, and M R Gray. Modeling of mass transfer and thermal cracking during the coking of athabasca residues. *Chemical Engineering Science*, 63:1683–1691, 2008.

[9] Joachim Werther. Fluidized-Bed Reactors. In *Ullmann's Encyclopedia of Industrial Chemistry*, pages 319–366. Wiley, Weinheim, Germany, 2012.

[10] L G Gibilaro. *Fluidization Dynamics*. Elsevier Butterworth-Heinemann, Woburn, MA, 2001.

[11] D Geldart. Types of gas fluidization. *Powder Technology*, 7:285–292, 1973.

[12] R Perry and D Green. *Perry's Chemical Engineering Handbook, 6th edition*. McGraw-Hill, New York, 1984.

[13] T Mikami, H Kamiya, and M Horio. Numerical simulation of cohesive powder behavior in a fluidized bed. *Chemical Engineering Science*, 53(10):1927–1940, 1998.

[14] BJ Ennis, G Tardos, and R Pfeffer. A microlevel-based characterization of granulation phenomena. *Powder Technology*, 65(1-3):257–272, 1991.

[15] P Y Liu, R Y Yang, and A B Yu. Dynamics of wet particles in rotating drums: Effect of liquid surface tension. *Physics of Fluids*, 23(1):013304, 2011.

[16] D Shi and J J McCarthy. Numerical simulation of liquid transfer between particles. *Powder Technology*, 184:64–75, 2008.

[17] K Pougatch. *Mathematical modelling of gas and gas-liquid jets injected into a fluidized bed*. PhD thesis, The University of British Columbia, 2011.

[18] M Dosta, S Antonyuk, and S Heinrich. Multiscale simulation of the fluidized bed granulation process. *Chemical Engineering & Technology*, 35(8):1373–1380, 2012.

[19] J H Ferziger and Perić. *Computational Methods for Fluid Dynamics*. Springer-Verlag, Berlin, 2002.

[20] H P Zhu, Z Y Zhou, R Y Yang, and A B Yu. Discrete particle simulation of particulate systems: Theoretical developments. *Chemical Engineering Science*, 62(13):3378–3396, 2007.

[21] B J Alder and T E Wainwright. Studies in molecular dynamics. I. general method. *The Journal of Chemical Physics*, 31(2):459–466, 1959.

[22] C S Campbell and C E Brennen. Computer simulation of granular shear flows. *Journal of Fluid Mechanics*, 151:167–188, 1985.

[23] P A Cundall and O D L Strack. A discrete numerical model for granular assemblies. *Géotechnique*, 29(1):47–65, 1979.

[24] M A van der Hoef, M van Sint Annaland, N G Deen, and J A M Kuipers. Numerical simulation of dense gas-solid fluidized beds: a multiscale modeling strategy. *Annual Review of Fluid Mechanics*, 40:47–70, 2008.

[25] J J Derksen and S Sundaresan. Direct numerical simulations of dense suspensions: wave instabilities in liquid-fluidized beds. *Journal of Fluid Mechanics*, 587:303–336, 2007.

[26] Y Yamamoto, M Potthoff, T Tanaka, T Kajishima, and Y Tsuji. Large-eddy simulation of turbulent gas-particle flow in a vertical channel: effect of considering inter-particle collisions. *Journal of Fluid Mechanics*, 442:303–334, 2001.

[27] J J Derksen. Direct numerical simulations of aggregation of monosized spherical particles in homogeneous isotropic turbulence. *AIChE Journal*, 58(8): 2589–2600, 2012.

[28] J Wang, MA van der Hoef, and J A M Kuipers. Comparison of two-fluid and discrete particle modeling of dense gas-particle flows in gas-fluidized beds. *Chemie Ingenieur Technik*, 85(3):290–298, 2013.

[29] R Y Yang, R P Zou, and A B Yu. Numerical study of the packing of wet coarse uniform spheres. *AIChE Journal*, 49(7):1656–1666, 2003.

[30] S M Iveson, J D Litster, K Hapgood, and B J Ennis. Nucleation, growth and breakage phenomena in agitated wet granulation processes: a review. *Powder Technology*, 117(1-2):3–39, 2001.

[31] Y S Cheong, C Mangwandi, J Fu, M J Adams, M J Hounslow, and A D Salman. A mechanistic description of granule deformation and breakage. In *Handbook of Powder Technology*, volume 12, pages 1055–1120. Elsevier B. V., Amsterdam, The Netherlands, 2007.

[32] S S Hsiau and M L Hunt. Kinetic theory analysis of flow- induced particle diffusion and thermal conduction in granular material flows. *Journal of Heat Transfer*, 115:541–548, 1993.

[33] R Mani, D Kadau, and H J Herrmann. Liquid migration in sheared unsaturated granular media. *Granular Matter*, 15:447–454, 2012.

[34] F Soulié, F Cherblanc, M S El Youssoufi, and C Saix. Influence of liquid bridges on the mechanical behaviour of polydisperse granular materials. *International Journal for Numerical and Analytical Methods in Geomechanics*, 30(3):213–228, 2006.

[35] B V Balakin, S Alyaev, A C Hoffmann, and P Kosinski. Micromechanics of agglomeration forced by the capillary bridge : the restitution of momentum. *AIChE Journal*, 59(11):4045–4057, 2013.

[36] S Radl, E Kalvoda, B J Glasser, and J G Khinast. Mixing characteristics of wet granular matter in a bladed mixer. *Powder Technology*, 200(3):171–189, 2010.

[37] B Remy. *Granular flow, segregation and agglomeration in bladed mixers*. PhD thesis, Rutgers, The State University of New Jersey, 2010.

[38] L Duchemin, J Eggers, and C Josserand. Inviscid coalescence of drops. *Journal of Fluid Mechanics*, 487:167–178, 2003.

[39] M Gross, I Steinbach, D Raabe, and F Varnik. Viscous coalescence of droplets: a lattice Boltzmann study. *Physics of Fluids*, 25:052101, 2013.

[40] J D Paulsen, J C Burton, and S R Nagel. Viscous to inertial crossover in liquid drop coalescence. *Physical Review Letters*, 106(11):114501, 2011.

[41] G Lian, C Thorntons, and M J Adams. Discrete particle simulation of agglomerate impact coalescence. *Chemical Engineering Science*, 53(19):3381–3391, 1998.

[42] O Pitois, P Moucheront, and X Chateau. Liquid bridge between two moving spheres: an experimental study of viscosity effects. *Journal of colloid and interface science*, 231(1):26–31, 2000.

[43] W B Haines. Studies in the physical properties of soils. *The Journal of Agricultural Science*, 15:529–535, 1925.

[44] V P Mehrotra and K V S Sastry. Pendular bond strength between unequal-sized spherical particles. *Powder Technology*, 25(2):203–214, 1980.

[45] X Pepin, D Rossetti, S M Iveson, and S J Simons. Modeling the evolution and rupture of pendular liquid bridges in the presence of large wetting hysteresis. *Journal of colloid and interface science*, 232(2):289–297, 2000.

[46] D Megias-Alguacil and L J Gauckler. Accuracy of the toroidal approximation for the calculus of concave and convex liquid bridges between particles. *Granular Matter*, 13(4):487–492, 2011.

[47] C D Willett, M J Adams, S A Johnson, and J P K Seville. Capillary bridges between two spherical bodies. *Langmuir*, 16(24):9396–9405, 2000.

[48] L R Fisher and J N Israelachvili. Direct measurement of the effect of meniscus forces on adhesion: a study of the applicability of macroscopic thermodynamics to microscopic liquid interfaces. *Colloids and Surfaces*, 3:303–319, 1981.

[49] M J Adams and V Perchard. The cohesive force between particles with interstitial liquid. *Institution of Chemical Engineers Symposium*, 91:147–160, 1985.

[50] J N Israelachvili. Adhesion and wetting phenomena. In *Intermolecular and Surface Forces*, pages 415–467. Elsevier Inc., Burlington, MA, 2011.

[51] G Lian, C Thorntons, and M J Adams. A theoretical study of the liquid bridge forces between two rigid spherical bodies. *Journal of colloid and interface science*, 161:138–147, 1993.

[52] D N Mazzone, G I Tardos, and R Pfeffer. The behavior of liquid bridges between two relatively moving particles. *Powder Technology*, 51:71–83, 1987.

[53] S Kim and S Karrila. *Microhydrodynamics: Principles and Selected Applications*. Butterworth-Heinemann, Boston, 1991.

[54] A J Goldman, R G Cox, and H Brenner. Slow viscous motion of a sphere parallel to a plane wall-1 Motion through a quiescent fluid. *Chemical Engineering Science*, 22:637–651, 1967.

[55] J J Derksen. Dense suspensions – solid – liquid interactions at the particle scale. *Progress in Computational Fluid Dynamics*, 12(2/3):103–111, 2012.

[56] J J Derksen. Simulations of hindered settling of flocculating spherical particles. *International Journal of Multiphase Flow*, 58:127–138, 2014.

[57] U Frisch, B Hasslacher, and Y Pomeau. Lattice-gas automata for the Navier-Stokes equation. *Physical Review Letters*, 56(14):1505–1508, 1986.

[58] S Wolfram. Cellular automaton fluids 1: basic theory. *Journal of Statistical Physics*, 45(3–4):471–526, 1986.

[59] S Chen and G D Doolen. Lattice Boltzmann method for fluid flows. *Annual Review of Fluid Mechanics*, 30:329–364, 1998.

[60] J A Somers. Direct simulation of fluid flow with cellular automata and the lattice-Boltzmann equation. *Applied Scientific Research*, 51(1-2):127–133, 1993.

[61] D D'Humieres, P Lallemand, and U Frisch. Lattice gas models for 3D hydrodynamics. *Europhysics Letters*, 2(4):291–297, 1986.

[62] J G M Eggels and J A Somers. Numerical simulation of free convective flow using the lattice-Boltzmann scheme. *International Journal of Heat and Fluid Flow*, 16(5):357–364, 1995.

[63] O Shardt, J J Derksen, and S K Mitra. Simulations of droplet coalescence in simple shear flow. *Langmuir*, 29(21):6201–6212, 2013.

[64] Anthony J C Ladd. Numerical simulations of particulate suspensions via a discretized Boltzmann equation . Part 2 . Numerical results. *Journal of Fluid Mechanics*, 271:311–339, 1994.

[65] A J C Ladd. Numerical simulations of particulate suspensions via a discretized Boltzmann equation. Part 1. Theoretical foundation. *Journal of Fluid Mechanics*, 271:285–309, 1994.

[66] M Bouzidi, M Firdaouss, and P Lallemand. Momentum transfer of a Boltzmann-lattice fluid with boundaries. *Physics of Fluids*, 13(11):3452–3459, 2001.

[67] J J Derksen and H E A Van den Akker. Large eddy simulations on the flow driven by a Rushton turbine. *AIChE Journal*, 45(2):209–221, 1999.

[68] D Goldstein, R Handler, and L Sirovich. Modeling a no-slip flow boundary with an external force field. *Journal of Computational Physics*, 105:354–366, 1993.

[69] A ten Cate, C H Nieuwstad, J J Derksen, and H E A Van den Akker. Particle imaging velocimetry experiments and lattice-Boltzmann simulations on a single sphere settling under gravity. *Physics of Fluids*, 14(11):4012, 2002.

[70] K Suzuki and T Inamuro. Effect of internal mass in the simulation of a moving body by the immersed boundary method. *Computers & Fluids*, 49(1):173–187, 2011.

[71] L Schiller and A Z Nauman. Über die grundlegenden Berechnungen bei der Schwerkraftaufbereitung. *Verein Deutscher Ingenieure Zeitung*, 77:318–320, 1935.

[72] X Song, H Bi, C J Lim, J R Grace, E Chan, B Knapper, and C McKnight. Hydrodynamics of the reactor section in fluid cokers. *Powder Technology*, 147(1-3):126–136, 2004.

[73] M R Gray, W C McCaffrey, I Huq, and T Le. Kinetics of cracking and devolatilization during coking of athabasca residues. *Industrial & Engineering Chemistry Research*, 43(18):5438–5445, 2004.

[74] G D Cody, D J Goldfarb, G V Storch, and A N Norris. Particle granular temperature in gas fluidized beds. *Powder Technology*, 87:211–232, 1996.

[75] B J Glasser, I G Kevrekidis, and S Sundaresan. Fully developed travelling wave solutions and bubble formation in fluidized beds. *Journal of Fluid Mechanics*, 334:157–188, 1997.

[76] B J Glasser, I G Kevrekidis, and S Sundaresan. One- and two-dimensional travelling wave solutions in gas-fluidized beds. *Journal of Fluid Mechanics*, 306:183–221, 1996.

[77] P Duru, M Nicolas, J Hinch, and É Guazzelli. Constitutive laws in liquid-fluidized beds. *Journal of Fluid Mechanics*, 452:371–404, 2002.

[78] M M El-Kaissy and G M Homsy. Instability waves and the origin of bubbles in fluidized beds. *International Journal of Multiphase Flow*, 2(4):379–395, 1976.

[79] S E Harris and D G Crighton. Solitons, solitary waves, and voidage disturbances in gas-fluidized beds. *Journal of Fluid Mechanics*, 266:243–276, 1994.

[80] C M Donahue, R H Davis, A A Kantak, and C M Hrenya. Mechanisms for agglomeration and deagglomeration following oblique collisions of wet particles. *Physical Review E*, 86:021303, 2012.

[81] R J Hill, D L Koch, and A J C Ladd. Moderate-Reynolds-number flows in ordered and random arrays of spheres. *Journal of Fluid Mechanics*, 448:243–278, 2001.

[82] M Ye, M A van der Hoef, and J A M Kuipers. The effects of particle and gas properties on the fluidization of Geldart A particles. *Chemical Engineering Science*, 60(16):4567–4580, 2005.

[83] T B Anderson and R Jackson. A fluid mechanical description. Comparison of theory and experiment. *Industrial & Engineering Chemistry Fundamentals*, 8 (1):137–144, 1969.

[84] K G Anderson, S Sundaresan, and R Jackson. Instabilities and the formation of bubbles in fluidized beds. *Journal of Fluid Mechanics*, 303:327–366, 1995.

[85] R A Fisher. On the capillary forces in an ideal soil; correction of formulae given by W.B. Haines. *Journal of Agricultural Science*, 16(3):492–505, 1926.

Appendix A

Derivation of Liquid Bridge Capillary Force

Using the Young-Laplace equation, the pressure differential ΔP is given as:

$$\Delta P = \sigma \left(\frac{1}{b} - \frac{1}{R_{ext}} \right) \tag{A.1}$$

Geometric parameters are shown in Figure A.1. The negative sign in Equation (A.1) accounts for R_{ext} being outside of the liquid bridge, with R_{ext} taken as the absolute value. Additionally, for small separation distances at all times after an initial growth period, the inner radius of curvature will be larger than the outer radius of curvature. These assumptions are shown as follows:

$$\begin{aligned} R_{ext} &= |R_{ext}| > 0 \\ b &> R_{ext} \end{aligned} \tag{A.2}$$

Therefore:

$$\Delta P < 0$$

The geometry and relevent variables are defined in Figure A.1.

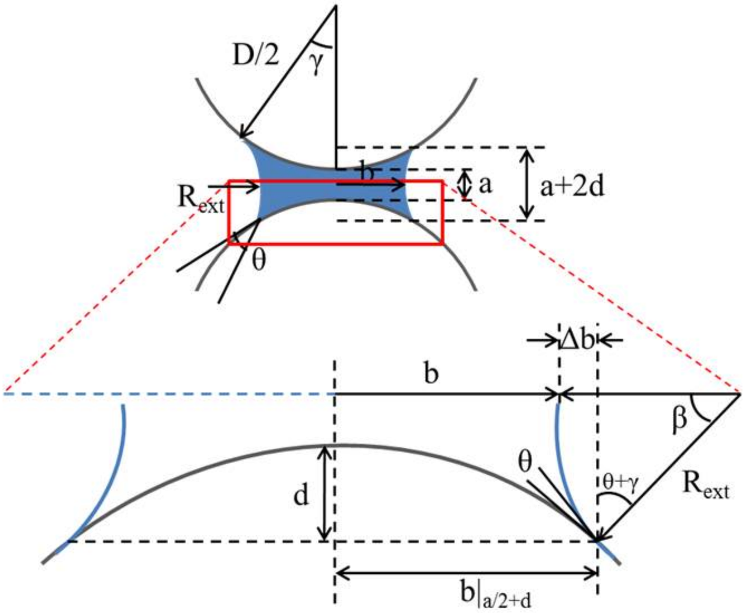

Figure A.1: Liquid Bridge Geometry: variables used for force derivation.

The force acting on a particle is the sum of the contributions due to the surface tension and the Young-Laplace pressure. However, due to the assumption that liquid film coats the particle fully, there is no 3-phase contact line on which the surface tension affects the particle. Therefore, only the pressure component is relevant.

The profile of the bridge is not known, making the mean curvature calculation difficult. Because of this, a toroidal approximation is made, defining the outer radius R_{ext} as constant [43]. With this approximation, the mean radius of curvature varies along the length of the bridge. There are therefore two methods of describing the force acting on the particles due to a liquid bridge. The two methods are the gorge and boundary methods.

A.1 Method 1: Gorge Method

The gorge method looks at the force at the neck of the bridge (*b*) [85].

$$\begin{aligned}F_{gorge} &= -\pi b^2 \Delta P \\ &= -\pi b^2 \sigma \left(\frac{1}{b} - \frac{1}{R_{ext}}\right) \\ &= -\pi b \sigma + \frac{\pi b^2 \sigma}{R_{ext}} \\ &= \pi b \sigma \left(\frac{b}{R_{ext}} - 1\right) \qquad \text{(A.3)}\end{aligned}$$

In order for this equation to be applied, values of b and R_{ext} must be determined in terms of other geometric variables.

A.1.1 Determining the value of R_{ext} in terms of other variables

Define $a+2d$ as the distance between particles at the point where the liquid bridge connects the liquid film (furthermore referred to as the contact line):

$$\begin{aligned}\frac{a+2d}{2} &= \frac{a}{2} + \frac{D}{2} - \frac{D}{2}\cos\gamma \\ &= \frac{a+2d}{2} + \frac{D}{2}(1-\cos\gamma) \qquad \text{(A.4)}\end{aligned}$$

$a+2d$ can additionally be defined using R_{ext}:

$$\begin{aligned}\frac{a+2d}{2} &= R_{ext}\sin\eta \\ &= R_{ext}\sin[90-(\theta+\gamma)] \\ &= R_{ext}\cos(\theta+\gamma) \qquad \text{(A.5)}\end{aligned}$$

Where the relation of η, γ, and θ are shown in Figure A.2. The joining point of the lines is the contact line.

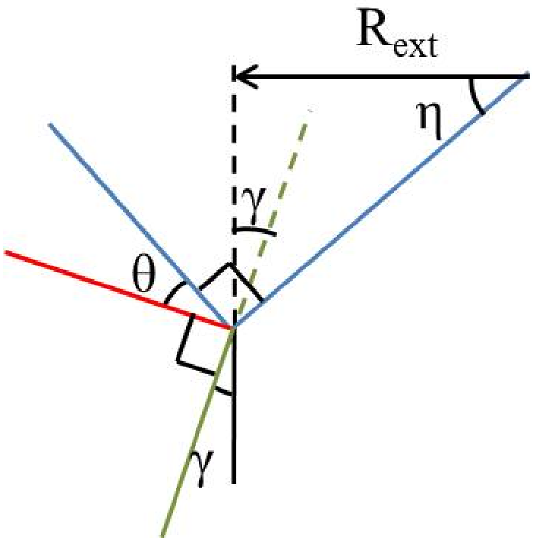

Figure A.2: Angles at contact point to determine relation of η, γ, and θ.

Combining the equations above and solving for R_{ext}:

$$\frac{a}{2}+\frac{D}{2}(1-\cos\gamma)=R_{ext}\cos(\theta+\gamma)$$

$$R_{ext}=\frac{\frac{a}{2}+\frac{D}{2}(1-\cos\gamma)}{\cos(\theta+\gamma)} \tag{A.6}$$

A.1.2 Determining the value of b in terms of other variables

Evaluating the distance from the liquid-gas interface at the bridge neck b to the contact line along b (Δb):

$$\Delta b=R_{ext}-R_{ext}\sin(\theta+\gamma) \tag{A.7}$$

$$\begin{aligned} b&=\frac{D}{2}\sin\gamma-\Delta b\\ &=\frac{D}{2}\sin\gamma-R_{ext}[1-\sin(\theta+\gamma)] \end{aligned} \tag{A.8}$$

By combining Equations (A.6) and (A.8), the pressure differential can be determined based on the particle diameter D, separation distance a, contact angle θ and half-filling angle γ.

A.2 Method 2: Boundary Method

The boundary method looks at the force at the contact line. The liquid bridge internal radius at the contact line is defined as $b|_{a/2+d} = D/2 \sin\gamma$.

$$\begin{aligned} F_{boundary} &= -\pi b|_{a/2+d}^{2} \Delta P \\ &= -\pi b|_{a/2+d}^{2} \sigma \left(\frac{1}{b|_{a/2+d}} - \frac{1}{R_{ext}} \right) \end{aligned} \tag{A.9}$$

Assuming that $D/2 >> b >> R_{ext}$ [48] , and since $b|_{a/2+d} > b$:

$$\begin{gathered} \gamma \approx 0 \\ \frac{1}{b|_{a/2+d}} << \frac{1}{R_{ext}} \end{gathered} \tag{A.10}$$

Therefore:

$$F \approx \frac{\pi b|_{a/2+d}^{2} \sigma}{R_{ext}}$$

For small curvature ($R >> b$), the spherical cap cross-sectional area is approximately equivalent to its surface area [50]:

$$\pi b|_{a/2+d}^{2} \approx \pi D d \tag{A.11}$$

Therefore:

$$F \approx \frac{\pi D d \sigma}{R_{ext}} \tag{A.12}$$

The separation distance at $a+2d$ is given by:

$$\begin{aligned} 2R_{ext} \cos(\theta+\gamma) &\approx 2R_{ext} \cos(\theta) \\ &\approx 2d + a \end{aligned} \tag{A.13}$$

Rearranging for d:

$$d = \frac{2R_{ext} \cos\theta - a}{2} \tag{A.14}$$

The force from Equation (A.12) can therefore be written as:

$$\begin{aligned} F &= \frac{\pi D\sigma}{R_{ext}} \left(R_{ext}\cos\theta - \frac{a}{2} \right) \\ &= \pi D\sigma\cos\theta \left(1 - \frac{a}{2R_{ext}\cos\theta} \right) \end{aligned} \tag{A.15}$$

A.3 Relating Force to Liquid Bridge Volume and Separation Distance

In order to relate the force equation above to liquid bridge volume, a flat profile for the liquid bridge is approximated [42]. This allows for the volume to be calculated as follows.

$$V = \int_0^{b|_{a/2+d}} 2\pi r H(r)\,\mathrm{d}r \tag{A.16}$$

where $H(r)$ is the normal distance between spheres. To develop an equation for $H(r)$, y_1 and y_2 are defined as the equations for the two spheres (with y the axis parallel to the line connected the sphere centres), separated by a :

$$H(r) = a + y_1 - y_2 \tag{A.17}$$

The equation of a sphere ($x^2 + y^2 + z^2 = (D/2)^2$) is shifted into cylindrical coordinates ($x^2 + z^2 = r^2$). The variable r represents the radius of the bridge (going from 0 to $b|_{a/2+d}$). With no separation distance, the equations for the spheres become:

$$\begin{aligned} y_1 &= -\sqrt{(D/2)^2 - r^2} + D/2 \\ y_2 &= \sqrt{(D/2)^2 - r^2} - D/2 \end{aligned} \tag{A.18}$$

Therefore:

$$\begin{aligned} H(r) &= a - 2\sqrt{(D/2)^2 - r^2} + D \\ &= a + D\left(1 - \sqrt{1 - \frac{r^2}{(D/2)^2}}\right) \end{aligned} \tag{A.19}$$

Using Taylor Series Expansion:

$$\sqrt{1 - \frac{r^2}{(D/2)^2}} \approx 1 - \frac{r^2}{D^2/2} \tag{A.20}$$

This yields:

$$H(r) \approx a + \frac{r^2}{(D/2)} \tag{A.21}$$

Plugging $H(r)$ into the liquid bridge volume:

$$\begin{aligned} V &= \int_0^{b|_{a/2+d}} 2\pi r\left(a + \frac{r^2}{(D/2)}\right) \mathrm{d}r \\ &= \pi a b|_{a/2+d}{}^2 + \frac{\pi}{D} b|_{a/2+d}{}^4 \\ &= \pi \frac{D}{4}\left(2a \frac{b|_{a/2+d}{}^2}{(D/2)} + \frac{b|_{a/2+d}{}^4}{(D/2)^2}\right) \\ &= \pi \frac{D}{4}[H^2(b|_{a/2+d}) - a^2] \end{aligned} \tag{A.22}$$

From geometry, $H(b|_{a/2+d}) \approx 2R_{ext}\cos\theta$. Therefore, the liquid bridge volume becomes:

$$V = \pi \frac{D}{4}[(2R_{ext}\cos\theta)^2 - a^2] \tag{A.23}$$

Solving for $2R_{ext}\cos\theta$:

$$2R_{ext}\cos\theta = \sqrt{\frac{V + \frac{\pi D}{4}a^2}{\frac{\pi D}{4}}} \tag{A.24}$$

Plugging this into Equation (A.15) gives:

$$
\begin{aligned}
F &= \pi D \sigma \cos\theta \left(1 - \frac{a}{\sqrt{\frac{V + \frac{\pi D}{4} a^2}{\frac{\pi D}{4}}}} \right) \\
&= \pi D \sigma \cos\theta \left(1 - \frac{1}{\sqrt{\frac{V + \frac{\pi D}{4} a^2}{\frac{\pi D a^2}{4}}}} \right) \\
&= \pi D \sigma \cos\theta \left(1 - \frac{1}{\sqrt{1 + \frac{4V}{\pi D a^2}}} \right) \qquad \text{(A.25)}
\end{aligned}
$$

Appendix B

Application of a Diffusion Curve to Simulation Data

B.1 Diffusion Equation

Making the assumption that liquid spreading due to particle-particle collisions and particle motion within a fluidized bed can be approximated as a diffusion process, the following differential equation needs to be solved.

$$\frac{\partial C}{\partial t} = \Gamma \frac{\partial^2 C}{\partial x^2} \tag{B.1}$$

The initial condition is that of a Dirac delta function, defined as a function that is 0 everywhere except at x=0, and an integral of one over the real domain. The Dirac delta is an approximation of the simulation initial condition, which has a finite thickness and height. Therefore, at small simulation times the resulting diffusion coefficient will be inaccurate. At greater simulation times, this effect should be mitigated. The boundary and initial conditions are presented in Equation (B.2).

$$\begin{aligned} C(x,0) &= \delta(x) \\ C(\infty,t) &= 0 \\ \left.\frac{\partial C}{\partial x}\right|_{x=\infty} &= 0 \end{aligned} \tag{B.2}$$

Because of the infinite boundary conditions in the solution and the periodic boundary conditions within the simulation, results can only be considered up to the time where liquid is transferred across the symmetry plane opposite the initially wetted plane. By applying the boundary and initial conditions in Equation (B.2) and ensuring mass conservation, a solution is given as shown in Equation (B.3) [1].

$$C(x,t) = \frac{\frac{m}{A}}{\sqrt{4\pi\Gamma t}} exp\left(\frac{-x^2}{4\Gamma t}\right) \tag{B.3}$$

Where:
$C =$ liquid mass concentration (kg/m^3)
$m =$ total liquid mass in the system (kg)
$A =$ cross-sectional area of diffusion plane (m^2)
$\Gamma =$ effective liquid diffusion coefficient (m^2/s)
$x =$ direction of diffusion (m)
$t =$ time (s)

Diffusion in the horizontal and vertical directions is calculated the same way. The derivation for the horizontal direction is shown below. Dividing both sides of Equation (B.3) by liquid density, the total liquid mass and liquid mass concentration become total liquid volume $V_{l,tot}$ and liquid volume fraction ϕ_l, respectively.

$$\phi_l(x,t) = \frac{\frac{V_{l,tot}}{A}}{\sqrt{4\pi\Gamma t}} exp\left(\frac{-x^2}{4\Gamma t}\right) \tag{B.4}$$

From Equation (B.4), the total liquid volume in the system is calculated as follows.

$$V_{l,tot} = \sum_{i=1}^{N} \pi D^2 \delta_i \tag{B.5}$$

N is the total number of particles in the system, N_{plane} is the number of particles occupying any volume in a plane, and δ_i is the liquid film thickness on particle i. The domain is split into slices Δp (for the analysis, $\Delta p/D = 0.04$ is used), calculating the liquid volume fraction ϕ_l in every slice. The liquid volume fraction in a slice can be calculated as follows.

$$\phi_l(\Delta p, t) = \sum_{i=1}^{N_{plane}} \frac{V_{l,i}}{V_{plane}} = \frac{1}{V_{plane}} \sum_{i=1}^{N_{plane}} \pi D h_i \delta_i \tag{B.6}$$

where $V_{l,i}$ is the volume of liquid from particle i within the slice. h_i is the height of sphere i within the slice, as shown in Figure B.1 for two slices. The derivation for the equation of the surface area of a spherical cap is shown in the next section.

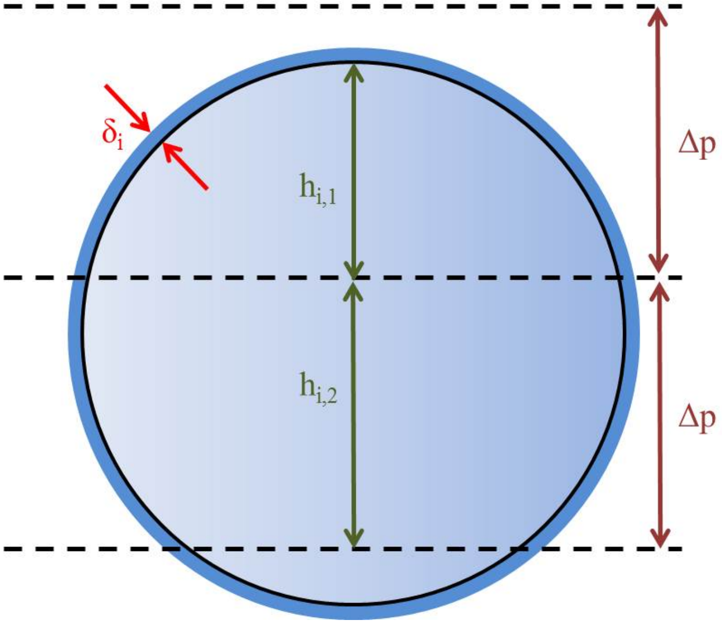

Figure B.1: Description of variables regarding diffusion analysis. The black dotted lines separate slices of thickness Δp. The value of h_i is shown for a sphere through two cuts: where the sphere ends within a slice $h_{i,1}$ and where the slice cuts through the sphere $h_{i,2}$.

Combining Equation (B.4) with those above results in Equation (B.7).

$$\frac{1}{V_{plane}} \sum_{i=1}^{N_{plane}} \pi D h_i \delta_i = \frac{1}{A_{plane}\sqrt{4\pi\Gamma t}} exp\left(\frac{-x^2}{4\Gamma t}\right) \sum_{i=1}^{N} \pi D^2 \delta_i \tag{B.7}$$

Substituting $V_{plane} = A_{plane}\Delta p$ into Equation (B.7), adding a fitting parameter β for the position, simplifying and rearranging yields the following equation.

$$\frac{1}{\Delta p} \sum_{i=1}^{N_{plane}} \frac{h_i}{D} \delta_i = \frac{1}{\sqrt{4\pi\Gamma t}} exp\left(\frac{-(x-\beta)^2}{4\Gamma t}\right) \sum_{i=1}^{N} \delta_i \tag{B.8}$$

Equation (B.8) can now be used in the analysis of the simulations.

B.2 Spherical Cap Surface Area

The circumference of a circle over the arc length s is integrated to determine the surface area within a slice of a sphere.

$$A = \int 2\pi r(s) ds \tag{B.9}$$

Where:
A = surface area (m^2)
s = arc length (m)
$r(s)$ = radius at position s

To determine $r(s)$, two radii r_1 and r_2 are defined, with r_1 at the base of the spherical cap and r_2 at an arbitrary height within the spherical cap, as in Figure B.2. Using pythagorean theorem:

$$\begin{aligned} r_1 &= D/2\sin(\alpha) \\ r_2 &= D/2\sin(\alpha - \eta) \end{aligned} \tag{B.10}$$

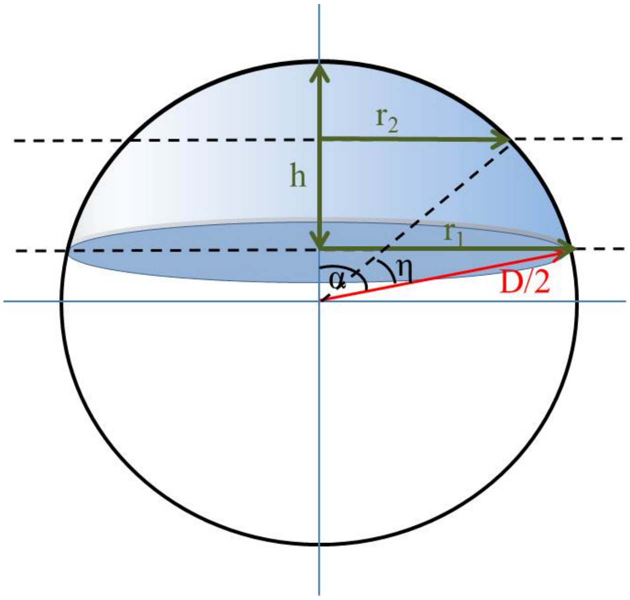

Figure B.2: Spherical Cap

By definition, the arc length between r_1 and r_2 is given by $s = D/2\eta$. From this, $r(s)$ is expressed as follows.

$$r(s) = D/2\sin(\alpha - \frac{2s}{D}) \tag{B.11}$$

Substituting this into Equation (B.9) gives

$$A = \pi D \int_0^{D/2\alpha} \sin(\alpha - \frac{2s}{D})ds \tag{B.12}$$

Integrating yields

$$A = \pi/2D^2 \left[\cos(\alpha - \frac{2s}{D})\right]_0^{D/2\alpha} \tag{B.13}$$

$$= \pi/2D^2(1 - \cos\alpha) \tag{B.14}$$

Substituting $h = D/2(1-\cos\alpha)$, the equation for the surface area of a spherical cap becomes

$$A = \pi Dh \tag{B.15}$$